EFFECTS OF FIBER DISCONTINUITY IN FIBER REINFORCED POLYMER MATRIX COMPOSITES

A Thesis Submitted to
the Graduate School İzmir Institute of Technology
in Partial Fulfillment of the Requirements for the Degree of

DOCTOR OF PHILOSOPHY

in Mechanical Engineering

by
Ahmet Süha KILIÇOĞLU

July 2024
İZMİR

We approve the thesis of **Ahmet Süha KILIÇOĞLU**

Examining Committee Members:

Prof. Dr. Metin TANOĞLU
Mechanical Engineering, Izmir Institute of Technology

Prof. Dr. H. Seçil ARTEM
Mechanical Engineering, Izmir Institute of Technology

Prof. Dr. Engin AKTAŞ
Civil Engineering, Izmir Institute of Technology

Prof. Dr. Evren M. TOYGAR
Mechanical Engineering, Dokuz Eylül University

Prof. Dr. M. Özgür SEYDIBEYOĞLU
Metallurgical and Materials Engineering, İzmir Katip Çelebi University

16 July 2024

Prof. Dr. Metin TANOĞLU
Supervisor, Mechanical Engineering,
Izmir Institute of Technology

Prof. Dr. M. İ. Can Dede
Head of the Department of
Mechanical Engineering

Prof. Dr. Mehtap EANES
Dean of the Graduate School

ACKNOWLEDGMENTS

ABSTRACT

EFFECTS OF FIBER DISCONTINUITY IN FIBER REINFORCED POLYMER MATRIX COMPOSITES

This dissertation examines how structural discontinuities affect the mechanical properties of composite beams reinforced with glass fibers. The study explicitly classifies these discontinuities as inter-ply or intra-ply based on discontinuity types within the composite layers. Discontinuities were introduced as pre-curing. The mechanical properties of these samples were evaluated using servo-hydraulic actuators in three-point bending quasi-static tests. The experimental results were compared to the predictions of CAE analysis by assessing the sectional fiber volume fraction and further complemented with microscopic analysis of local discontinuities.

The study found that areas of dislocation lead to zones with a high concentration of resin, and the exothermic curing process causes increased temperatures. As a result, the resin changes color from clear to yellow, indicating decreased mechanical durability. Fiber discontinuities and resin gaps weaken the structural integrity of glass fiber-reinforced polymer (GFRP) composite leaf springs. Irregularities in manufacturing, whether between layers or within a single layer, can impact the durability of the material and its ability to fill gaps. The findings highlight the significance of material composition, structural integrity, and comprehension of failure mechanisms in the design and production of composite beams. It is essential to address heat transfer concerns to reduce resin gaps and prevent fractures caused by heat. The results indicate that understanding the relationship between internal structural flaws and gaps in the resin can greatly improve the design and production of beams. This study offers crucial insights for enhancing composite materials' structural performance and dependability in engineering applications.

ÖZET

FİBER TAKVİYELİ POLİMER MATRIS KOMPOZİTLERDE FİBER SÜREKSİZLİĞİNİN ETKİSİ

Bu tez, cam elyaf takviyeli kompozit plakaların mekanik davranışları üzerindeki yapısal süreksizliklerin etkisini araştırmaktadır. Bu süreksizlikler, kompozit mikro yapısındaki geometrik kısıtlamalar nedeniyle katmanlar arası (inter-ply) ve katman içi (intra-ply) olarak sınıflandırılmıştır. Süreksizlikler kürleme öncesi ilave edilmiştir. İlk olarak, malzeme özellikleri kupon seviyesinde testlerle belirlenmiştir. Daha sonra, bilgisayarlı sayısal kontrol kesimi ve manuel uygulama ile katman içi süreksizlikler oluşturularak iki tam ölçekli kompozit numune üretilmiştir. Bu numunelerin mekanik özellikleri, servo-hidrolik aktüatörler kullanılarak üç nokta eğme testi ile değerlendirilmiştir. Deneysel test sonuçları, kesitsel fiber hacim oranı değerlendirilerek CAE analiz tahminleriyle karşılaştırılmış ve yerel süreksizliklerin mikroskopik analizi ile desteklenmiştir.

Çalışma, yer değiştirme bölgelerinin reçine açısından zengin alanlara yol açtığını ve ekzotermik kürleme sürecinin reçinenin rengini şeffaftan sarıya dönüştürdüğünü, bunun da mekanik dayanıklılığı azalttığını ortaya koymuştur. Ayrıca, fiber süreksizlikleri ve reçine boşlukları, cam elyaf takviyeli polimer (GFRP) kompozit yaprak yayların yapısal bütünlüğünü olumsuz etkilemektedir. Üretim sürecindeki düzensizlikler, malzeme dayanıklılığını ve boşluk doldurma kapasitesini etkilemektedir. Isı transferi ile ilgili sorunların ele alınması, reçine boşluklarını ve ısı kaynaklı çatlakları azaltmak için önemlidir. Bulgular, iç yapısal kusurlar ve reçine boşlukları arasındaki ilişkiyi anlamanın, kiriş tasarımı ve üretim süreçlerini önemli ölçüde iyileştirebileceğini önermektedir. Bu çalışma, mühendislik uygulamalarında kompozit malzemelerin yapısal performansını ve güvenilirliğini optimize etmek için kritik bilgiler sunmaktadır.

I dedicate this thesis to my dear family, Nermin, Nihat, and Naz

KILIÇOĞLU

PREFACE

This research aimed to explore the limitations of producing thick beams. When creating these beams, certain geometric restrictions prevent the use of fiber reinforcements. The study involved testing five variations of a model reinforced with glass fibers, a type that OlgunÇelik[1] has been consistently manufacturing. This model has undergone examination and practical testing in light commercial vehicles across various countries for about a decade.

Throughout the study, introducing five deviations from the model enhanced the correlation of results with real-world values. The findings from this investigation are significant as they reveal that areas of displacement within composites lead to resin regions. The exothermic curing process triggers temperature increases, causing the transparent resin to turn yellow, indicating a decrease in strength.

The presence of occurrences, fiber interruptions, and resin gaps compromises the integrity of glass fiber-reinforced polymer (GFRP) composite leaf springs. Irregularities within or across layers impact the material's durability and ability to fill voids.

This study has shown that understanding the makeup of parts, the strength of structures, and identifying reasons for failures are factors in creating and making beams. It's essential to focus on solving heat transfer issues to prevent gaps in resin and fractures caused by uncontrolled heat. A critical element that can significantly improve beam design and production is grasping the relationship between discontinuities and resin gaps. This research offers insights for enhancing the performance and reliability of thick polymer matrix composites in engineering applications. The knowledge gained from this study will support advancements in thick polymer beam

Further investigation will be done after this study to enhance the understanding of the formation of carbonyl[2] mechanism using FTIR.

TABLE OF CONTENTS

LIST OF FIGURES

LIST OF TABLES

LIST OF SYMBOLS AND ABBREVIATIONS

3D	Three dimensional
CAA	Computer Aided Analysis
CAE	Computer Aided Engineering
CFRC	Carbon fiber reinforced composite
CMC	Ceramic matrix composites
E	Young's modulus
F	Force
F_{max}	Maximum force
FRP	Fiber-Reinforced Polymer
FVF	Fiber Volume Fraction
GFRC	Glass fiber reinforced composite
GFRP	Glass fiber-reinforced polymer
GPa	Giga Pascal
GSM	Grams per square meter
HP-RTM	High-Pressure Resin Transfer Molding
I.E.	In example
ILSS	Inter Laminar Shear Strength
J	Joule
k	A thousand times of
L	Final length
L0	Initial length
m	Meter
m^2	meter square
MMC	Metal matrix composites
MPa	Mega Pascal
N	Newton
NCF	Non-crimp Fabric
P_{max}	Maximum force
PMC	Polymer matrix composites

Prepreg	Pre-impregnated composite raw material.
PVA	Polyvinyl alcohol
RTM	Resin Transfer Molding
TDS	Technical datasheet
TEX	Weight per kilometer in grams
UD	Unidirectional
UDGFR	Unidirectional glass reinforced
UD-NCF	Unidirectional-Non crimped Fabrics
UTS	Ultimate Tensile Strength
VARTM	Vacuum-Assisted Resin Transfer Molding
δ	Displacement
ε	Strain
ε_0	Initial Strain
ε_p	Plastic Strain
σ	Stress

CHAPTER 1

INTRODUCTION

Composite materials are formed by combining multiple materials to allow the final material to possess the average properties of the materials used. The final material will have neither the pure strengths nor weaknesses of the primary materials. The outcome will be fashioned to achieve equilibrium among the primary materials' specifications. Composite materials possess a high degree of flexibility in their designability, allowing for variations in material composition, geometric structure, and production techniques.

A high stiffness-to-weight ratio can be achieved by controlling the direction of the fibers. Furthermore, enhancing specific specifications of the more affordable or less long-lasting materials is possible. The primary distinction between the solution of materials, such as alloying, and composite materials is that composite materials can be mechanically disassembled from one another.[3–5]

Composite materials have a diverse range of applications. The high stress-to-weight ratio of these materials makes them popular in transportation technologies. Composite materials are commonly used in the sports industry to manufacture race car parts, bicycle frames and components, skis, oars, and boats. Composite materials are widely used to construct various aircraft components, such as wings, cabins, and control surfaces.[5–9]

Composite materials can serve as replacements for super alloys in certain instances. Fiber-reinforced ceramics can enhance the ductility of brittle ceramics. This is an exemplary demonstration of integrating various material characteristics to achieve a more optimal combination. Composite materials also find application in various other areas of aircraft engines.[6,10–14]

Composite materials are utilized in wind turbine blades due to their favorable characteristics, such as low inertia, weight, and strength. During instances of severe wind conditions, the blades must possess sufficient flexibility in order to endure the forces. Continuous fibers enable them to achieve this capability.[15–17]

Composite materials exhibit various failure modes, although most of them only partially impact the structural integrity of the construction. By following this approach, users can identify the failure in advance, thus preventing it from becoming catastrophic.

Therefore, composite material designs offer a higher level of safety compared to designs made from a single material.[18–21]

Strain-based measurements can facilitate Non-Destructive Testing for predictive maintenance due to the presence of partial failure specifications. For instance, Fiber Bragg grating sensors are used in aircraft wings. The sensor assists the maintenance crew in determining the loads that have affected the aircraft during flight and landing. By implementing this approach, it would effectively mitigate the risk of any failures leading to casualties.[21–23]

Table 1.1. Types of Matrixes for Composite Materials. (Source: Zweben 2015[24])

REINFORCEMENT	MATRIX			
	Polymer	Metal	Ceramic	Carbon
Polymer	X	X	X	X
Metal	X	X	X	X
Ceramic	X	X	X	X
Carbon	X		X	X

The diverse types of composite materials can be categorized in multiple ways. The material in which the reinforcement material is embedded is referred to as the matrix. One method of categorizing composites is by their matrix type. As can be seen from Table 1.1[24], mainly, there are 4 types of matrix mediums. This study focused on polymer matrix composites. The composites can also be grouped by their reinforcement materials, as can be seen from Figure 1.1[24]. In this study, the main topic was continuous fiber-reinforced composite materials.

1.1. Focus of This Study

The manufacturing process of composite materials varies. In continuous fiber composite materials, the continuous fibers are shaped to match the geometry to address the limitations of draping. As the geometric intricacies escalate, it is necessary to augment the discontinuous regions; otherwise, the alteration in fiber directions results in a diminished calculated strength of the directional force.[25,26]

Discontinuities, however, result in regions of the matrix that are abundant in matrix material. In some cases, these regions may be filled with discontinuous fibers. Nevertheless, the fiber ratio in these regions cannot be accurately anticipated, so these calculations should not consider that. It is important to note that not calculating these regions' fiber content can enhance the strength, but it can be disregarded for safety reasons. Misaligning the discontinuous regions could potentially mitigate the effects of these regions.
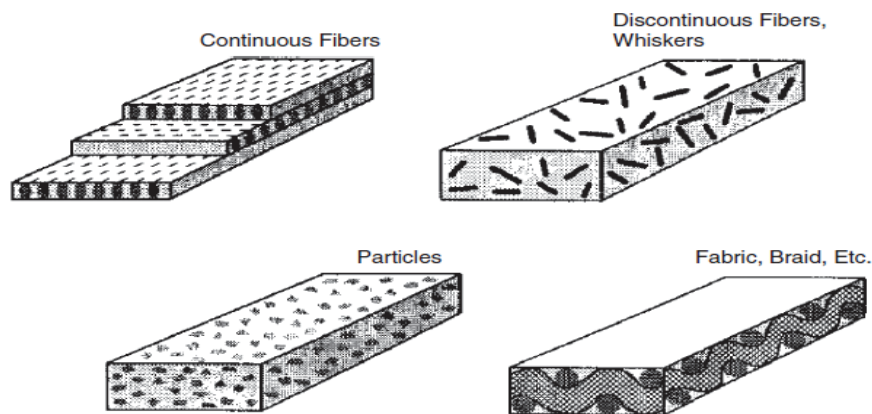
Figure 1.1. Types of Reinforcements in Composite Materials. (Source: Zweben 2015[24])
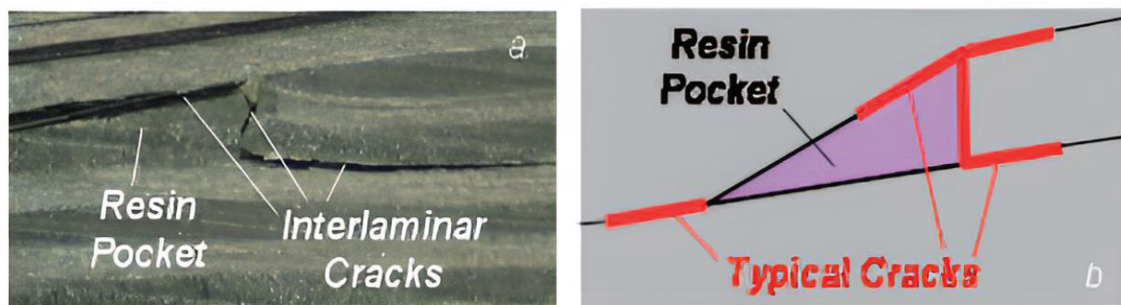
Figure 1.2. Resin Pockets and Crack Initiation (Source Butler 2011[27])

To manufacture leaf springs with varying widths and thicknesses, it is necessary to utilize a preform that does not contain stitches. There are several approaches to this. However, the variable thickness necessitates using patches between the continuous laminae. These areas are known as resin pockets and are typically the locations where cracks begin, as can be observed on Figure 1.2[27].

This study aims to investigate diverse types of discontinuities. In an example, the variable width spring tips can be seen on Figure 1.3[28]. This thickness change requires drop-offs that induce interply discontinuities.

The discontinuities in the fiber are made in order to cover the shape of the part with the limitations of the draping. The draping in fabric-based composite production, including prepreg materials, is a limiting factor. The draping behavior of UD-NCF (Unidirectional-Non crimped Fabrics) has not been investigated as much as that of woven fabrics. Yet a study by F. J. Schirmaier[29] et al. show the limitations of this type of material.
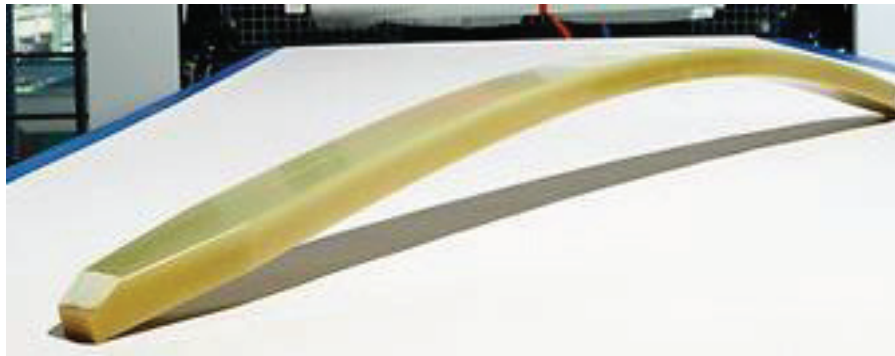
Figure 1.3. Variable Width and Thickness Composite Leaf Spring.
(Source: Henkel 2013[28])

As can be seen on Figure 1.4[29] that during the shaping process the fibers might fill the shape if the shape get complex. Due to this phenomenon, continuous fibers are cut into different geometric shapes.

As can be seen on Figure 1.5[30], some geometries cannot be covered with continuous fibers that spread evenly. The black parts are pentagons, and the white ones are hexagons. This method is implemented due to the material limitations of football fabric's drapability.

1.2. Aim of the Study

The objective of this study is to thoroughly investigate the influence of structural discontinuities on the mechanical characteristics of composite beams made of glass fiber-reinforced polymer (GFRP). The study aims to categorize these discontinuities as inter-ply or intra-ply types, which occur within the composite layers before they are fully cured. Mechanical properties are evaluated by performing quasi-static three-point bending tests utilizing servo-hydraulic actuators. The experimental results are compared with computational analysis (CAE) by evaluating the sectional fiber volume fractions. This evaluation is supplemented by microscopic analysis of local discontinuities.

This study provides significant insights into the relationship between internal structural defects, resin distribution, and the mechanical properties and reliability of composite materials. The goal of this project is to enhance our understanding of composite beam design and manufacturing processes in engineering by combining experimental findings, computational modeling, and microscopic analysis.
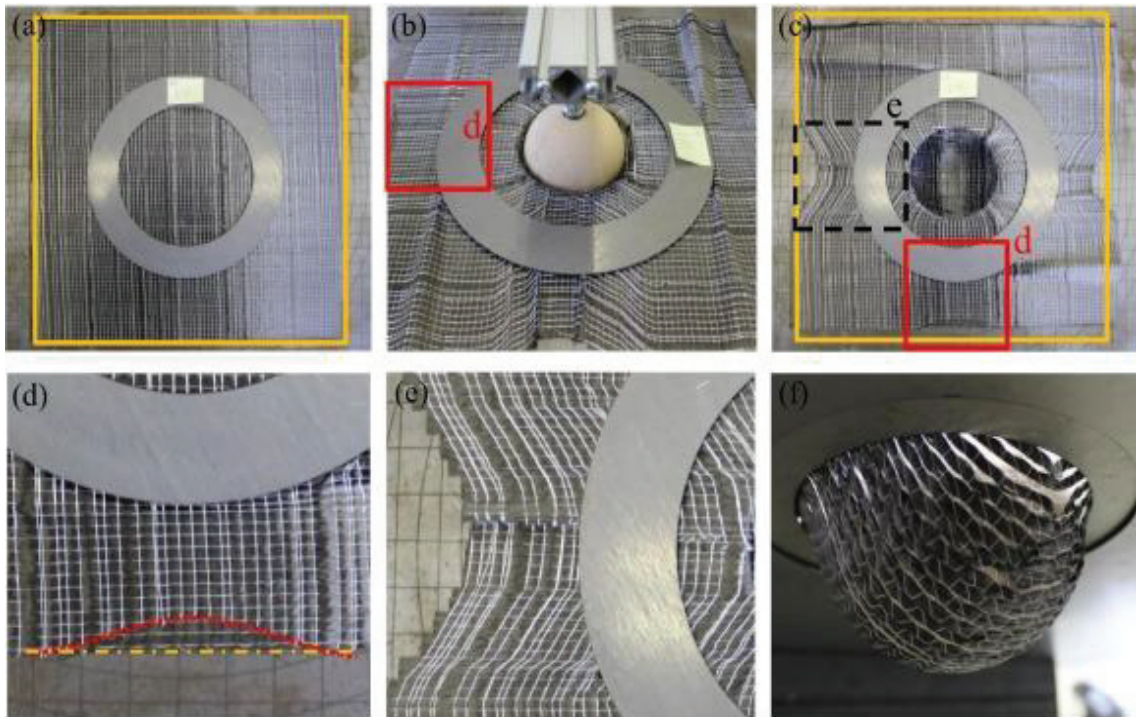
Figure 1.4. Hemisphere Test of UD-NCF. (a) top-view before testing; (b) side view after testing; (c) top-view after testing with removed hemisphere forming tool; (d) slippage between glass fibers and carbon fibers due to forming; (e) shear deformation between carbon fibers due to forming; (f) gapping between carbon fibers on hemisphere due to forming (bottom view). (Source: Schirmaier 2016[29])

1.2.1. Characterization of Discontinuities

The process involves categorizing discontinuities within composite layers as inter-ply or intra-ply based on location and nature. Introducing discontinuities before curing to replicate authentic manufacturing conditions.
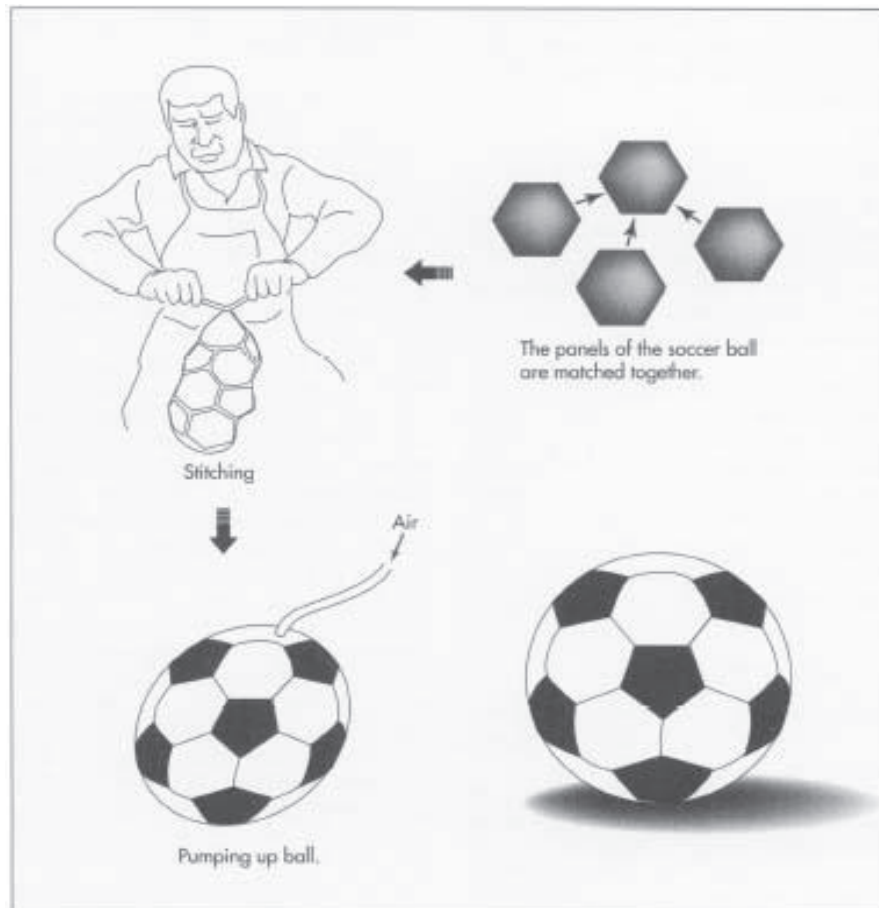
Figure 1.5. Production of Football Geometry. (Source: Madehow 2024[30])

1.2.2. Experimental Evaluation

Performing quasi-static three-point bending tests utilizing servo-hydraulic actuators to quantify mechanical properties. Examining the impact of discontinuities on structural performance, with a specific emphasis on strength, stiffness, and failure mechanisms.

1.2.3. Computational Analysis

Computer-aided engineering (CAE) involves using simulations to predict the mechanical behavior of a system. This analysis focuses on sectional fiber volume fractions and stress distributions. Verifying empirical observations with computational forecasts to improve comprehension and predictive aptitude.

1.2.4. Microscopic Analysis

Utilizing microscopic techniques to analyze local discontinuities, resin distribution, and fiber arrangement within the composite structure. Examining the relationship between small-scale observations and large-scale mechanical properties in order to understand the impact of internal defects.

1.2.5. Impact on Material Durability

Detecting areas with a high concentration of resin and discoloration caused by the heat released during the curing process suggests a decrease in mechanical strength. Evaluating the structural consequences of resin gaps and fiber discontinuities on the enduring dependability of GFRP composite components.

1.2.6. Engineering Implications

Emphasizing the crucial significance of material composition and manufacturing quality in determining structural integrity and performance. Offering analysis on design factors to reduce heat-induced resin gaps and improve the dependability of composite materials in engineering applications.

1.3. Thesis Outline

The thesis aims to thoroughly examine the impact of structural discontinuities on the mechanical characteristics of glass fiber-reinforced polymer (GFRP) composite beams.

CHAPTER 1, provides an overview of the context and reasons behind the study, highlighting the importance of comprehending these impacts in composite materials engineering. The document delineates the precise goals of categorizing discontinuities as either inter-ply or intra-ply within composite layers before curing.

CHAPTER 2, comprehensively examines the existing literature on composite materials. It explores distinct types of discontinuities and the computational methods utilized to analyze their impact on mechanical properties. This chapter establishes the

fundamental basis for comprehending the existing deficiencies in knowledge and the contributions made by research.

CHAPTER 3, provides a comprehensive description of the experimental methodology used. This includes the criteria for selecting materials, the techniques for introducing discontinuities, and the setup for conducting three-point bending quasi-static tests using servo-hydraulic actuators. Additionally, the article explains the utilization of microscopic analysis techniques to investigate specific discontinuity and resin distribution areas.

CHAPTER 4, delves into computational analysis (CAE), explaining simulation principles, setup configurations, and predictive modeling of mechanical behavior. It compares CAE predictions with experimental results to validate findings and enhance understanding of structural performance influenced by internal flaws.

CHAPTER 5, concludes the experimental results presented and discussed previously, focusing on analyzing how various discontinuities affect mechanical properties such as strength, stiffness, and durability. The composite beam design and manufacturing analysis have been conducted to evaluate the consequences and importance of enhancing material dependability and effectiveness.

1.4. Novelty of the Thesis

This thesis investigates the discontinuous areas present in continuous glass fiber composites. As far as we know, the fiber reinforcements are either fully continuous or discontinuous. In some studies, like those done by M. Fikry[31] et al. carbon fiber reinforced polymers investigated glass fiber is preferred in specific applications, such as leaf springs, because it is less expensive, more resistant to galvanic corrosion, and has higher impact resistance [32].

Several studies have examined composite shells that include cutouts. Dewangan[33–38] et al. conducted a series of studies that shed light on the impact of intra-ply discontinuities on vibration levels. The force capacity of thick beams under quasi-static conditions has not been investigated.

Non-crimp Fabric (NCF) is increasingly used in materials because it offers advantages compared to woven fabrics. NCFs have increased strength and stiffness since they are aligned in directions without any crimping. This alignment helps reduce stress

points and weaknesses that usually happen where fabrics intersect. Additionally, NCF allows for adjusting the orientation of fibers, resulting in materials with customized properties to meet performance needs. The porous structure of NCFs aids resin flow during the infusion process, ensuring saturation and an even spread of resin. This ultimately improves the quality of parts by minimizing defects and voids. Incorporating NCF materials can enhance performance, leading to weight savings, which is particularly beneficial for industries like aerospace and automotive. Despite costs, enhanced efficiency, reduced material usage, and fewer production mistakes make Non-crimp Fabrics a financially advantageous choice in the long term.[39–42]

This study examines the properties and traits of E-glass continuous unidirectional non-crimp fiber reinforced epoxy composites. The study entailed comparing non-continuous samples and analyzing the influence of interply and intraply discontinuities on durability tests.

Material testing was conducted at the coupon level in our research to establish baseline material characteristics. We then produced two full-scale models of intra-ply composite samples using layers of glass fiber-reinforced prepregs. Using a computer numeric control cutter and manual application methods, the samples were deliberately exposed to discontinuities. We conducted 3-point bending quasi-static tests on full-scale specimens using servo-hydraulic actuators to assess how these discontinuities affect the mechanical properties of the composite laminate.

In this study, experimental results with predictions generated by computational analysis focus on evaluating sectional fiber volume fraction using CAE models. Microscopic analysis identifies local discontinuities and improves the understanding obtained from the computational models. This thorough approach clarified the complex connection between internal structural inconsistencies and the mechanical properties of continuous glass fiber-reinforced materials.

The formation of resin-rich zones in dislocation areas during the exothermic curing process is a significant observation. The zones show a clear color change in the resin, transitioning from transparent to yellow-brown Carbonyl Formation, and are linked to reduced mechanical strength.[2] The results of our research provide insight into the mechanisms that explain these phenomena and enhance the overall comprehension of composite material behavior. So, the study provides a valuable contribution to composite materials research by offering insights that can help optimize manufacturing processes and enhance the structural reliability of composite parts.

CHAPTER 2

FUNDAMENTAL CONCEPT AND LITERATURE

Composite materials are widely used in different industries. During the development of production methods, some advantages and disadvantages emerged. In this section, the literature is investigated to summarize possible outcomes of the different methods and clarify the requirements of this study.

2.1. Introduction to Composite Materials

There are multiple production methods and alternative materials to produce composite materials. To use the correct material and process for the specific application, the effects of the selections must be studied thoroughly.

2.1.1. Definition of Composite Materials

Composite materials have become promising and central to engineering and material sciences research since the mid-20th century. The exponential expansion and widespread acceptance of composite materials can be ascribed to their outstanding structural and mechanical characteristics and their resilience against chemicals, fire, corrosion, and wear. These materials exhibit a distinctive blend of these beneficial characteristics.[43,44] Composite materials are extensively used in diverse industries such as aerospace, automotive, marine, wind and thermal power generation, civil construction, and telecommunications, owing to their notable properties.[43–45]

Composite materials, which consist of two or more constituent materials with distinct physical or chemical properties, are a highly significant and diverse category of engineering materials. Specific criteria must be met for a material to be classified as a composite. The composition must comprise at least two physically distinct materials that can be mechanically separated. When combined, it generates a different material with exceptional and optimal characteristics. It can be created by combining the individual materials to allow for the dispersion of one material within the other, resulting in optimal properties. It exhibits distinct qualities that are superior to the individual components.[46]

10

Composite materials typically consist of two primary phases: the matrix and the reinforcement.

The matrix is the dominant phase that encloses and surrounds the reinforcement phase. Reinforcement can manifest as particles, fibers, or whiskers made from either natural or synthetic materials.

The matrix in composites is typically considered to be a less intense and less stiff phase, while the reinforcement phase is more robust and stiffer. The reinforcement phase carries the applied load to the material.[47]

2.1.2. Classification of Composite Materials

The properties of each component have an impact on the overall properties of composites. Therefore, it is necessary to study their classification and distinct properties thoroughly. Classifying composites based on matrix and reinforcement material is widely and commonly used.

2.1.2.1. Composite Materials by Composition

Ceramic matrix composites (CMCs) consist of ceramic reinforcements and a ceramic matrix. Ceramic materials possess inherent resistance to oxidation and degradation when exposed to high temperatures, making them highly suitable for use in high-temperature applications, particularly for components in gas turbine engines of automobiles and aircraft.

Nevertheless, their fracture toughness values exhibit a significant deficiency. This makes them brittle and susceptible to catastrophic failures when flaws are present. Furthermore, they are highly vulnerable to thermal shock and prone to damage during manufacturing and use. Ceramic Matrix Composites (CMCs) are engineered materials that address the drawbacks of monolithic ceramics by incorporating ceramic reinforcement in the form of particles, fibers, or whiskers embedded within a ceramic matrix. This allows CMCs to take advantage of the excellent high-temperature strength and resistance to environmental conditions offered by ceramic materials while minimizing the risk of catastrophic failure.

Metal matrix composites (MMCs) are composite materials of a metallic matrix

and dispersed ceramics, such as oxides, carbides, or metallic reinforcement. Some examples of this category of composites include directionally solidified eutectic alloys, oxide dispersion strengthened alloys, Al-Si eutectic casting alloys, pearlitic steel, and two-phase lamellar alloys like gamma TiAl. Metal matrix composites (MMCs) exhibit a synergistic blend of physical and mechanical properties. They demonstrate exceptional thermal and electrical conductivity, robust resistance to harsh environments, impressive resistance to impact and erosion, and notable properties in terms of fatigue and fracture.

Moreover, MMCs provide enhanced strength and rigidity compared to the matrix alloy, outstanding resistance to wear, and a decreased coefficient of thermal expansion. They have been widely employed in diverse applications, such as transportation, thermal management, and aerospace.[48]

Polymer matrix composites (PMCs) comprise a polymer matrix, either thermoplastic or thermoset, and reinforcement materials such as carbon, glass, aramid, and metal fibers. Thermosets are favored over thermoplastics due to their superior strength and higher resistance to elevated temperatures. PMCs are extensively employed in diverse composite applications and are manufactured in significant volumes owing to their convenient production process and cost-effectiveness. The integration of high-performance fibers such as carbon, boron, and aramid, along with the utilization of advanced matrix materials, has led to the development of engineering structural materials.

Glass fiber-reinforced polymers are the most significant and widespread polymer matrix composites (PMCs). Carbon fiber-reinforced polymer matrix composites (PMCs) are widely recognized as the leading structural composites, especially in the aerospace industry.[43,44,47,49,50]

2.1.2.2. Composites Utilizing Reinforcement Geometry

Particle-reinforced composites, which can be divided into subclasses of large-particle and dispersion-strengthened composites, are a specific type of composite material categorized according to the shape of the reinforcement. These two composites vary in their methods of strengthening. When discussing composites reinforced with large particles, "large" indicates that the interaction between the particles and the matrix occurs at the atomic or molecular level.

The rigid and inflexible reinforcing particles tend to impede the movement of the

matrix phase. The matrix reallocates a fraction of the exerted stress to the particles, resulting in their contribution to bearing a portion of the load. To effectively strengthen or improve the mechanical properties of composites, it is essential to establish a strong bond at the interface between the matrix and particles.

The particles in dispersion-strengthened composites possess diameters within the nanometer range, varying from 10 to 100 nm. Strengthening occurs at the atomic or molecular level due to the interactions between particles and the matrix. In this specific category of composites, the matrix predominantly bears the majority of the applied load, while the small, dispersed particles impede the displacement of dislocations. As a result, the composites have limited ability to undergo plastic deformation, which improves their mechanical properties.[47]

Fiber-reinforced composites are widely recognized as the foremost category of composites. This composite type includes a dispersed phase comprising synthetic glass, carbon, basalt, aramid, and natural fibers. This material enhances its properties, increasing strength, rigidity, and durability against chemical corrosion, high temperatures, and wear. The main goal of designing fiber-reinforced composites is to attain a high specific strength and moduli. The fibers in composites can be classified as continuous or discontinuous, depending on their length, and can be arranged in an aligned or randomly oriented manner.[47]

Glass fiber-reinforced polymer composites have a substantial volume in total composite production. Glass fiber demonstrates a low mass and a high level of durability. It proves a comparatively high ratio of strength to weight and a moderate ratio of modulus to weight. They continue to enhance the resilience of polyester, epoxy, and phenolic resins. It is economically efficient and available in multiple formats.[49]

Carbon is a high-performance fiber material widely used to strengthen advanced polymer matrix composites due to its exceptional properties. Fiber materials with the highest specific modulus and specific strength are recognized for their capacity to retain their elevated tensile modulus and strength, even under high temperatures. They resist moisture and diverse solvents, acids, and bases. The manufacturing processes of fiber and composites are cost-effective and highly efficient. Importantly, these fibers exhibit various physical and mechanical characteristics that allow composites containing them to have specific engineered properties.[47]

2.1.2.3. Manufacturing of Fiber-Reinforced Polymer Composites

There are multiple production methods for different composites. All have distinct advantages and limitations over each other. Diverse options should be investigated to select the most suitable method.

2.1.2.3.1. Hand Layup Method

The hand layup method uses natural (I.E., hemp fiber) and synthetic (carbon, glass, etc.) fibers to manufacture composites. This manufacturing method is the most prevalent and extensively utilized for open mold composite production. In this procedure, a thin layer of mold-release paint (gel coat) is first applied to the mold surface to prevent adhesion during the process.

Fiber preforms are then placed in the open mold. Next, polymer resin is poured or applied onto a reinforcement material using a brush. The roller applies a uniform load to improve the interaction between the layers of reinforcement and the matrix materials. Furthermore, it eliminates the air in the interface between the matrix and reinforcement. Ultimately, the mold is retained to allow the resin to undergo the curing process, typically at ambient temperature, although heat may be employed to guarantee an effective curing procedure.[43,44,51]

2.1.2.3.2. Vacuum Bag Molding

This technique involves using a pliable film made of nylon, polyethylene, or polyvinyl alcohol (PVA) to cover and seal the mold. Typically, this method is conducted with the help of the hand layup method. Firstly, the laminate is created using the hand layup method. Subsequently, it is positioned between the vacuum bag and the mold to facilitate the infusion of fibers into the matrix material. A vacuum pump extracts the air from the space between the mold and the vacuum bag.[43]

2.1.2.3.3.Compression Molding

This method utilizes preheated molds mounted on a hydraulic or mechanical press. Figure 2.1[52] illustrates the sequential process of compression molding.[52,53] Firstly, a pre-cut reinforcement from pre-impregnated composite material is inserted into the mold cavity. Prepreg refers to a type of material used in the composite industry. It consists of continuous fiber reinforcement that has been impregnated with a polymer resin but has not been fully cured.

Next, the mold is sealed, and the components are compressed to achieve the desired form. The material undergoes compaction and curing by applying pressure and heat to its interior. Compression molding provides numerous benefits, including precise detailing for complex shapes, quick cycle time, high productivity, and automated processes with dimensional stability.[43,47,51]
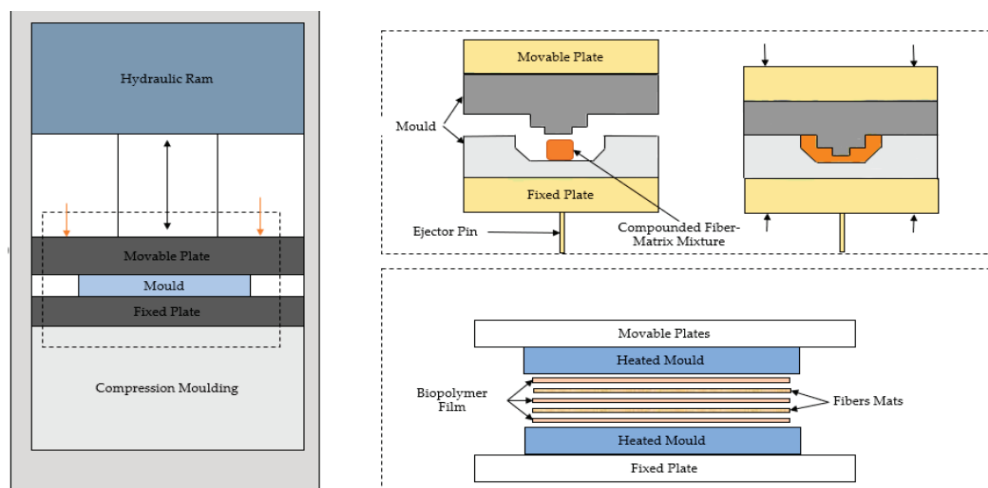
Figure 2.1. Compression Molding Diagram. (Source: Sanivada 2020[52])

2.1.2.3.4. Pultrusion

The pultrusion method fabricates components with continuous lengths and a consistent cross-sectional shape, such as rods, tubes, and beams. This method involves the initial impregnation of constant fiber bundles with resin, then pulling them through a die that preforms them into the desired shape. The saturated material is subsequently extruded from the heated closed die and undergoes continuous pulling through the die. The resin matrix is initiated to cure this heated die. Tubes and hollow sections are created using center mandrels or inserted hollow cores.

This method is a perpetual process and can be easily automated, allowing for a diverse range of shapes to be achieved. Nevertheless, the rates of production are comparatively elevated.[47,51]

2.1.2.3.5. Filament Winding

Filament winding is a cost-reducing process that is both continuous and self-automated. This technique involves the precise arrangement of continuous fibers in a predetermined configuration to create a hollow structure. Hence, it is advantageous to fabricate both axisymmetric and specific non-axisymmetric composite components, such as pipe bends. This method involves feeding continuous prepreg sheets, roving, or monofilament through a resin bath. Subsequently, they are wound onto a rotating mandrel in specific orientations. Once the necessary number of layers has been applied, the mandrel is extracted, resulting in the desired final geometric shape. Subsequently, the curing process is initiated.[44,47,51]

2.1.2.3.6. Resin Transfer Molding (RTM)

In the Resin Transfer Molding (RTM) process, fiber reinforcement mats are positioned at the base of the mold. Subsequently, resin that has been preheated is introduced into the mold under pressure via an injector. RTM enables diverse combinations of fiber material and its orientation, including 3D reinforcements.

Furthermore, this method produces composite structural components with exceptional quality, strength, and surface finish.[44] This method is another way of serially producing leaf springs.

2.1.2.3.7. Vacuum-Assisted Resin Transfer Molding (VARTM)

VARTM is a composite manufacturing technique that involves resin transfer, similar to RTM. Nevertheless, this technique consists of using a vacuum for the injection process. Fibers are arranged on a mold, and a perforated tube is inserted between the vacuum bag and the resin container.

A vacuum draws the resin through the perforated tubes, consolidating the laminate

structure by binding it with the fibers. Composite structures can be achieved without excess air by drawing resin into the cavity under a vacuum. Furthermore, it enables accurate tolerances and intricate shaping. Consequently, it is a widely used manufacturing technique for producing large objects such as boat hulls and wind turbine blades.[44,51]

2.1.2.3.8. Prepreg-Based Production

Prepregs are manufactured using diverse techniques, each offering distinct advantages and uses. The solvent-based technique entails dissolving the resin in a solvent to decrease its viscosity. The fibers are immersed in the solution to ensure complete impregnation, after which the solvent is evaporated, resulting in the resin being deposited onto the fibers. This technique offers exceptional resin infiltration and even dispersion, although it necessitates solvent recovery systems and longer processing durations due to the requirement for solvent evaporation.

The hot-melt method entails the fusion of the resin, which is then directly applied to the fibers, bypassing the need for solvents. In this method, fibers were impregnated with resin via pressure and heat to generate the prepreg. A siliconized substrate (carrier paper) pre-laminated to a certain thickness of epoxy.

The thickness can be adjusted via some different methods, one of which is a doctor blade. The doctor blade and doctor cylinder play roles in coating processes across various industries. A doctor blade is a tool that applies an adjustable layer of coating material, offering flexibility and cost-effectiveness, making it well-suited for tasks like printing and laminating. On the other hand, a doctor cylinder is a rotating cylinder used for coatings at high speeds, particularly beneficial for large-scale production in industries such as paper, board, and textiles due to its durability and efficiency. While doctor blades provide control and easy maintenance, doctor cylinders shine in scenarios requiring throughput by ensuring consistent coatings over extensive areas. The selection between the two depends on process needs like coating precision, application speed, and material characteristics.[54,55]

The blade scrapes off the excess resin from a drum; the hot resin-coated drum is then pressed over the siliconized paper for it to be coated. A comb was used to spread the fibers evenly; this step was essential to induce equal material characteristics along the same axis. The uniformly spread fibers were sandwiched between two resin-coated

papers. Again, the fibers were infused with heat and pressure with the resin between the heating and compacting rollers. The coating paper was nonelastic and stiff to drape, so it could be replaced with backing paper for easier handling. In the produced samples, one side of the paper was replaced with a backing paper.[56] Fibers are guided through heated rollers coated with molten resin, resulting in the even distribution of resin. This approach is more expedient and ecologically sustainable, obviating the necessity for solvents. Also, uniform quality should be ensured without any gaps.[56,57]

The film stacking technique entails arranging pre-prepared resin films onto fibers while maintaining strict control over temperature and pressure. This method enables meticulous regulation of the amount of resin present and is compatible with a wide range of resin and fiber combinations. Nevertheless, resin film preparation necessitates supplementary procedures and may entail intricate machinery, posing a potential disadvantage in production efficiency and cost.[58]

The solution coating method entails threading fibers through a resin solution containing a solvent and subjecting them to heat to eliminate the solvent. This technique is efficient for resins with low viscosity and ensures thorough saturation of the fibers.

However, it necessitates the management of solvents and results in longer processing durations due to the evaporation of solvents. This procedure generally entails immersing the material in a solution and using metering rolls to achieve the desired resin content.[58]

The selection of a method is determined by various factors such as the type of resin, desired properties of the product, environmental concerns, and production efficiency. The solvent-based technique is well-suited for intricate resin systems, whereas the hot-melt technique is preferred for its rapidity and ecological advantages. The film stacking method provides meticulous control for specific applications, while the solution coating method is appropriate for resins with low viscosity.[56,58]

Before starting the manufacturing process using prepregs, it is essential to cut the prepreg material to the desired size. Place the material into a mold. Expose it to heat and pressure. Methods like oven or autoclave curing ensure heat and pressure distribution, while vacuum bagging removes the air and compresses the layers.

Compression molding is another approach where high pressures and temperatures shape the prepreg. Each method ensures the creation of quality composite parts suitable for challenging applications in aerospace, automotive, and other industries.

2.2. Types of Discontinuities in Composite Structures

Composite materials are widely used in aerospace, automotive, and other high-performance industries because of their properties, like high strength-to-weight ratios, stiffness, and resistance to environmental wear. However, these materials may have imperfections that can significantly influence their effectiveness, durability, and safety. These imperfections often result from how the materials are made, handled, or used.

When engineers design and create components, they face challenges related to shape constraints and the necessity for thickness changes to enhance structural efficiency and reduce weight. These limitations can worsen imperfections within the material. Recognizing the types of imperfections and their effects is essential for improving the design of materials, manufacturing processes, and quality assurance.

2.2.1. Voids

Air pockets, known as voids, can get stuck in the material while it is being made. These empty spots become stress points, weakening the materials' strength and stiffness. Voids usually happen when the resin does not thoroughly soak into the material or when it does not cure properly.

Detecting and fixing gaps or empty areas is crucial to solid and stable structures.[7,33,59] Interactions between fibers and matrices and areas of small empty spaces. Microscopic voids are visible in the Figure 2.2[59].

2.2.2. Delaminations

Delaminations refer to the process of layers separating within a laminated composite. This can arise due to manufacturing flaws, impacts, or thermal cycling. Delaminations undermine the ability of the composite to bear loads and can result in disastrous failure if not identified and fixed. In aerospace applications, they pose significant challenges, especially when it comes to ensuring the utmost structural integrity. A delamination induced by impact can be seen in Figure 2.3[3].

Delaminations refer to the process of layers separating within a laminated composite. This can arise due to manufacturing flaws, impacts, or thermal cycling.

Delaminations undermine the ability of the composite to bear loads and can result in disastrous failure if not identified and fixed. In aerospace applications, they pose significant challenges, especially when it comes to ensuring the utmost structural integrity.[3,59]
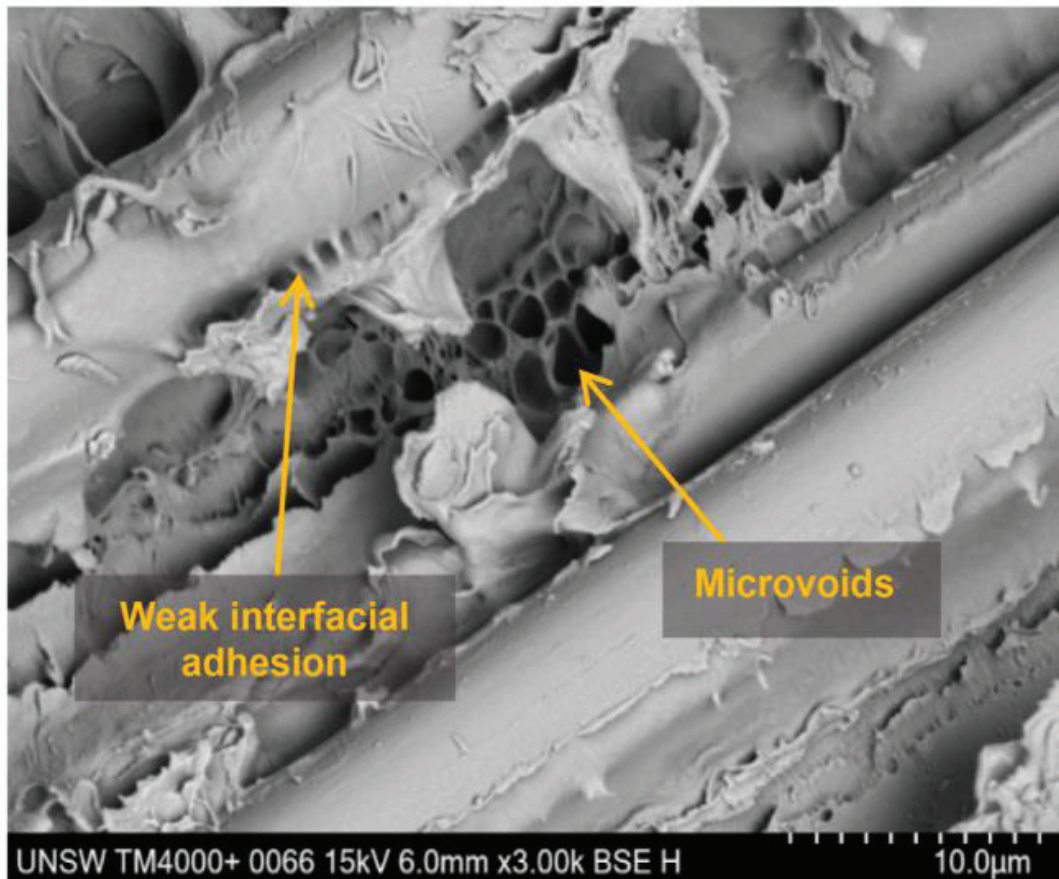
Figure 2.2. Voids in Composite Materials. (Source: Shafaq 2023[59])

2.2.3. Fiber-Matrix Debonding

The disconnection arises when the fiber detaches from the matrix, thereby affecting the efficiency of load transfer and compromising the strength of the composites. It can occur due to bonding during production or when subjected to stress.[3,31]

2.2.4. Cracks

Cracks in composite materials can arise from mechanical loading, impact, or environmental influences. The propagation of these cracks can ultimately fail. The cracks

can be categorized as matrix, fiber, or interfacial based on their specific location. Early detection of cracks is crucial as they have the potential to propagate under stress rapidly.[3,31]
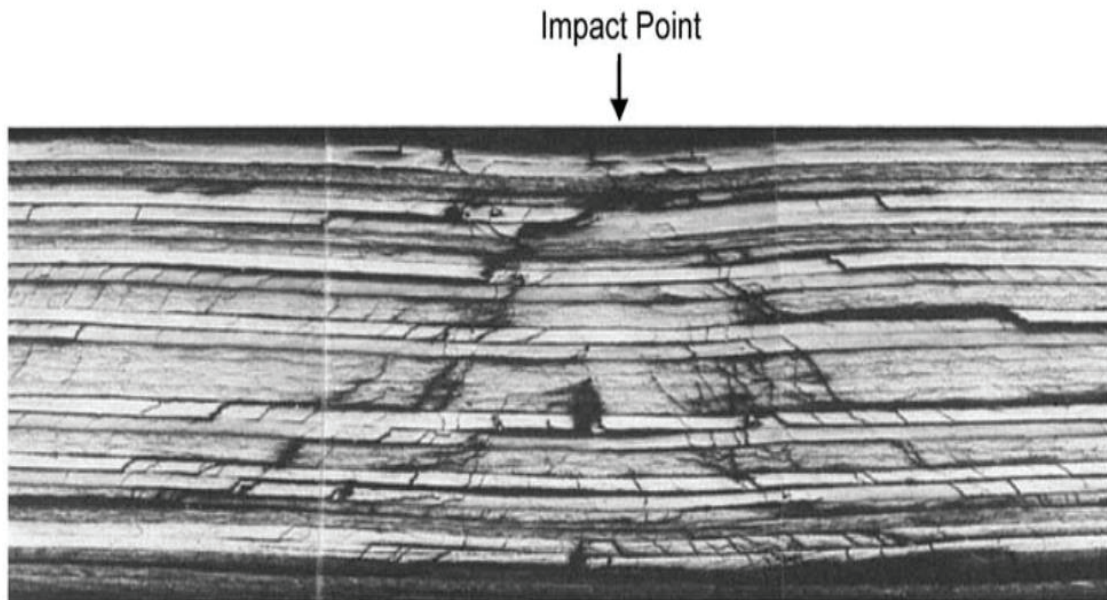
Carbon/Epoxy
30 ft-lb Impact
Diagonal Cracks and Extensive Delaminations

Figure 2.3. Impact Initiated Delamination. (Source: Campbell 2010[3])

2.2.5. Foreign Inclusions

Unwanted elements, or inclusions, can be mixed into the material during production. These foreign particles create stress points, lowering the composites' effectiveness. Such inclusions may come from the surroundings or impurities in the manufacturing process.[47,60]

2.2.6. Impact Damage

Damage caused by an impact can lead to issues like cracking in the material, breaking of fibers, and separating layers. This kind of damage can be tricky as it may not be easily seen on the surface but can significantly weaken the strength of the material.[47,60,61]

2.2.7. Ply Waviness

The term ply waviness or fiber waviness describes the misalignment of fibers in the layers of a material, as seen in Figure 2.4[59]. This misalignment often occurs due to mishandling during the manufacturing process. Ply waviness can cause a decrease in strength and stiffness. It is particularly problematic in situations that demand levels of accuracy and strength.[29,62]
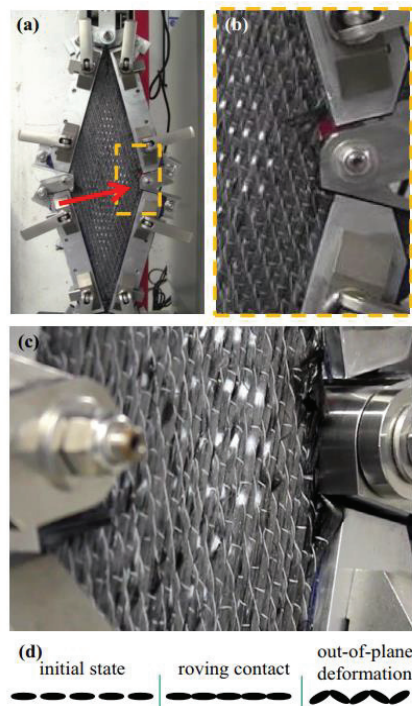
Figure 2.4. Ply Waviness. Testing the picture frame deformation of UD NCF entails the following steps: (a) fully examining the front view; (b) closely inspecting a magnified rectangle within the view; (c) observing the side view, specifically towards the arrow in the full front view; (d) demonstrating the buckling of carbon fibers due to compressive strains that are perpendicular to them. (Source: Shafaq 2023[59])

2.2.8. Hygrothermal Effects

Exposure to both moisture and high temperatures, known as aging, can create microcracks and cause material debonding. Such damage can deteriorate the materials' characteristics. Shorten its lifespan over time

The behavior as seen in Figure 2.5[63] resembles voids mentioned in 2.2.1. The main difference is the voids mentioned in 2.2.1 are created before and during the curing process, yet hygrothermal effects are formed afterward.[63]
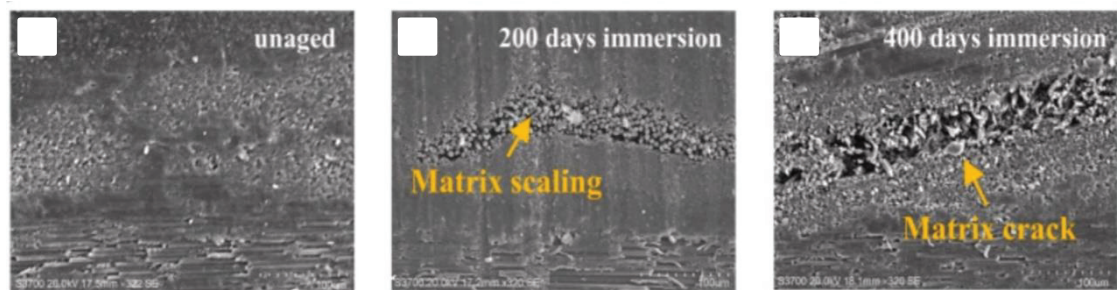
Figure 2.5. Long-Term Exposure in Hygrothermal Environment of Laminated Composites. (Source: Liu 2024[63])

2.3. Discontinuity Types of Fibers

The discontinuities mentioned above are fiber-resin and within-resin discontinuities. Yet another class of discontinuities can be explained by fiber alignment. This type mainly forms continuous fiber composites rather than chapped fiber composites.

It can be classified into two main sections: inter-ply and intraply. In this study, these effects are being compared to a fully continuous sample. As mentioned above, current studies have been conducted with Carbon fiber-based materials, yet this study was conducted with Unidirectional glass fiber materials.

2.3.1. Intraply Discontinuities

Intraply discontinuities can occur within a material layer, such as fiber fractures, cracks, and separation between the fibers and matrix. Hybrid composites containing fibers in the layer may experience unique internal disruptions due to the varying mechanical properties of the fibers. These disruptions can significantly affect the mechanical properties at a localized level and the overall performance of the composite material. They can also be placed due to geometrical limitations during the production process.[25,47]

This type of discontinuity was demonstrated with two different samples. Sample#4 and Sample#5 are specially designed to investigate this type of discontinuity.

This type of discontinuity is mainly required to produce beams that have changed in width. This method can narrow the springs' endpoints in the serial production of leaf springs. In this type of discontinuity, some of the continuous fibers are cut, yet some are kept connected. This weakens the total fiber strength since discontinuous fibers function as chopped fibers.

2.3.2. Interply Discontinuities

Discontinuities can arise within the layers of materials, such as delamination and cracks between the laminates. These interruptions are especially crucial in composites with varying fiber types across layers, as they can create stress patterns. It is vital to address these discontinuities to guarantee the lasting dependability of composites utilized in engineering fields.[64]

This type of discontinuity is especially used during variable thickness requirements. By using short layers within continuous layers, the thickness of the total part can be increased. In this study, 3 sample types were suggested for resembling this type of discontinuity.

2.3.3. Applications and Implications

It is essential to grasp the types of gaps and how they impact the design of composite structures and the enhancement of manufacturing methods. For instance, spotting and addressing discontinuities can avert breakdowns in aerospace settings where reliability and efficiency are vital. In the sector, reducing these imperfections can boost the resilience and safety of parts. Upholding top-notch composites via quality checks and cutting-edge detection methods is essential to upholding safety and performance benchmarks in these industries.[35–38]

In this study, thick beams made of unidirectional glass fiber composite prepreg have been used. Current literature has shell-based studies, and carbon fiber materials have been studied. This study is focused on determining the root causes of failure modes on the thick beams of composites.

CHAPTER 3

EXPERIMENTAL PROCEDURES

This study has been conducted to compare serial production methods. The production recipes, materials, molds, and machinery are the same as those of the serially produced sample. The serially produced sample is fully continuous; thus, it is called Sample#C in this dissertation. Five additional samples that resemble different classes and subclasses of discontinuities were investigated. As mentioned in previous chapters, the investigated discontinuities are required during production due to geometrical limitations, not post-cure discontinuities.

The experimental method started with a coupon-level material test to determine the characteristics of the prepreg material. The selected material is unidirectional glass fiber prepreg. Glass is the preferred reinforcement because composite beams, like leaf springs, are prone to elastic deformation and require high elastic capacity. Compared to carbon and Kevlar, the ultimate elongation is highest for glass fiber, as can be seen Table 3.1[65]. Epoxy resins are favored for their elongation capacity with glass fiber reinforcement while producing composite leaf springs.

Table 3.1. Expected Reinforcements vs. Epoxy Resin Mechanical Properties.
(Source: Karthik 2020[65])

Properties	Carbon	Kevlar	Glass	Epoxy
Young's modulus in GPa	125–400	70–112	30–40	3.5
Tensile strength in MPa	4127	2800	3450	83
Ultimate elongation in %	2.4	2.4	3.15	4.2
Density in g/cm³	1.58	1.47	2.66	1.15
Weave type	Plain	Plain	Plain	–

Prepreg is commonly utilized in production because of its quality, easy handling, and impressive mechanical characteristics. Pre-impregnated fibers guarantee resin distribution, which contributes to creating long-lasting parts. This technique decreases space. Improves fiber alignment, leading to enhanced structural strength.

Prepreg material is also used to ease handling during the serial layup process.[56,66] Additionally, prepreg materials provide control over fiber volume percentage. Reduce waste generation, making them well suited for high-performance uses, like the aerospace and automotive sectors.[54,60]

Leaf spring-shaped full-sized beams are deliberately manufactured with defects to study their impact on their mechanical properties. These flaws replicate genuine imperfections that may occur during the manufacturing process.[25–27,29,62,67–69] The regions containing flaws are subjected to a matrix burnout test to assess the effects of these imperfections. This procedure involves incinerating the matrix material while retaining the reinforcing fibers to measure the fiber volume fraction (FVF).[70,71] The FVF, or Volume Fraction Factor, is significant in determining materials' mechanical behavior, rigidity, and durability. Accurately determining the Formation Volume Factor (FVF) is crucial for evaluating the manufacturing process's efficiency and the structure's integrity. Most of the composite structures' mechanical, thermal, and chemical characteristics can be determined by the rule of mixtures.[72,73]

In addition to the FVF test, microscopic imaging is used to investigate the discontinuity zones. This test revealed cracks and voids as well as carbonyl formation.[2] The carbonyl formation can be seen as yellow-brown discoloration and is referred to as yellowing.[2] In this study, yellowing and yellow-brown terms are used interchangeably, as well as carbonyl formation. This formation shows a reduction of mechanical capacity.

The full-size samples were subjected to a quasi-static 3-point bending flexural test. The tests have been conducted with priced servo-hydraulic actuators. The tests were conducted with displacement control and force acquisition. The results are compared with the continuous sample, Sample#C.

Computer Aided Engineering (CAE) analysis is employed to assess the correlation between the outcomes of tests and the performance of composite structures in simulations. This analysis validates our models' precision and guarantees that our simulations depict the behavior of the composites under different loads. The CAE models are constructed to resemble discontinuities inspected with microscopic imagery. The details are discussed in the following chapters.

Furthermore, fatigue tests were performed to evaluate the durability and reliability of the composites, as fatigue can significantly impact their lifespan and dependability. These tests are crucial for comprehending the impact of repeated loading on these materials' strength and mechanical properties. One of the samples failed too early

compared to other samples, Sample#3, which was outlined from fatigue tests. Materials and Prepreg Preparation

A unidirectional E-glass reinforced (UDGFR) epoxy prepreg system prepared within this study was used to fabricate the composites. The unidirectional (UD) oriented noncrimp E-Glass type 2400 Tex fiber with 1000 g/m^2 areal density was used. Prepreg materials were produced via the hot melt method, impregnating fibers with epoxy resin using pressure and heat. A siliconized substrate paper was pre-laminated to a certain thickness of epoxy. The thickness of the material was adjusted via the doctor-cylinder method.[74] The same material is used for coupon-level tests as well as full-sized beams. This material is also being used for serially produced composite leaf springs.

3.1. Coupon Level Tests

Mechanical characterization techniques mainly consist of four groups, as can be seen from Figure 3.1[75]. The tests are destructive methods using a specimen of traditional shape and dimensions prepared in compliance with D3039[76]/ STM D790[77] ASTM standards.
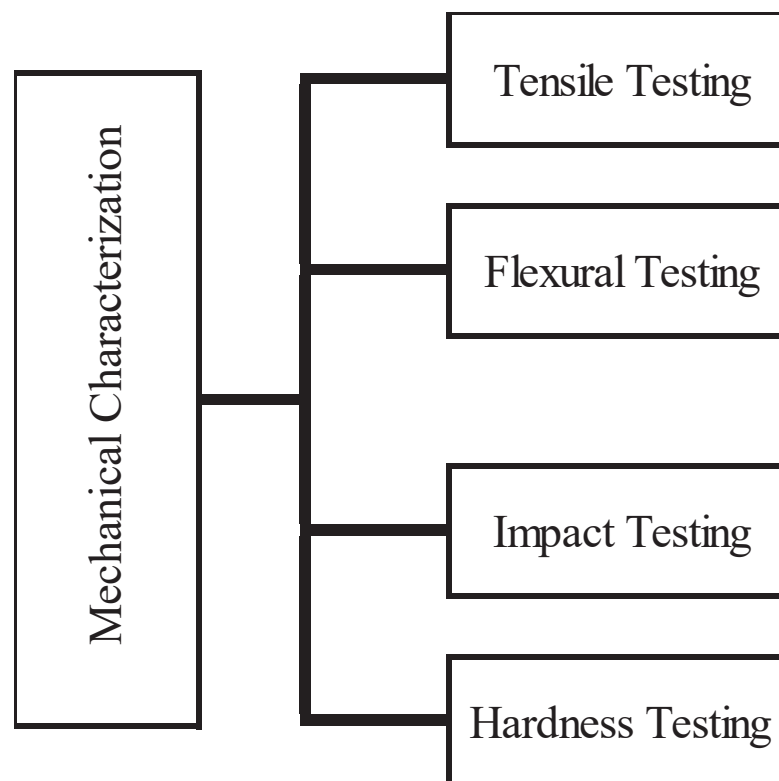
Figure 3.1. Mechanical Characterization Types. (Source: Das 2020[75])

During the tensile test, the sample midsection is narrowed to focus on the stress to induce failure. The narrow area's area is calculated and accepted as fixed during the test because only engineering values are calculated.

The stress is calculated by the Equation (3.1)[78]. The change in the elongation is measured via extensometers is used to calculate the strain via Equation (3.2)[78] a strain gauge can also be used. The tensile samples are shaped as shown in

Figure 3.2[76]. The thickness can change due to manufacturing defects and limitations, yet the area is measured for each sample.

$$\sigma = \frac{F}{A} \qquad (3.1)$$

$$\varepsilon = \frac{L - L_0}{L_0} \qquad (3.2)$$

The Young's (Elasticity) Modulus is calculated via Equation (3.3)[78]. The Young's modulus, ultimate stress, and elongation at the breakpoint are measured.[78]

$$E = \frac{\sigma}{\epsilon} \qquad (3.3)$$
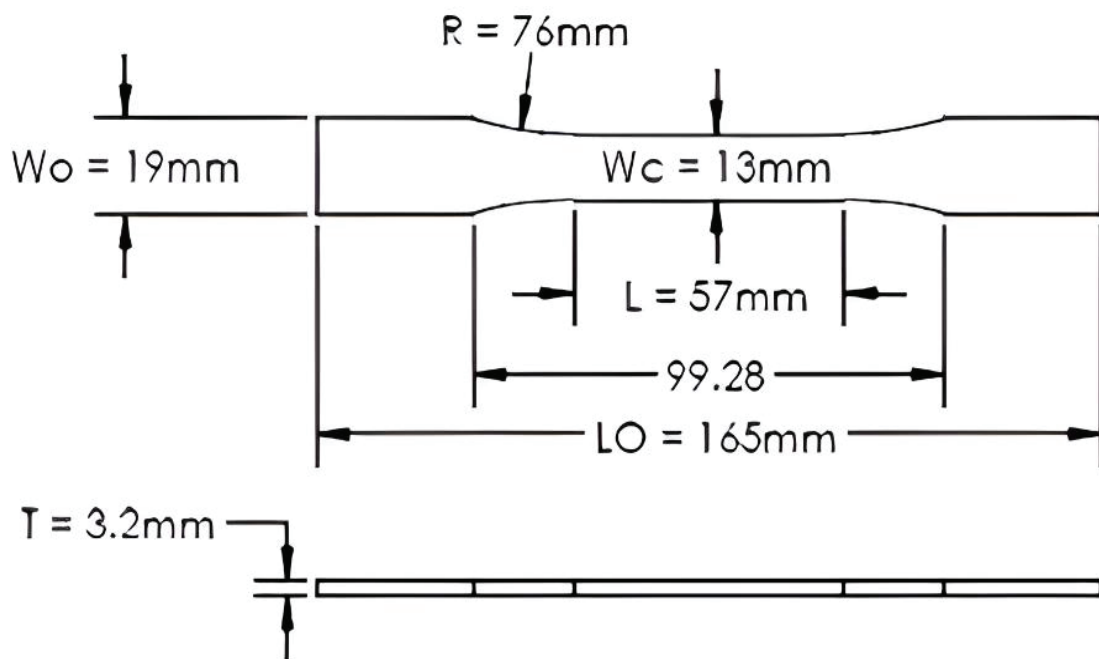
Figure 3.2. Tensile Sample Drawing. (Source: ASTM D3039[76])

The test was conducted by a tensile testing machine, as shown in Figure 3.4[79]. The figure shows that the extension meter only reads the central area. The length of the extensimeter is called gauge length and is used as L_0 in the calculations. As can be seen from Figure 3.3[80], the specimen failure follows through the body and breaks within the end tap region.
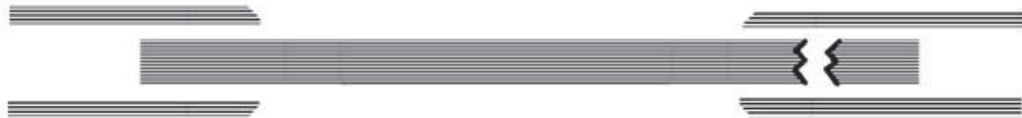
Figure 3.3. Tensile Test Sample Failed Specimen. (Source: ASTM D3039[80])

Coupon tests are performed to determine the continuous material characteristics. The test samples were produced via compression molding of prepreg material. The prepreg is an epoxy resin-based, Non-Crimp Fabric of 1000 gram per square meter (GSM) unidirectional glass fiber. The glass fiber is 2400 grams per kilometer (TEX).
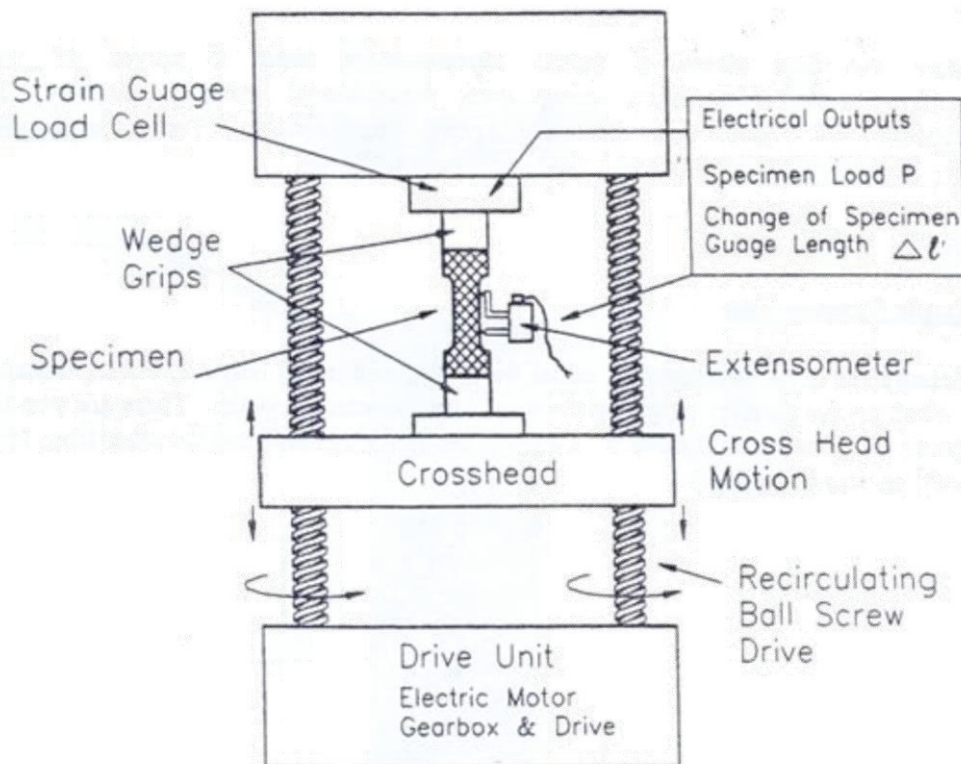
Figure 3.4. Schematic representation of INSTRON tension test machine.

(Source: Tan 2021[79])

The samples were produced as a single plate of 5 plies in an oil-heated compression mold at 120°C, then post-cured at 90°C for 12 hours. The concluded material is a 400 mm-by-400 mm sheet with a 3mm thickness. The samples were then cut by a water jet and prepared. Prepared samples for these tests can be seen on Figure 3.7, at the composite coupons section, tensile, compression, and ILSS samples were tested, and the gathered data was used to develop a FEM material model. Tensile tests were conducted in the transverse direction to determine multiple-direction characters.

3.1.1. Manufacturing of the Test Coupons

Coupon experiments were conducted to assess the strength properties of epoxy composites reinforced with glass fibers. The test specimens were created through a compression molding technique at 120°C following the same production recipe as the full-sized beams. This approach mirrors the process used in making serially produced leaf springs, which ensure pressure distribution across the material.

Subsequently, the batches of samples underwent post-curing at 90°C for 12 hours to improve their material characteristics. Each composite plate manufactured had dimensions of 400 mm length, 400 mm width, and 3 mm thickness.

Using a waterjet cutting machine, the samples were then accurately trimmed to the required dimensions. This method was selected to meet the needs for producing test coupon samples, guaranteeing precision and minimal thermal damage to the material.

The fabrication of the plates and subsequent cutting of coupon samples are depicted in Figure 3.6. This illustration guides each step involved in creating the test specimens, from molding to the final cutting phase. This thorough preparation procedure guarantees that the test samples meet standards of quality and consistency as a factor in acquiring dependable and repeatable mechanical property data during the following coupon tests.

3.1.2. Material Characterizations

A series of standardized mechanical tests were conducted to accurately determine the material properties and establish foundational data for future enhancements. Specifically, the ASTM D3039[76] Tensile Test, ASTM D6641[81] Compression Test, ASTM

2344[82] Short Beam Strength (Inter Laminar Shear Strength), and ASTM D790[77]

Three Point Bending Tests were executed to evaluate the material's behaviors and basic mechanical characteristics. These tests gauge tensile strength, compressive strength, and flexural properties, offering insights into how the material performs under loading conditions.

The findings from these tests played a role in developing material property charts that function as benchmarks for Computer Aided Engineering (CAE) models. Utilizing these test outcomes allowed it to simulate and analyze the material's mechanical properties, ensuring dependable and reproducible data for subsequent assessments and enhancements.[76,77,81] These tests helped to model a materials cart. The materials carts were used as a baseline for the computer-aided engineering analysis (CAE) models.

3.1.2.1. Tensile Test Method

Tensile tests are done according to ASTM D3039 [76] testing standard. Two Shimadzu Universal Testing Machines with 100kN and 300kN loadcells are used, respectively. Test rate of 2mm per minute according to standard applied. A video extensometer was used to measure the strain in tensile tests.
The 300kN Shimadzu Universal Testing Machine's loadcell with a tensile coupon sample can be seen on the Figure 3.5. On the coupon sample, the video extensometer's gauge mark stickers are shown in Figure 3.5.

3.1.2.2. Compression Test Method

The compression test was done on the same machine with different apparatuses. The apparatus is designed and manufactured according to the standard. The test was done according to ASTM D6641[81] with 1.3mm per minute according to the standard.

On the compression test, the strain is measured via strain gauges. The strain data is collected with the Dewesoft Data Acquisition device at 100Hz. The test bench can be seen in Figure 3.6; the apparatus is designed and made according to ASTM D6641[81] standard.

3.1.2.3. Three-Point Bending Tests Methods

The 3-point bending test was done on a Shimadzu Universal Testing machine with a 100kN load cell. The test is done with a 3-point bending fixture. The test was done according to ASTM D790[77] with 1.26 mm per minute. A typical test bench for 3-point bending can be seen on Figure 3.8[83]. Two pillars support the coupon, and another is pressed to bend the part. The test speed is adjusted according to the testing standards.
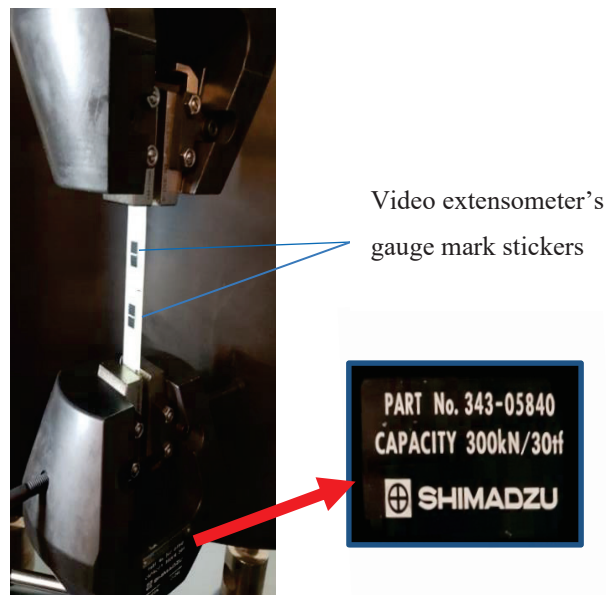
Figure 3.5. Shimadzu Universal Testing Machine with a Tensile Coupon Test.
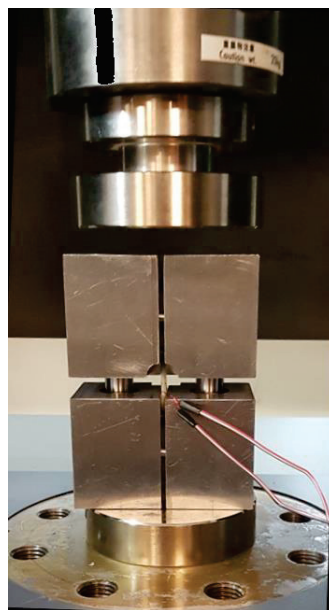
Figure 3.6. Compression Coupon Test.

Stacking of the Plies

Composite Plate

Prepreg plies cutting
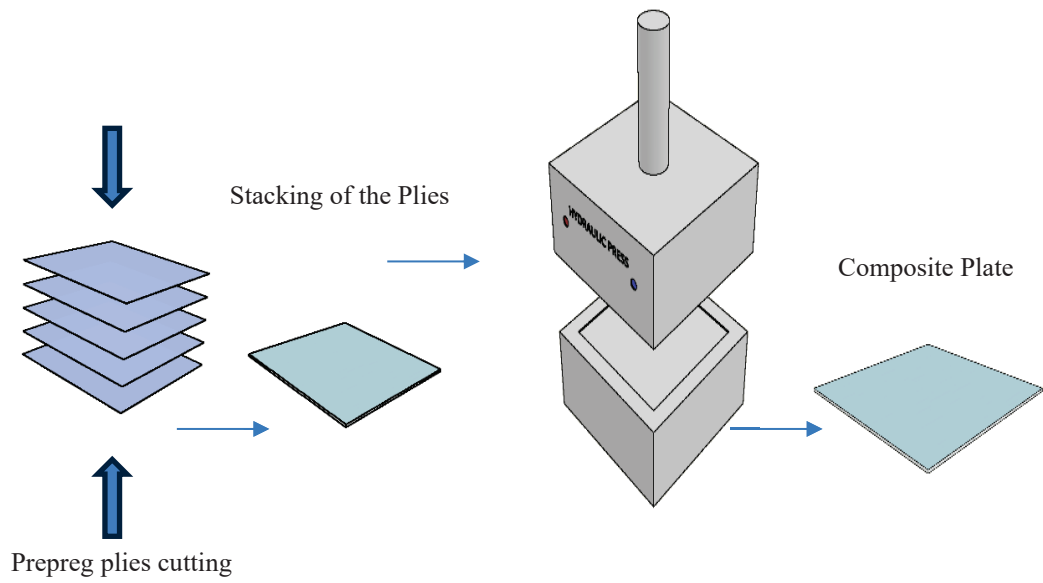
Plies Compress Molded and
Cured in a Press Mold.

Sectioning of the Plate via Waterjet.
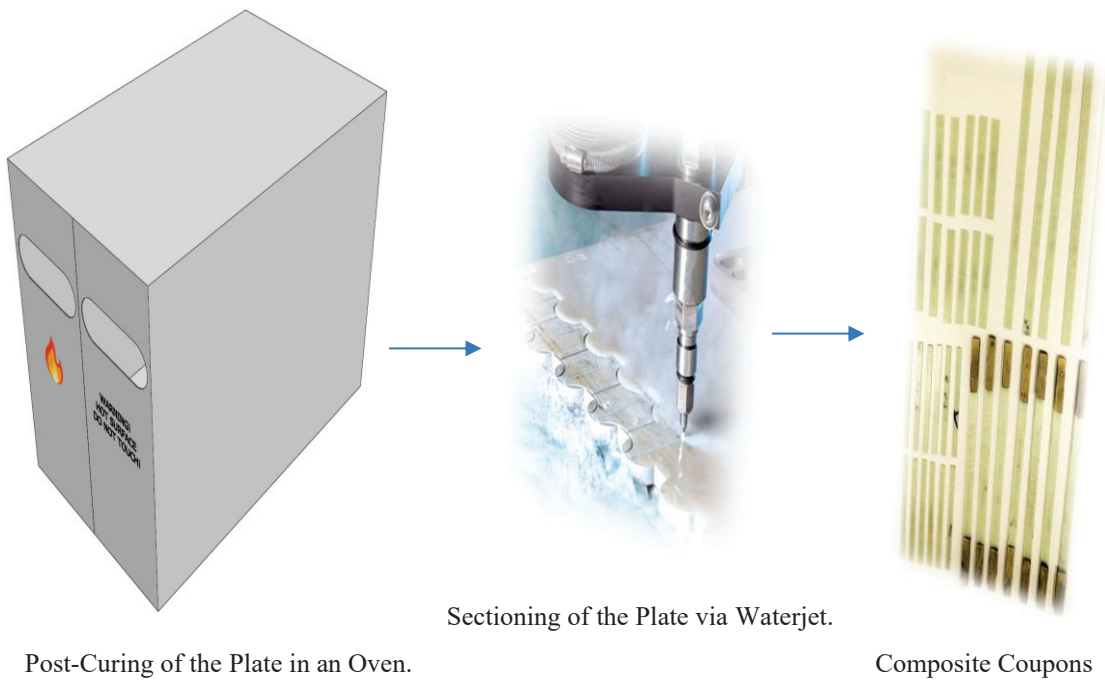
Post-Curing of the Plate in an Oven.

Composite Coupons

Figure 3.7. Illustration of the composite plate fabrication with coupon preparation.

Figure 3.8. Instron 3 Point Bending Test Fixture. (Source: Instron 2021[83])

3.1.2.4. Interlaminar Shear Strength (ILSS) Test

ILSS test is done to determine the interlaminar shear strength of the composite materials. The test is similar to a 3-point bending test, yet the test is conducted without any bending. To induce pure shear without bending, the ASTM D 2344[82] standard is used with a unique geometry, as shown in Figure 3.9[82]. The ILSS is calculated via the Equation (3.4)[82]. An actual testing picture can be seen in Figure 3.10.

3.1.3. Coupon Test Results

Tests are inspected according to their respective standards; each type of test gives us a specific engineering value. Some test samples failed, so they were omitted from the results.

$$ILSS = \frac{3P_{max}}{4B\delta} \ [\frac{J}{m^2}] \tag{3.4}$$
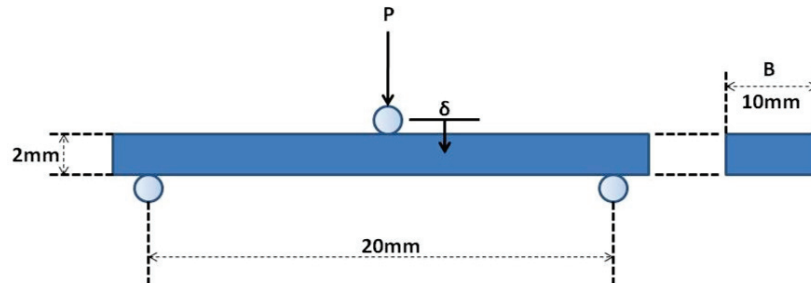
Figure 3.9. ILSS Test Geometry.(Source: ASTM D 2344)

Figure 3.10. ILSS Testing Bench.

3.1.3.1. Tensile Tests of Axial Coupons and Results

The Tensile test samples of Axial coupons are produced in an oil-heated mold. The Axial test sample dimensions can be seen on

Table 3.2, and the actual picture of these tests can be seen on Figure 3.11. The coupons are cut from a 5-ply plate in waterjet sanded at the end tap areas and bonded with a two-part structural epoxy adhesive, DP420[84], and waited for at least 24 hours to cure per the adhesive's Technical Data Sheet (TDS)[84] guides.

Figure 3.11. Axial Test Coupons Before the Test.

The coupons are cut from a 5-ply plate in waterjet sanded at the end tap areas and bonded with a two-part structural epoxy adhesive, DP420[84], and waited for at least 24 hours to cure per TDS[84] guides. As shown in Table 3.3 the sample failure modes are coded with special name tags. The definitions are also used in the results table as the standard guides. The axial tensile test samples before and after can be seen in Figure 3.12 and Figure 3.12, respectively. The coupon dimensions are shown in

Table 3.2. The dimensions are within the ASTM D3039[76] dimension tolerance. After the test, the results are compared to the standard failure modes, as shown in Table 3.3[76].

3.1.3.2. Tensile Tests of Transverse Coupons and Results

The Tensile Transverse coupon tests were produced in a heated mold. The Transverse test sample dimensions can be seen on Table 3.6, and the actual picture of these tests can be seen on Figure 3.13. The coupons are cut from a 5-ply plate in a waterjet.

Table 3.2. Axial Tensile Test.

Tensile Test Axial			
Sample Name	Width (mm)	Thickness (mm)	Gauge Length (mm)
K0_TA _ 1	25.5	3.05	49.81
K0_TA _ 2	25.13	2.89	52.04
K0_TA _ 3	24.73	2.79	50.39
K0_TA _ 4	25.73	2.71	51.47
K0_TA _ 5	26.73	3.01	50.27
K0_TA _ 6	27.73	2.92	50.32
K0_TA _ 7	28.73	2.71	47.98

Table 3.3. Tensile Test Failure Codes/Typical Modes.(Source: ASTM D3039[76])

First Character		Second Character		Third Character	
Failure Type	Code	Failure Area	Code	Failure Location	Code
Angled	A	Inside Grip/Tab	I	Bottom	B
Edge Delamination	D	At Grip/Tab	A	Top	T
Grip/Tab	G	<1W from Grip/Tab	W	Left	L
Lateral	L	Gage	G	Right	R
Multi-Mode	M(xyz)	Multiple Areas	M	Middle	M
Long. Splitting	S	Various	V	Various	V
Explosive	X	Unknown	U	Unknown	U
Other	O				

The axial Tensile test samples before and after can be seen Figure 3.13 and Figure 3.14 respectively. The coupon dimensions are shown in Table 3.6. The dimensions are within the ASTM D3039[76] dimension tolerance.

Table 3.4. Tensile Axial Test Failure Modes.

Sample Name	Failure Type	Test Acceptance
K0_TA _ 1	SAV	OK
K0_TA _ 2	GAB	NOK
K0_TA _ 3	SGM	OK
K0_TA _ 4	XMV	OK
K0_TA _ 5	XMV	OK
K0_TA _ 6	SGM	OK
K0_TA _ 7	LIT	NOK
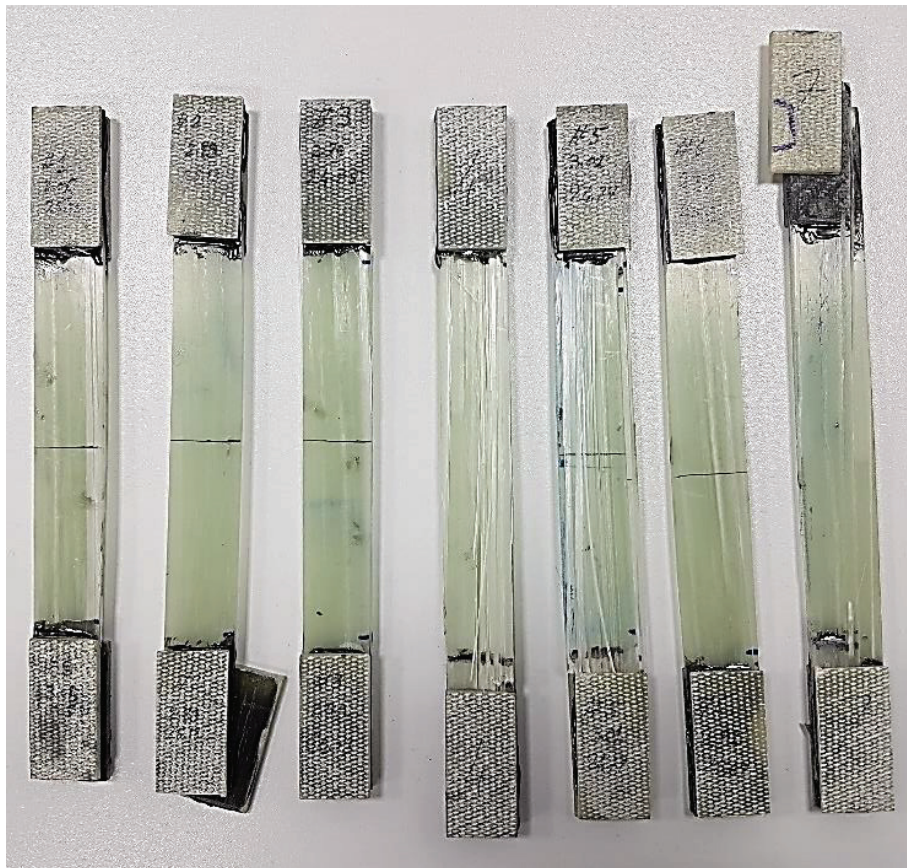
Figure 3.12. Tensile Axial Test Coupons After the Test.

Table 3.5. Tensile Axial Test Material Data.

STM D3039 2 mm/min			
Sample Name	Tensile Strength (MPa)	Strain at Break	Ex Young's Modulus [MPa]
K0_TA _ 1	987.7	0.20	58756.32
K0_TA _ 2	N/A	N/A	N/A
K0_TA _ 3	1101.1	0.20	64109.32
K0_TA _ 4	957.5	0.17	48045.78
K0_TA _ 5	737.2	0.15	51126.44
K0_TA _ 6	660.4	0.15	65910.13
K0_TA _ 7	N/A	N/A	N/A
Avg. (Ort.)	888.786	0.17	57589.60
St. Dev. (±)	183.536	0.02	7841.49

Table 3.6. Tensile Transverse Test Coupon Dimension.

Sample Name	Width (mm)	Thickness (mm)
K0_TÇ _ 1	2.8	14.96
K0_TÇ _ 2	2.64	15.15
K0_TÇ _ 3	2.69	14.99
K0_TÇ _ 4	2.76	14.97
K0_TÇ _ 5	2.87	15.22

3.1.4. Compression Tests of Transverse Coupons and Results

The compression test samples of Transverse coupons are produced in an oil-heated mold. The transverse test sample dimensions can be seen on Table 3.8, and the actual picture of these tests can be seen on Figure 3.16 The dimensions are within the limits of ASTM D6641[81] dimension tolerance.

The calculated test result data can be seen on Table 3.12. The strain measurement is done via two strain gauges on each side of the samples. The measured strains should be in the compression direction on both gauges, or the test would fail according to the ASTM D6641[81] standard.
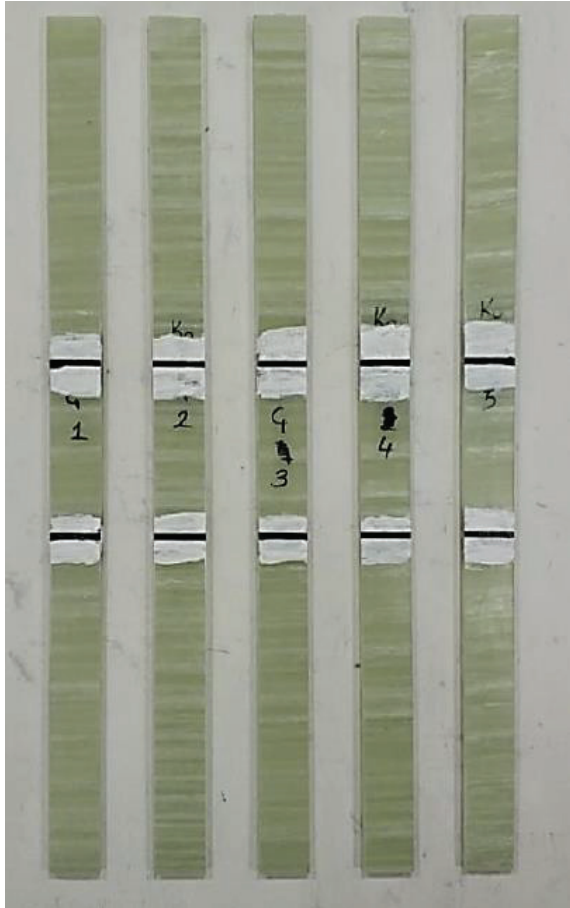
Figure 3.13. Tensile Transverse Coupon Samples.

Figure 3.14. Tensile Transverse Test Coupons After the Test.

Table 3.7. Tensile Transverse Test Results.

ASTM D3039 2 mm/min		
Sample Name	Transverse Tensile Strength (MPa)	Strain at Break
K0_TÇ _ 1	34.81	0.33
K0_TÇ _ 2	31.66	0.2
K0_TÇ _ 3	36.66	0.32
K0_TÇ _ 4	33.38	0.27
K0_TÇ _ 5	33.88	0.34
Avg. (Ort.)	34.08	0.29
St. Dev. (±)	1.84	0.06

The dissimilar strain value depicts a bend instead of a compression. Thus, if pure compression fails, so does the test. All of the five samples pass this criterion, so they are calculated. The samples after the test can be seen on Figure 3.17. The failure position of the samples can be seen in the image.

3.1.4.1. Three-Point Bending Test of Axial Coupons

The Axial 3-point bending test samples are produced in an oil-heated mold. The test samples are shaped according to ASTM D790[77] and the actual picture of the test can be seen on Figure 3.18. The samples before the test can be seen on Figure 3.19. The coupon dimensions can be seen on Table 3.9. Sample numbers match in the table as the coupon sample photograph shows.

The test results can be seen in Table 3.10. Tripoint Bending Test Results Table 3.10. The strength strain deviation is within acceptance tolerances of the standard, as seen in the table. The coupons after the test can be seen on Figure 3.20. The results show the failure in the middle of the samples. Thus, the tests are valid according to the standard [77].

3.1.4.2. Three-Point Bending Test of Transverse Coupons and Results

The Transverse 3-point bending test samples are produced in an oil-heated mold. The test samples are shaped according to ASTM D790[77]. The samples before the test can be seen on. Figure 3.21. The coupon dimensions can be seen in Table 3.11.

The coupon sample names are the same as the definitions written on the sample pictures, as applied to the previous coupons. The test results can be seen on Table 3.12. The strength strain deviation is within acceptance tolerances of the standard, as seen in the table. The coupons after the test can be seen on Figure 3.22. The results show the failure in the middle of the samples. Thus, the tests are valid according to the standard.[77]
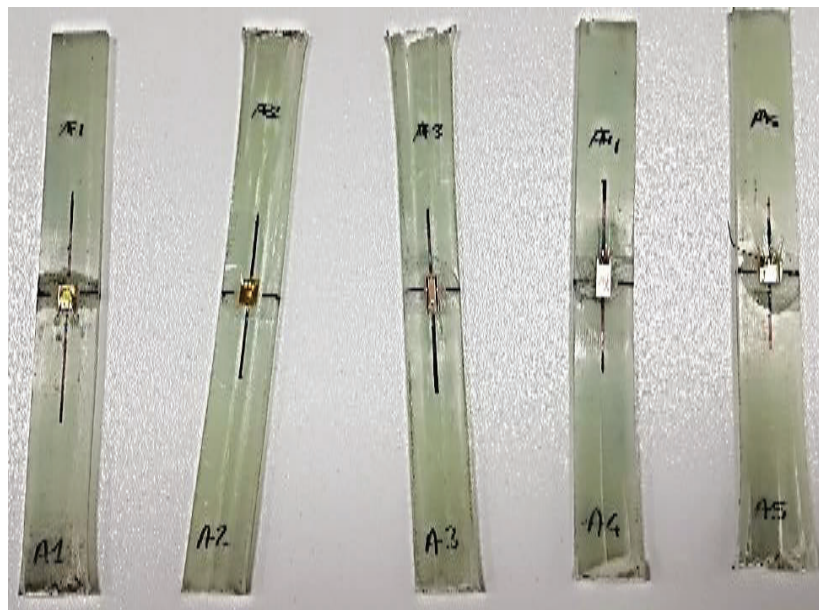
Figure 3.15. Axial Compression Test Coupons After the Test.
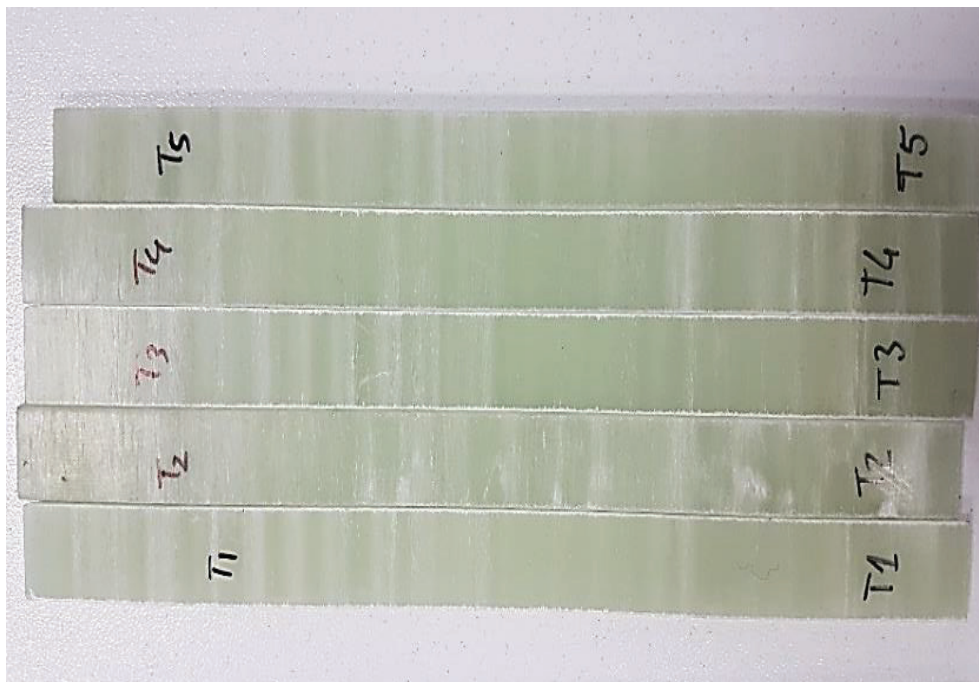
Figure 3.16. Transverse Compression Pre-test Coupon Samples.

Table 3.8. Compression Transverse Test Coupon Dimension.

Compression Test Transverse		
Sample Name	Thickness (mm)	Width (mm)
Comp T1	2.75	11.97
Comp T2	2.76	12.08
Comp T3	2.78	11.99
Comp T4	2.76	12.02
Comp T5	2.77	11.95
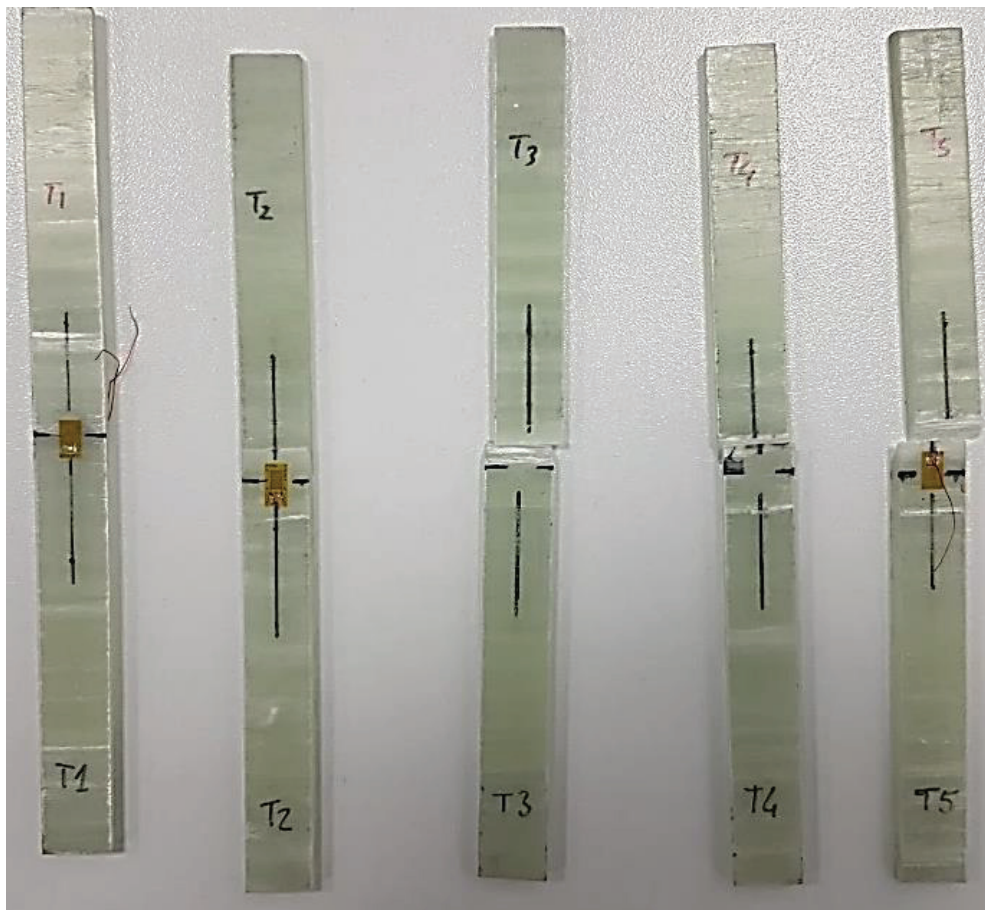
Figure 3.17. Compression Transverse Coupons After the Test.

Table 3.9. Axial Three-Point Bending Coupon Dimensions.

Sample Name	Thickness (mm)	Width (mm)
K0_A_3PB _ 1	2.63	14.89
K0_A_3PB _ 2	2.61	14.90
K0_A_3PB _ 3	2.66	14.87
K0_A_3PB _ 4	2.62	14.90
K0_A_3PB _ 5	2.83	14.93
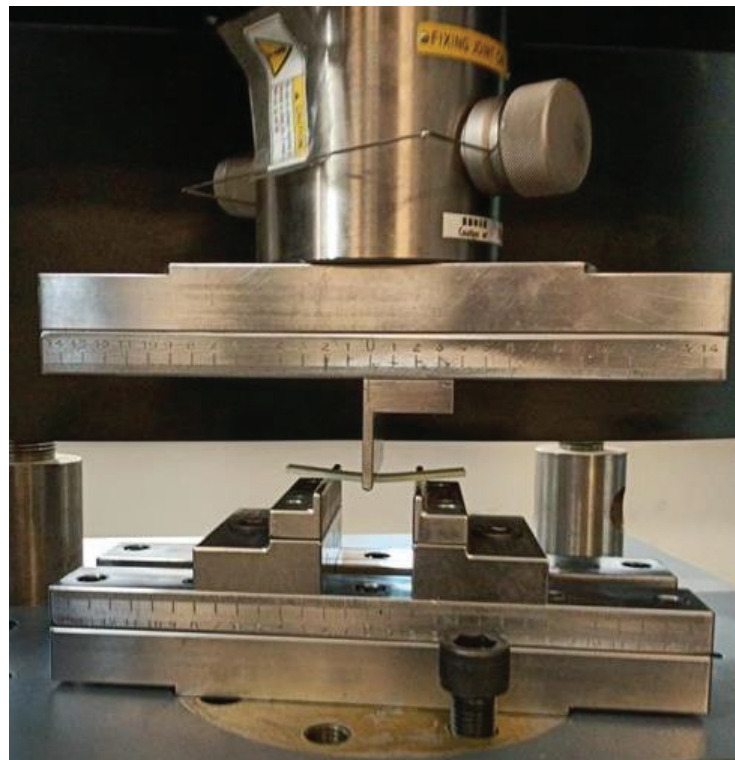
Figure 3.18. Axial Coupons of Tripoint Bending.

3.1.5. Inter Laminar Shear Strength Test of Coupons and Results

The ILSS test samples are produced in an oil-heated mold. The test samples are shaped according to ASTM D2344[82] standard, and the actual picture of the test can be seen on Figure 3.23. The test results are shown in Table 3.13. The results show acceptable deviation according to the standard. ILSS test samples are produced in a small enough dimension to prevent flexural behavior, thus only allowing interlaminar shear behavior to be affected.
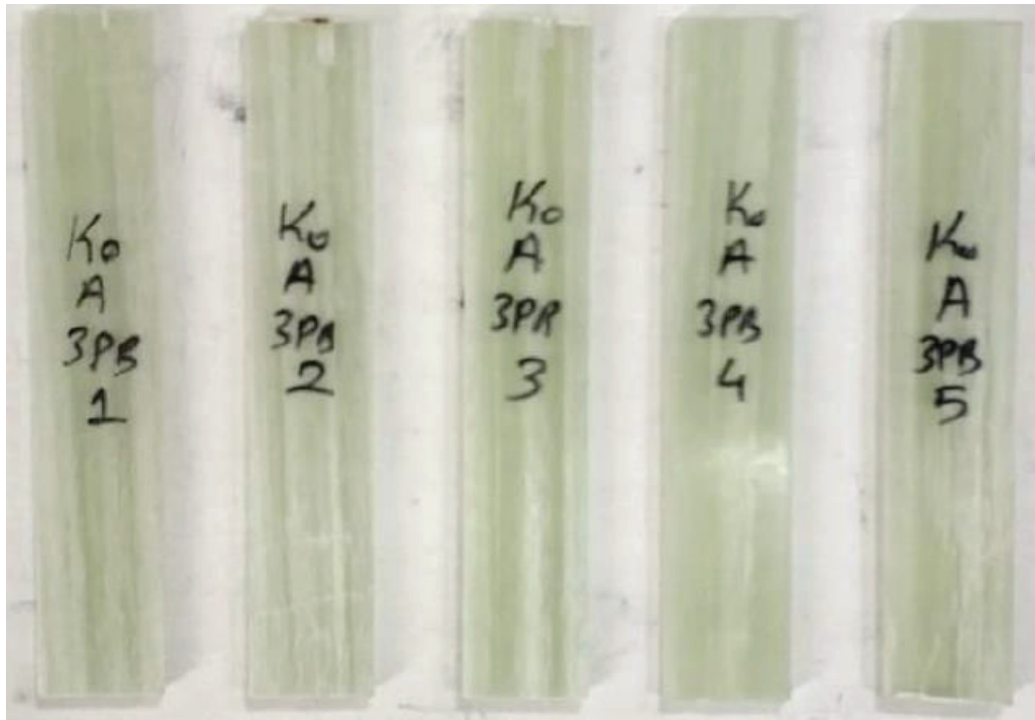
Figure 3.19. Tripoint Bending Test of Coupon Tests.

Table 3.10. Tripoint Bending Test Results.

Axial 3Point Bending Test Results			
Sample Name	Max Force (N)	Bending Strength (MPa)	Max Stroke (mm)
K0_A_3PB _ 1	2032.81	1361.88	4.41
K0_A_3PB _ 2	1937.34	1317.01	4.18
K0_A_3PB _ 3	1981.88	1299.73	4.07
K0_A_3PB _ 4	2174.84	1467.19	4.75
K0_A_3PB _ 5	2091.09	1206.67	3.88
Average	2043.59	1330.50	4.26
Std. Dev. (±)	93.13	95.04	0.33

Figure 3.20. Axial Three-Point Bending Coupons After the Test.

Table 3.11. Transverse Three-Point Bending Coupon Dimensions.

Three-Point Bending Transverse Coupons		
Sample Name	Thickness (mm)	Width (mm)
K0_T_3PB _ 1	2.7	14.95
K0_T_3PB _ 2	2.67	14.94
K0_T_3PB _ 3	2.61	14.96
K0_T_3PB _ 4	2.62	15
K0_T_3PB _ 5	2.69	15
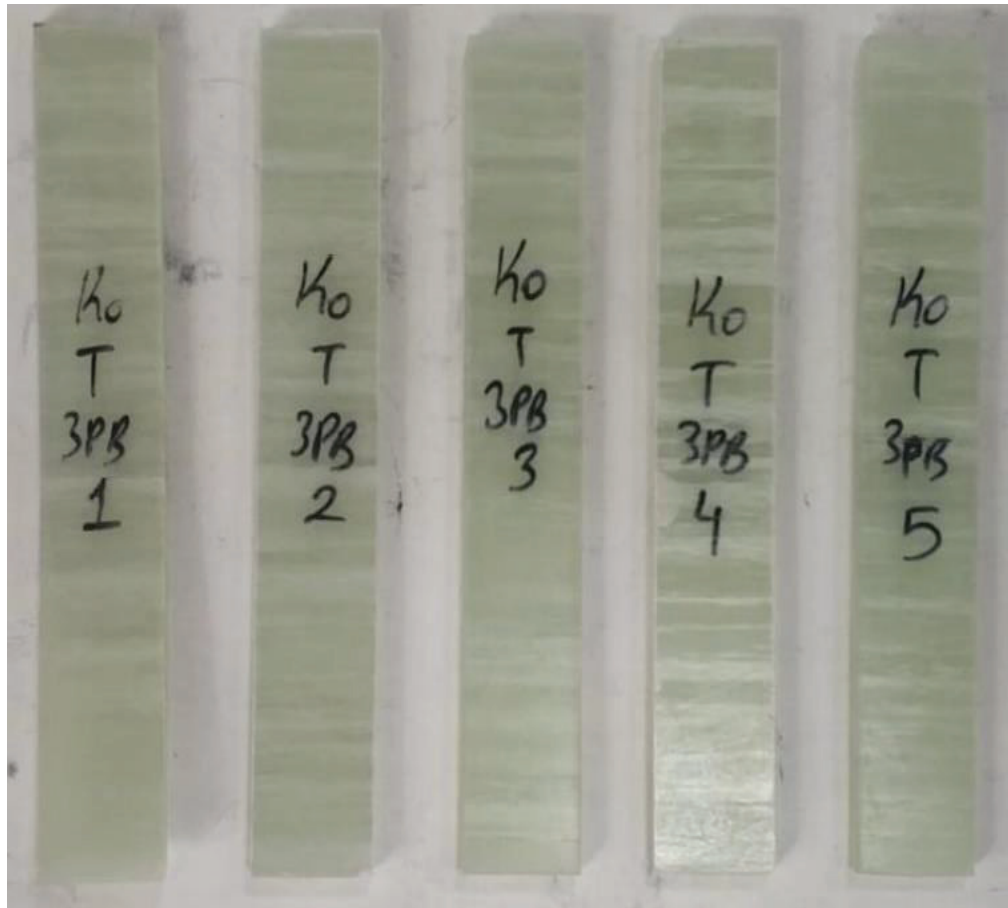
Figure 3.21. Transverse Tripoint Bending. Coupons

Table 3.12. Results of Transverse Three Point Bending.

Transverse Three-Point Bending Results			
Sample Name	Max Force (N)	Bending Strength (MPa)	Max Stroke (mm)
K0_T_3PB _ 1	92.5	58.56	0.67
K0_T_3PB _ 2	104.25	67.54	0.73
K0_T_3PB _ 3	83.44	56.5	0.65
K0_T_3PB _ 4	116.38	77.99	0.9
K0_T_3PB _ 5	100.94	64.17	0.74
Average	99.5	64.95	0.74
Std. Dev. (±)	12.41	8.51	0.1

Figure 3.22. Examine the Transverse Three Point Bending Coupons Following the Test.

Figure 3.23. ILSS Testing of Coupon Test.

Table 3.13. ILSS Coupon Test Results.

Sample Name	ILSS
1	70.39
2	80.76
3	75.64
4	74.49
5	73.09
6	65.28
7	70.58
Average	72.89
Std. Dev.	4.50

3.2. Simulation Correlation of Tensile Test

The test results were used to determine Computer Aided Engineering (CAE) model simulation parameters. Altair® program group was used for the simulations.[85–89] The primary characterization is done in Radioss® to simulate the tensile behavior of the material linear data. Data gathered through the tests has been applied as Sigma Yield and Young's Modulus to the CAE model.
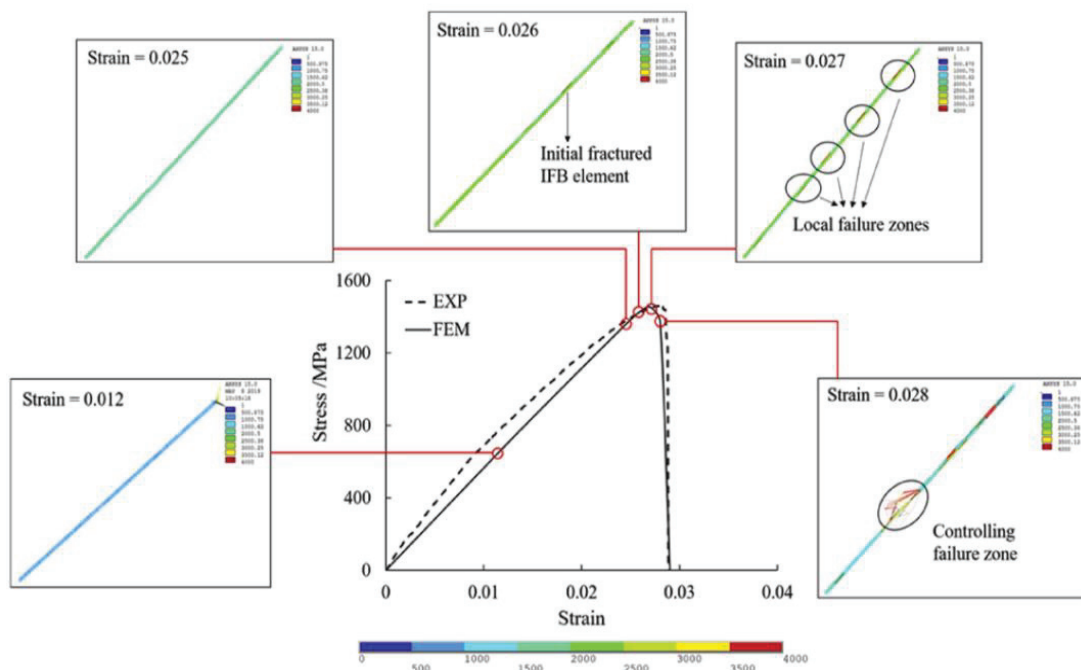
Figure 3.24. Tensile Sample Stress-Strain Comparison Between Test and FEM Analysis.

(Source: Peng 2020)

The test for Compression[79] and ILSS[82] was also conducted to determine the materials' characteristics fully. The gathered information was used in Finite Element Analysis models (FEM). The material models were used as a base for computer analysis. A typical comparison graph can be seen on Figure 3.24[20]. As can be seen from the graph, the curves of the Experimental and FEM models do not fit perfectly, yet they resemble each other.

The material model is selected as Mat25 with PCOMPP property. 24QEHP Composite Shell formulation is used to reduce computation time with acceptable results[86]. This part of the analysis is done only for continuous fiber composites, and further analysis was done for discontinuous samples. The applied data can be seen on Figure 3.26. A transverse coupon sample can be seen on Figure 3.25.

To compare the results, the test data is reduced to 20 points via manual resampling.[90] The data should be selected manually to follow the original test data. The original data and the simplified data example can be seen on Figure 3.27. The simplified data used on this graph is shown in Table 3.14. Simplified Test data is used to correlate the nonlinear characteristics of the simulation.

Tensile Axial test results can be seen on Figure 3.28. The CAE of the coupon sample failed at the center, which is similar to the test results. Figure 3.29 from left to right, the CAE model's unloaded, loaded, failed, and failed states can be seen. The test result has some fluctuation. This is a normal behavior since the fiber failure happens in a duration rather than instantly at all fire bundles. CAE demonstration shows a similar failure mode as the test, where the tension spreads through the length, and the failure starts from the central line.
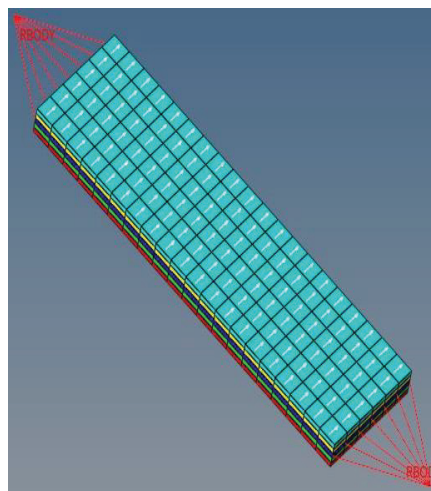
Figure 3.25. Transverse Coupon Basic CAE Model.

Name	Value
Solver Keyword	/MAT/COMPSH/
ID	1
Name	Kord_UD1
Color	■
Include	[Master Model]
Defined	☑
User Comments	Do Not Export
Card Image	M25_COMPSH
Regular_OR_encrypted_flag	Regular
RefRho_Option	☐
Rho_Initial	1.94e-09
E11	57000.0
E22	10500.0
Nu12	0.2
Iform	0: Standard formulation
E33	9600.0
G12	5200.0
G23	5200.0
G31	4900.0
Epsilon_f1	
Epsilon_f2	
EPS_t1	0.022
EPS_m1	0.2205
EPS_t2	0.0038
EPS_m2	0.003805
d_max	
Wp_max	
Wp_ref	
Ioff	6: If for each layer, Wp > Wpmax or tensile failure in direction 1 or 2

Figure 3.26. CAE Model Simulation Data.

Table 3.14. Simplified Data Example of Coupon Test's Analysis.

% Strain	Stress [MPa]
0.000%	0.10
0.145%	88.48
0.284%	140.42
0.358%	181.30
0.425%	219.84
0.498%	259.82
0.594%	301.06
0.667%	343.71
0.754%	388.32
0.835%	434.28
0.941%	481.61
1.029%	529.74
1.120%	579.23
1.249%	628.97
1.323%	678.83
1.418%	728.47
1.545%	777.83
1.641%	826.82
2.124%	987.74
2.144%	3.82
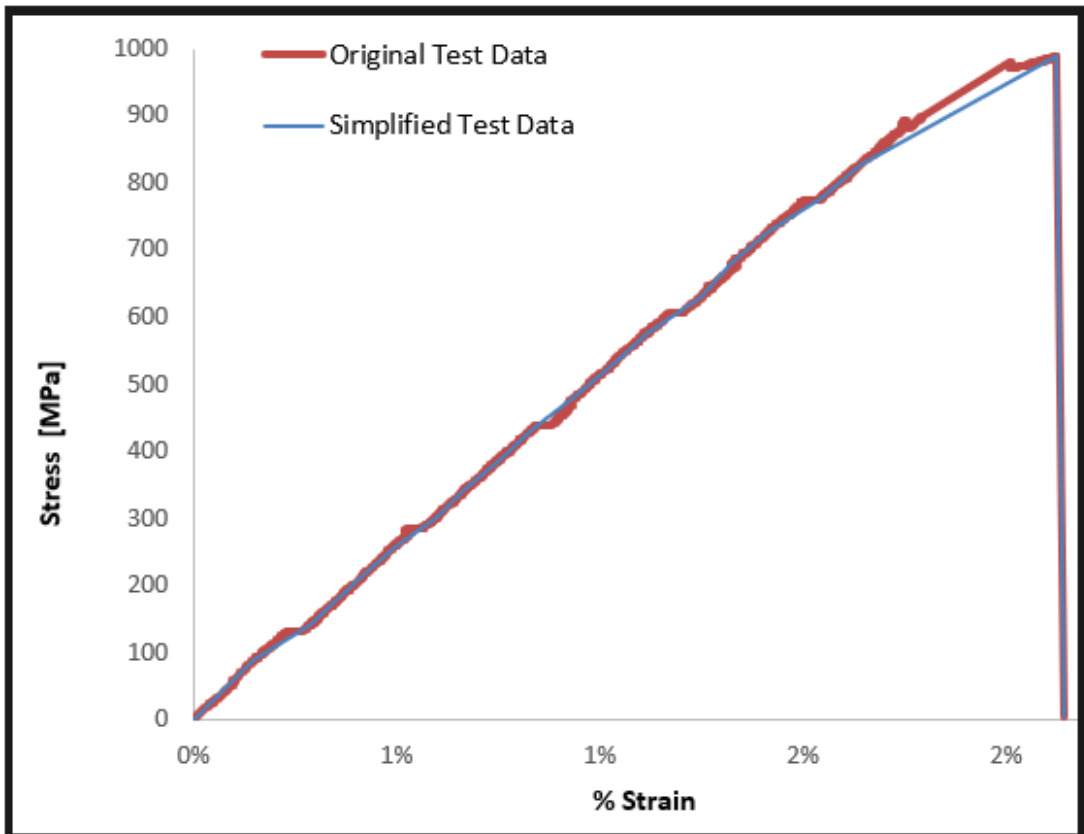
Figure 3.27. Example graph of test data and simplified data comparison.
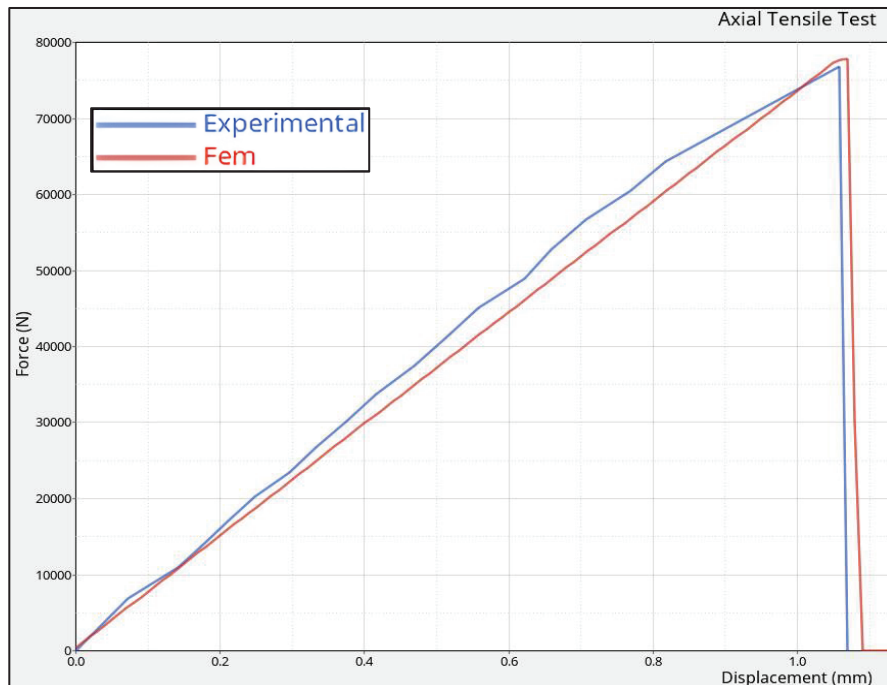
Figure 3.28. Axial Test CAE Comparison Graph.

Figure 3.29. Simulation of the Axial Coupon Test; the Progress is from Left to Right.

3.3. Discontinuous Beam Samples

Although some coupon sample tests can help determine the primary behavior of the material, the smaller and more controlled nature of these experiments narrows the realistic effects of the serial production effects. Tests were conducted to determine the real-life impact of these experiments at full size.

One sample type with fully continuous fiber reinforcement was specified as the reference group. This type of family was named Sample#C. This family is an actual spring that is being serially produced. Sample#C is a reference sample containing all continuous fiber layers. This product is a mass-produced authentic leaf spring. Each sample was created using an identical process in a singular mold. Simultaneously, the fabricated materials were placed on a carrier for post-curing, as seen on Figure 3.31(c). All the samples were produced via the prepreg compression molding and cured in a heated mold under a hydraulic press. The mold temperature was set to 120°C at the center and 100°C at the tips to allow slow curing and remove excess resin from the mold before it gets cured. Beam samples represented parabolic springs.

The parabolic definition means that those springs have variable thicknesses, yet a special non-parabolic serially produced spring is investigated in this study. This selection helped us to utilize the same layer thickness through the length of the spring while we changed the layer width by inducing intra-ply discontinuities. The fiber volume fraction was kept the same along the beam by adding short plies between full-length plies.

The press was set to exert a force of 1000 kilonewtons. Two samples were simultaneously cured in a mold with two cavities. The pressure was gradually raised to

prevent curing at the core while simultaneously adjusting the temperature to prevent rapid surface curing. The samples were subsequently cured in an oven at 90°C for 12 hours. The procedures were conducted in accordance with the leaf spring production process. Olgun Çelik[1]'s subbranch, Olgun Tech facility, determined them through testing and trials at laboratory and field-testing centers.[1]
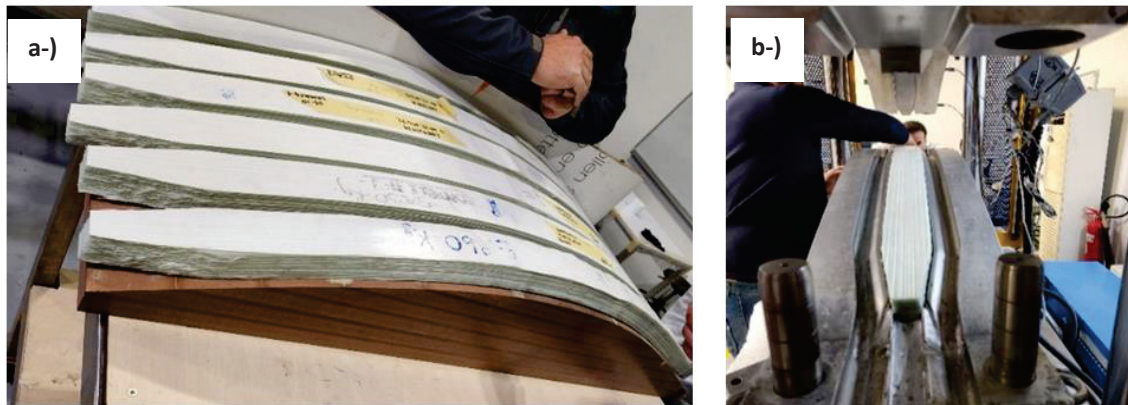
Figure 3.30. Prepreg Forming Before Pressing. a) Prepreg Layup at the preform table, b) Prepreg Layup at in the mold placement step.

An arrangement enables the positioning of the prepreg that was laid up. Consult Figure 3.30 for an illustration of the preform table. The continuous samples labeled #C were created following the process used for fabricating springs. The other two samples were also produced using the same approach except for how they were layered. In these cases, 43 layers of plies were stacked on top of each other. Figure 3.30 displays a sample inside the mold.

The examples illustrate a bird's-eye view of the discontinuous samples. Discontinuities, whether internal or external, are visible on the sides of these samples. The width's discontinuity was increased by 1 mm, resulting in a width of 68 mm at the narrowest point. The post-curing process took place in an electric oven for over six hours. All samples were grouped in a specific tray for post-curing to maintain a consistent temperature.

Three types of interply sample families were produced. Two distinct types of intra-ply fiber discontinuity cases were generated. The continuous sample was used to simulate the ideal case since the sample did not have any discontinuities.[88] The two discontinuous samples depict two of the production limitations. It is important to note that limitations can arise due to geometrical and draping allowances.[69]

Sample#1 was intentionally designed to mimic the variations in thickness found in materials. Modifying the thickness was crucial for ensuring uniform stress distribution in a cantilever arm. There was a lack of research on inter-ply interruptions in full models. Various methodologies, including Sample#2, can be used to investigate this and offer an alternative approach to achieve the desired effect. There could be potential uses for ply interruptions.
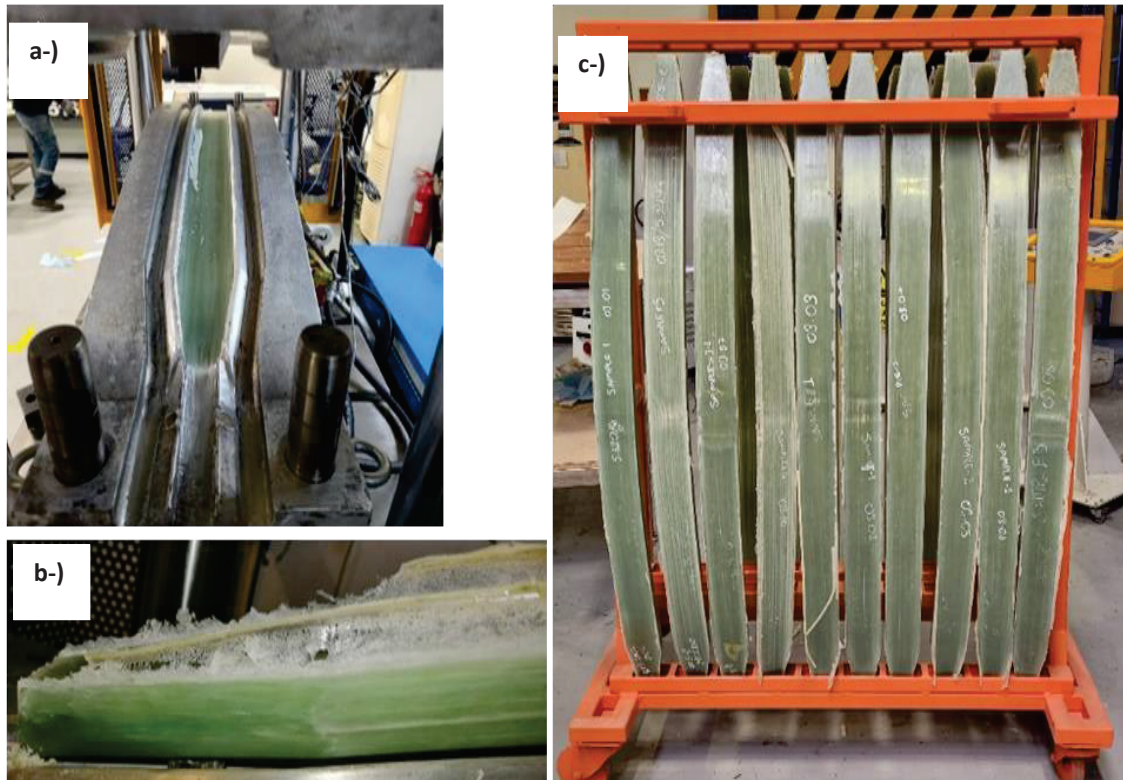
Figure 3.31. Composite Beams After Curing Process. Composite Beams a) in the mold, b) after ejected from the mold, c) at the post-curing tray.

Sample#2 exhibited ply interruptions. Sample#2 differs because it does not contain gaps in the layup phase; interrupted layers are positioned consecutively. The main issue occurs when the layers move during the pressurized curing process because of the resin flow. The shift was evident when examining the pre-curing and microscopic images of Sample#2.

Sample#3 family was designed to mimic the worst-case scenario. The discontinuities were placed in tension-compression direction and to the outermost position. These conditions were designed to compare the status of the best (Sample#C) and the worst (Sample#3).

Sample#4 was one of the two samples consisting of intra-ply discontinuities. Due to the same "ply" on every layer, there was no specific layup book for this type of sample. This sample has the cut-out at the outer sides of the center area. This would cause air gaps and resin-rich regions on the sides of the samples.

The effects of these gaps had been determined during the tests. The design for Sample#4 was specially chosen to resemble the ends of the springs. Narrowing is required at the ends of the spring arms to assemble the spring eye holder. To our knowledge, intra-ply discontinuities on full-size beams have not been studied before. This can be done in multiple ways, as Sample#5 was another method. There may be other uses for the intra-ply discontinuities.

Sample#5 was another type of intra-ply discontinuity sample. Due to the same ply on every layer, there was no specific layup order for Sample #4. This sample is cut out at the inner side of the center area. This made the resin pockets in the middle of the samples. The fibers in the central area spread to fill the central gap, yet there was a resin-rich area in the immediate center.

3.3.1. Definition of Full-Size Beam Samples

Full-sized samples were produced to identify the issues faced during thick part production in serial lines. The samples were designed to mimic 5 problems encountered with thick beam production.

3.3.1.1. Interply Discontinuity Sample #1

In Figure 3.32, side view of Sample #1 can be seen. This subject has 58 layers (plies), yet the highest layers on top of each other are 43 due to discontinuous ply nature. This sample induces triangular-type resin pockets. Each discontinuity length was 40mm, and the total discontinuous area was added up to 120 mm. These resin pockets simulate similar to the Figure 1.2[27] type discontinuity. The white areas at the sides depict the total length of the continuous part.

The 3D Model depicts a more detailed version of the premolding version of Sample#1. The after-layup version can be seen on Figure 3.33. S1D1 is the shortest discontinuous layer of 5, S1D2 is the longest, and S1D3 is the longest.
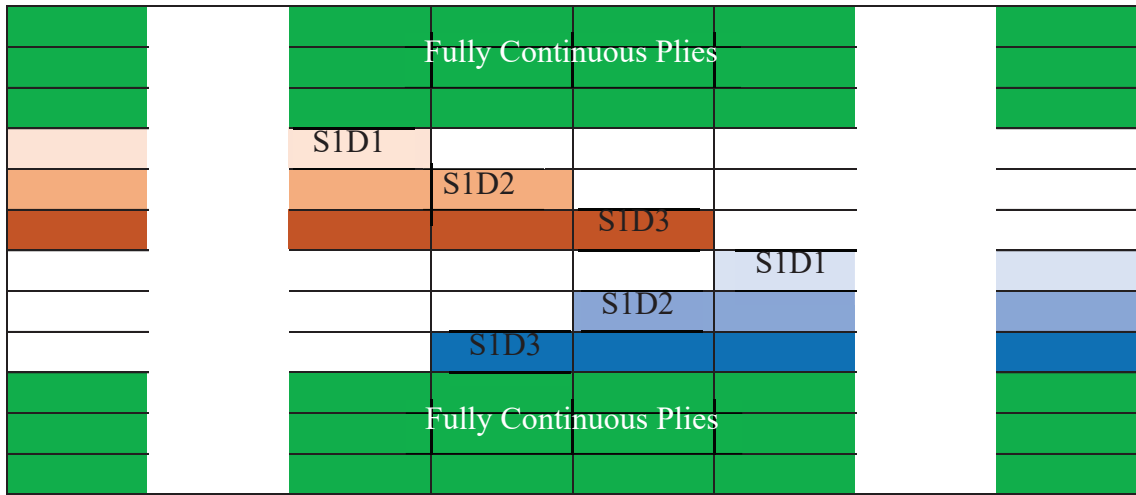
Figure 3.32. Layup Book View of Discontinuous Sample#1.

Each of these layers consists of 5 layers. The vertical lines depict 40mm of length on Figure 3.32. This shows that S1D1 is 40mm shorter than S1D2 and S1D3 80 mm longer than S1D1. The gaps are shown only as a demonstration; the real gaps can be different since the demonstration model is only done as a simple illustration.

3.3.1.2. Interply Discontinuity Sample #2

In Figure 3.34, side view of Sample #2 can be seen. This subject has 58 layers (plies), yet the highest layers on top of each other add up to be 43 due to discontinuous ply nature. This sample induces rectangular-type resin pockets. Each discontinuity length was 40mm and the total discontinuous area adds up to 120 mm. These resin pockets simulate similar to the Figure 1.2[31] type discontinuity.

The white area at the sides depicts the total length of the continuous part. The vertical lines represent 40mm of length on Figure 3.34. This shows that S2D1 was 40mm shorter than S2D2, and S2D3 was 80 mm longer than S2D1. There were 43 plies, yet at the middle of the section, 3 groups of discontinuous lays, each with 5 plies, are placed.

3.3.1.3. Interply Discontinuity Sample #3

In Figure 3.35 side view of Sample #3 can be seen. This subject has 58 layers (plies), yet the highest layers on top of each other add up to be 43 due to discontinuous ply nature. This sample induces triangular-type resin pockets. Each discontinuity length

is 40mm, and the total discontinuous area adds up to 120 mm along the length. The white area at the sides depicts the total length of the continuous part. The total length is planned to be longer than 1000mm. The main difference is that the discontinuities are outside the sample. This showed us the discontinuities' effects on the samples outside areas.

The vertical lines depict 40mm of length on Figure 3.35. This shows that S3D1 was 40mm shorter than S3D2, and S3D3 was 80 mm longer than S3D1. There would be 43 ply layups on each section, yet there would be 58 layers. The discontinuous layers ended in a way that allowed another layer to start.

3.3.1.4. Control Sample of Discontinuous Samples

The interlaminar discontinuity samples were compared with the fully continuous sample of 43 plies. The test subject has equal fiber volume density and plies per section as all the samples. The Figure 3.36 demonstrates Sample #C. The length, production, and test methods were identical in all samples. The image demonstrated is the side view of the continuous sample.

3.3.1.5. Intraply Discontinuity Sample#4

The following samples demonstrate the top view of the discontinuous samples. These samples have intraply discontinuities on their sides, inner or outer parts. Each depicted discontinuity was equal to 1mm, from 74mm at the most expansive area to 68mm at the narrowest area. The fully continuous samples ranged from 55% fiber volume density to about 50.5% fiber volume density.

In Figure 3.37, top view of Sample #4 can be seen. This subject has 43 layers (plies). This sample induces triangular-type resin pockets. Each discontinuity length was 40mm, and the total discontinuous area was added up to 120 mm.

The discontinuity was on the outside of the sample, and all of the plies are the same in this sample. The white area at the sides depicts the total length of the continuous part. Figure 3.38 illustrates the three-dimensional representation of Sample#4. This image was created to facilitate comprehension of the design.

(a)

Resin Pockets

(b)

Fully Continuous Plies

S1D1   S1D2   S1D3   S1D2   S1D1

S1D3

Fully Continuous Plies
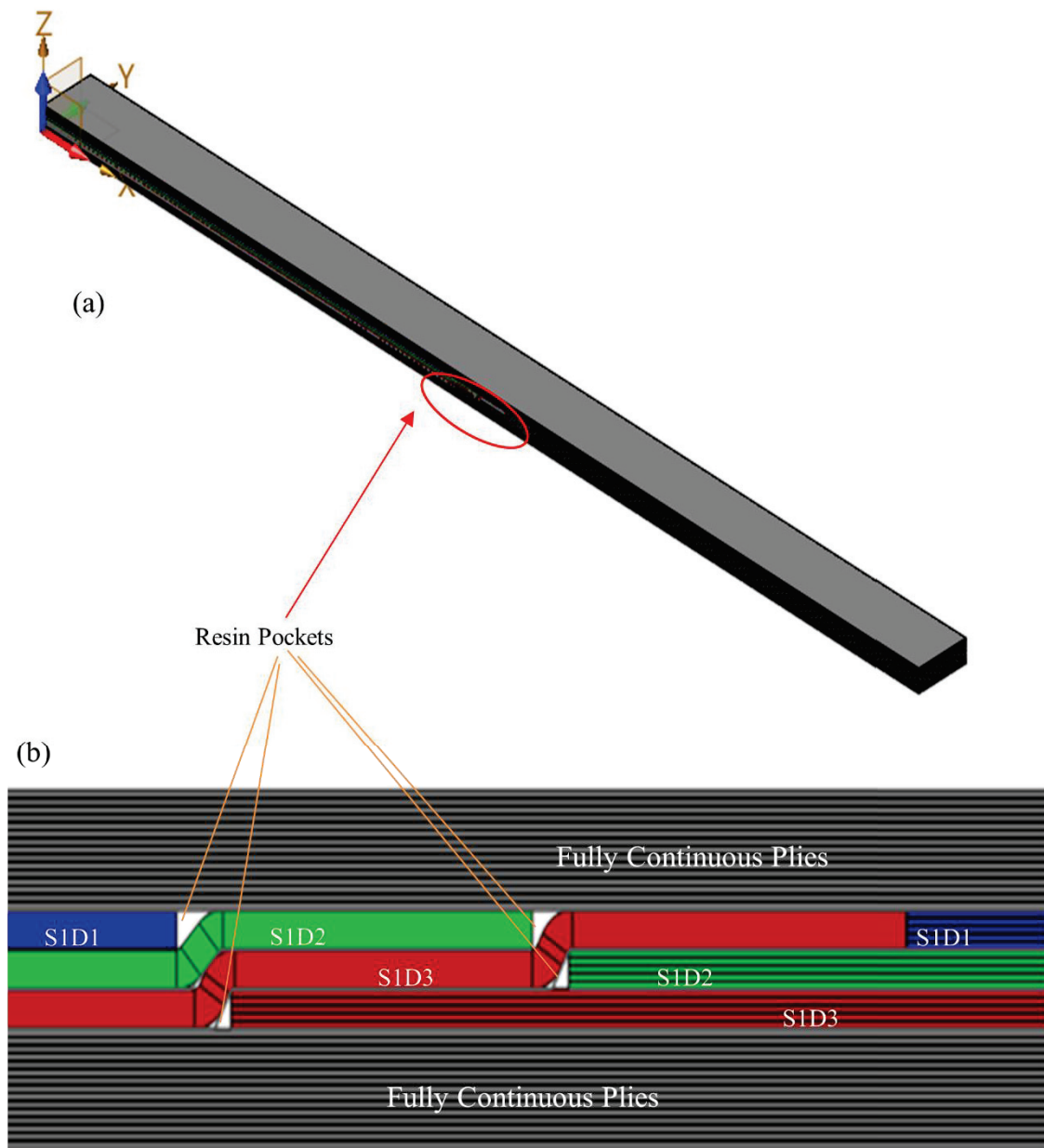
Figure 3.33. Depiction in 3D Model of Discontinuous Sample #1. (a) For the full Section view of Sample #1, the approximate length is 1300mm, the width is 74mm, and the edges were trimmed to 1.2 meters after the curing. (b) The section view of the pre-curing part can be seen from this depiction. The resin pocket zones are shown in white.
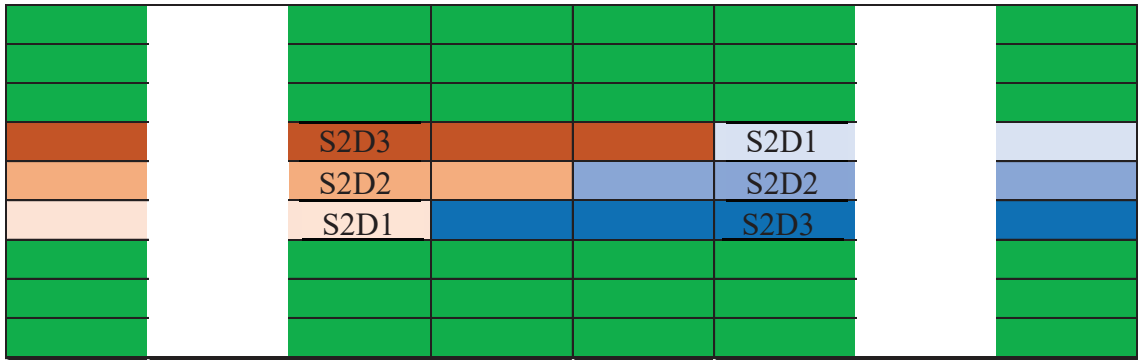
Figure 3.34. Discontinuous Sample #2.

Figure 3.35. Discontinuous Sample #3.
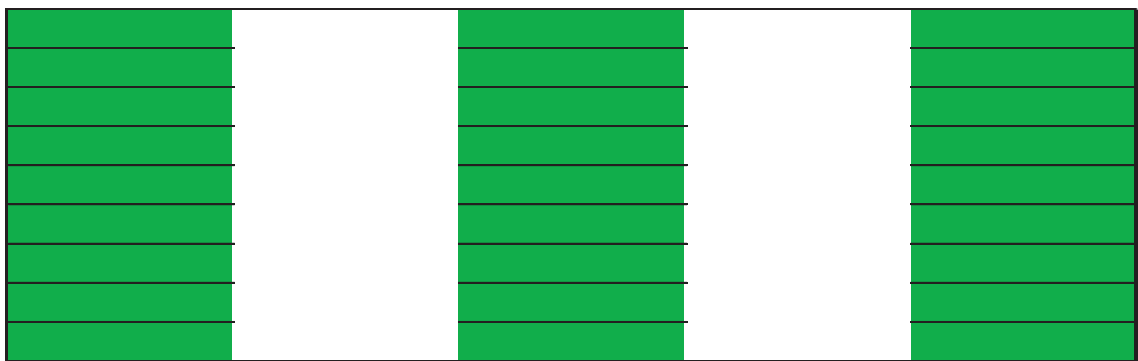
Figure 3.36. Control Sample #C.
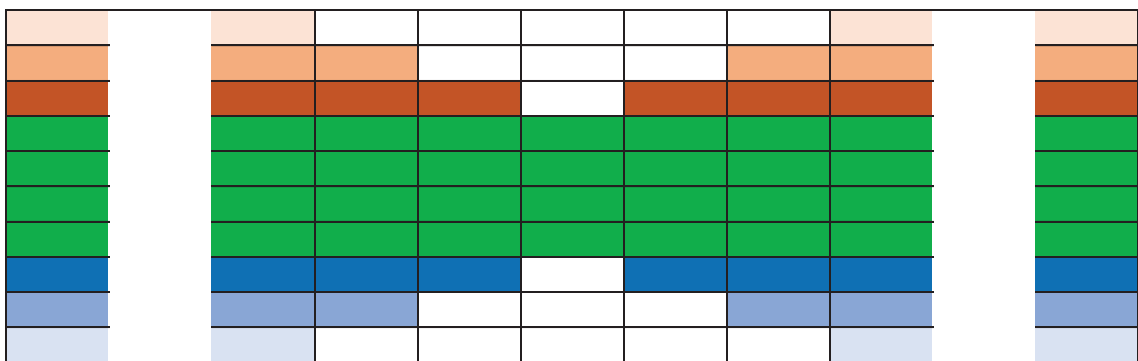
Figure 3.37 Top view of Sample #4.
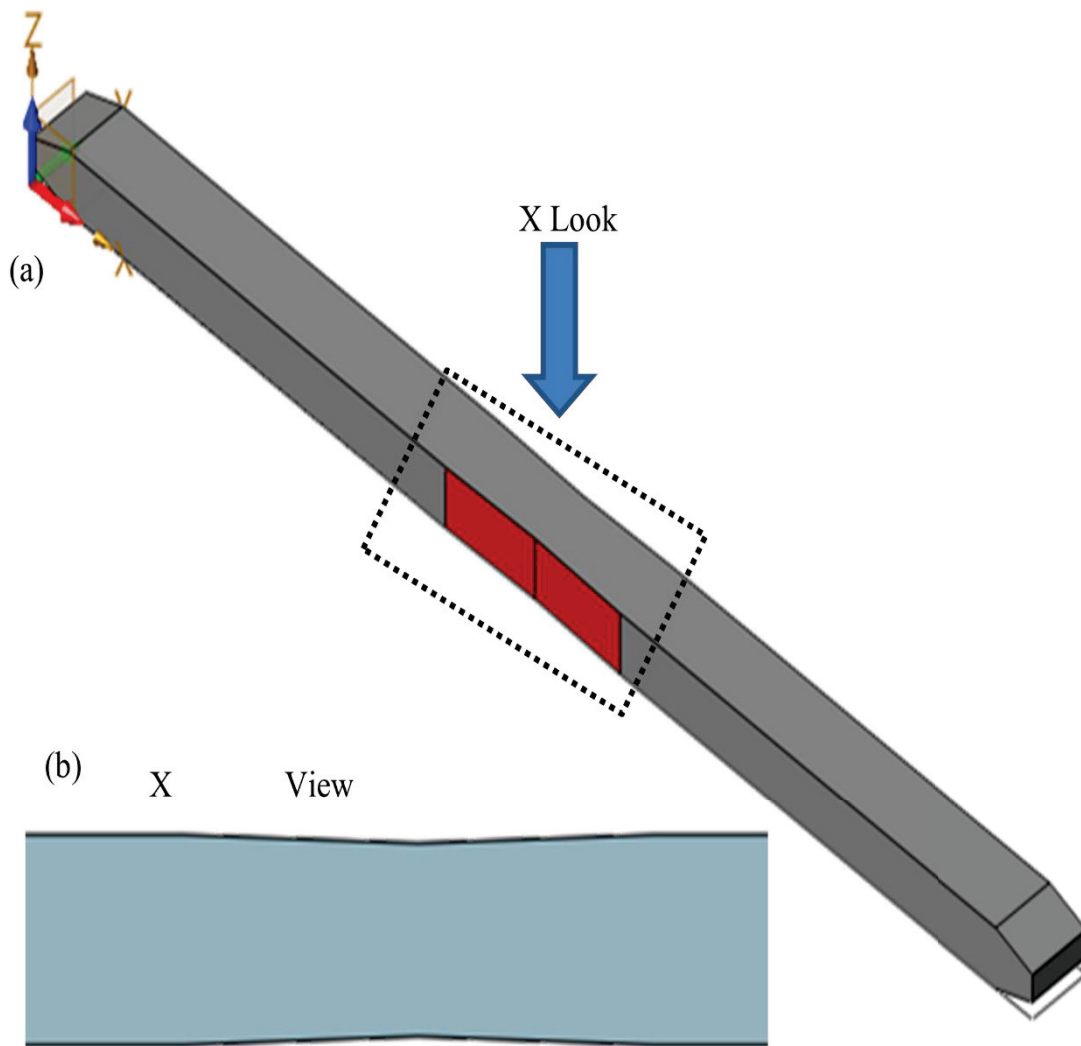
Figure 3.38. 3D Model View of Sample #4. (a) Sample#4 total 3D model (b) The Top view of the model shows the variable width of the sample in the middle section.

3.3.1.6. Intraply Discontinuity Sample#5

In Figure 3.39, top view of Sample #5 can be seen. This subject had 43 layers (plies). This sample induces triangular-type resin pockets. Each discontinuity length was 40mm, and the total discontinuous area was added up to 120 mm. The discontinuity was on the outside of the sample, and all of the plies are the same in this sample. The white area at the sides depicts the total length of the continuous part.

The samples were tested on a 3-point bending fatigue test. All of the samples and the control were compared, and the failure modes and failure cycles were investigated. Applied test stress was adjusted according to the quasistatic coupon test sample data.

The produced sample was tested for static maximum force application on the 3-point bending test fixture in order to determine the quasistatic behavior of the full-size samples. The samples were produced in a serial production leaf spring mold and the curing recipe was the same as the serial production leaf springs. Also, the samples were post-cured, the same as the serial productions.
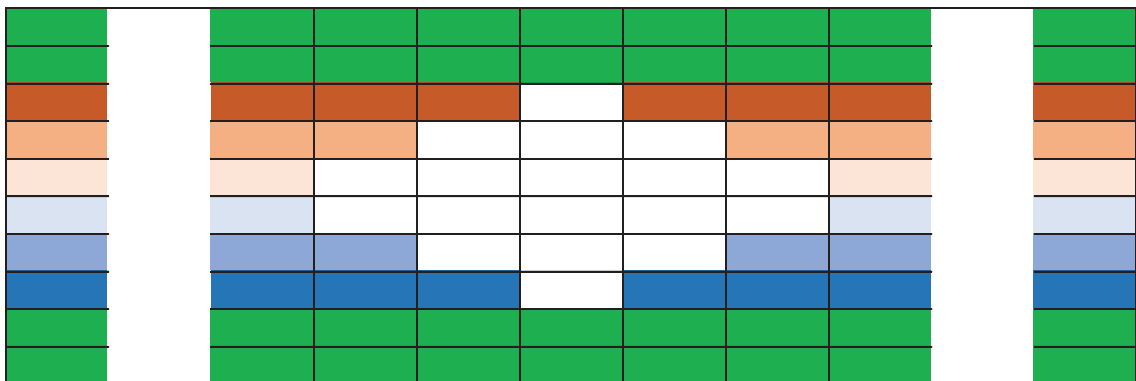
Figure 3.39. Top View of Sample #5.

3.3.2. Production of the Full-Size Samples

There are 6 sample families, as mentioned in the previous chapters; one of them is the continuous sample as the reference sample. The other five depict different types of discontinuities. The continuous sample was used to determine the best results since the sample did not have any discontinuities.[60,91] The five discontinuous samples depict five possible production limitations. These limitations can be caused due to geometrical and/or draping allowance.[29,68,69]

The sample types #1, #2, and #3 depict interply discontinuities. The types #1 and #3 had resin pockets between the layers. Type #1 and #2 had the discontinuous layer in the middle layers, yet #3 had the discontinuity on the surface. Thus, #3 is expected to have the most inferior quasistatic and fatigue behavior of all the sample types. This expectation was based on Euler–Bernoulli beam theory. Since the surface is further away from the natural axis, the strain was more significant on the surface of the beam.[92,93] The position of the natural axis can be seen on Figure 3.40[92].
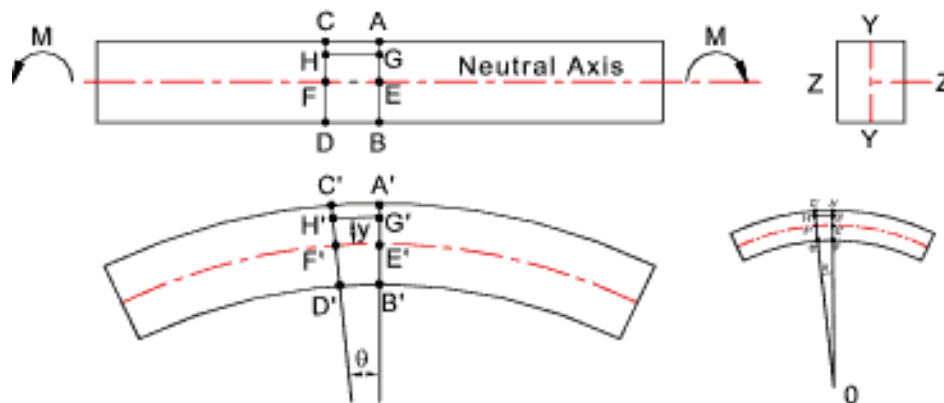
Figure 3.40. Neutral Axis of a Beam Subjected to Bending. (Source: Roymech 2022[92])

Optimal curing during compression molding requires meticulous experimentation and precise calibration for each resin type. Elevated temperature would facilitate the curing of the part starting from the outer layer, thereby preventing the removal of excessive resin from the inner portion of the part. The elevated pressure prevented the resin from flowing out of the central region of the part.

If the surplus resin cannot be eliminated, the fiber-to-resin ratio, in part, was low. Gas pockets from air or moisture, known as voids, bubbles also become trapped within the layers.[94–97] The presence of non-uniform macroscopic features in the samples led to the initiation of cracks.

There are some methods to prevent this formation, such as slowly increasing the temperature and the pressure. Also, vibrating the mold could elevate the part from having air pockets, improving the result.[95] However, in serial production, mold cooling is required for each product. Thus, would increase energy consumption as well as production time. The same principle applies to the slow pressure incremental time. Due to serial production constraints, production quality and cost must be adjusted to satisfy the required characteristics.

A summary of defects are demonstrated in Figure 3.41[97]. As demonstrated in Figure 3.41[97], our production method, hot pressing, is susceptible to voids, impurities, and resin-rich areas.[94–97]
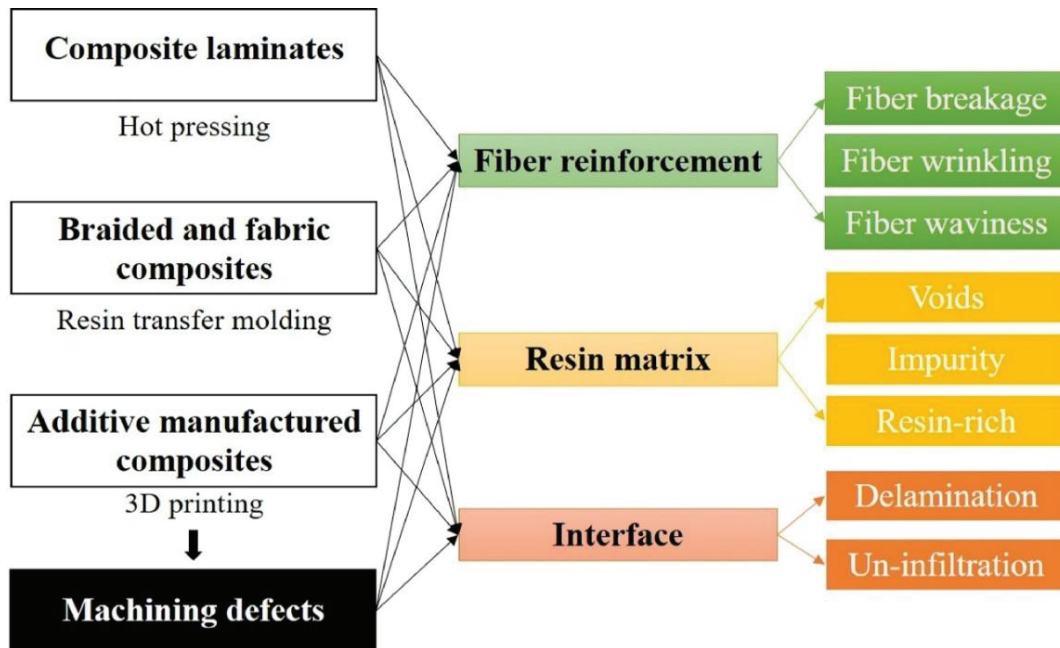
Figure 3.41. Classification of Common Composite Defects.
(Source: Fu 2022[97])

The continuous samples, #C, are a serially produced leaf spring for light commercial vehicles. All of the samples were cured according to serially produced sample, #C. The aim is to compare the field-proven sample with possible discontinuous samples. This leaf spring type was preferred among other serially produced springs. The main reason was that this spring has equal thickness across the section. Hence, this allowed us to produce a fully continuous sample that is needed, to compare with the other samples.

After curing, the voids can be seen after a sectional cut of the sample. The gaps are viewed as circle-like structures areas without matrix and fiber, as can be seen from Figure 3.42[97]. The resin flow during the curing phase shifts the fiber orientation and induces resin rich-zones, as can be seen from Figure 3.42[97]; voids do not contain any matrix (resin) or reinforcement (fiber) in them as seen on the figure.[97,98]

An automated cutter was used to slit the layers from a rolled sheet of prepreg according to each layer's form. The layers are placed on top of each other according to their respective layup designs. A roller made of PTFE was used for hand consolidation.

The produced parts are placed on a preform to allow them to be easily placed on the press mold. If the preform is not used, placing the procured parts touches the mold unevenly. The center of the sample touches the rest of the part. Thus, the surface would be heated unequally.
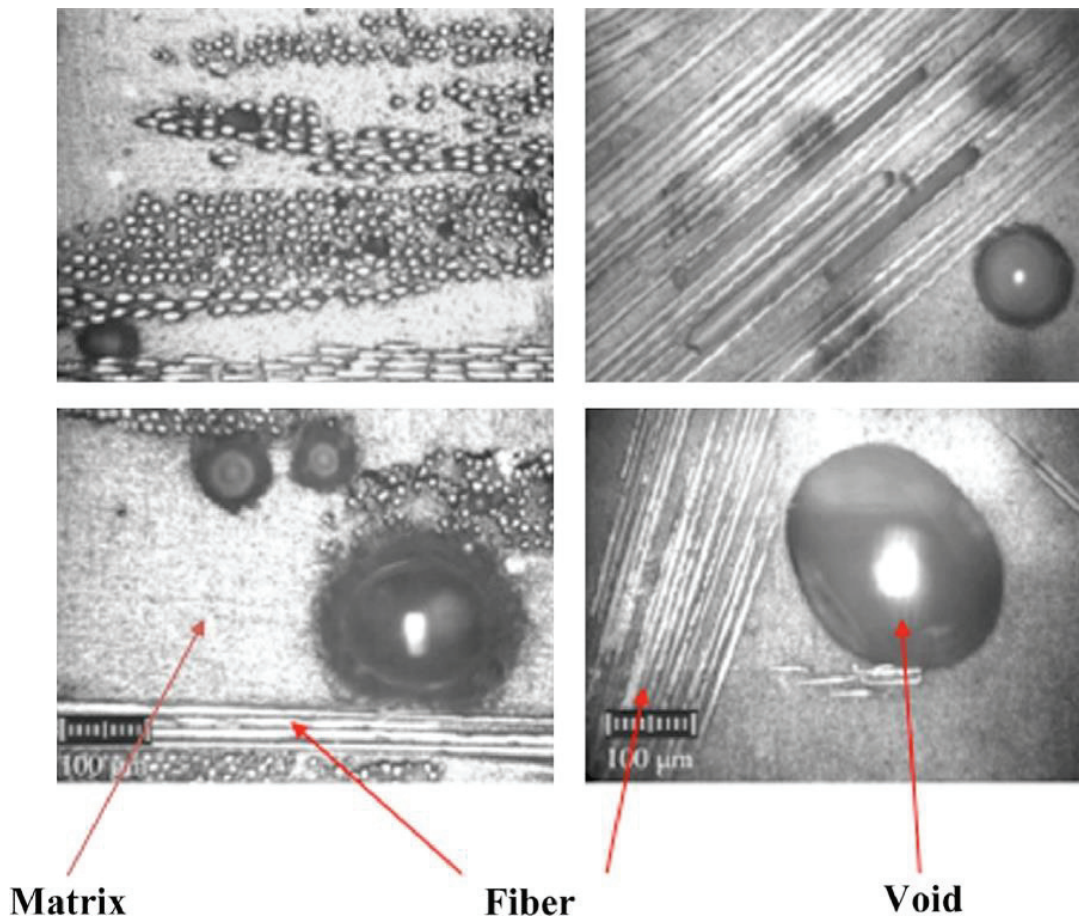
Figure 3.42. Microscopic Images of Voids and Resin-Rich Areas.

(Source: Fu 2022[97])

3.3.2.1. Production of Continuous Samples

The continuous samples, Sample#C, were produced using standard procedures, as were the other samples. 43 layers of continuous plies arranged on top of each other. The cured sample in the mold can be seen on Figure 3.43. The sample number and type were written on the spring to prevent sample mix-up.

3.3.2.2. Production of Sample #1

Sample #1 needs a layup diagram since the layup order changed on layers. The Figure 3.44 shows the layer order of this sample. The PTFE roller was used to consolidate the layers on each layer.

The hand layup process of Sample 1 can be seen on Figure 3.44. Each layer's cover film is removed and placed on top of each other according to the layup order diagram. Due to the discontinuities' form, there are gaps at the layer change areas. The gaps can be seen on Figure 3.45.

The hand rolling and even the preform did not close the gaps as can be seen on Figure 3.46. After the press curing is done the gaps are still visible. The cured sample #1 center area can be seen on Figure 3.48.

Drop-off area gaps can be seen in the red circles. These drop-off areas are precursors of the resin pockets. The triangular gaps can induce voids and resin-rich areas. Similarly, the gasp is shown while the sample is on the consolidation table as in Figure 3.46. The size of the gaps is still considerable when the sample is not cured. These gaps are filled with air and also moisture.

The curing process removed some portion of the air gaps, yet the discontinuous zones are present within the sample, as seen in Figure 3.48. It can also be noted that the fiber directions change during the curing process.
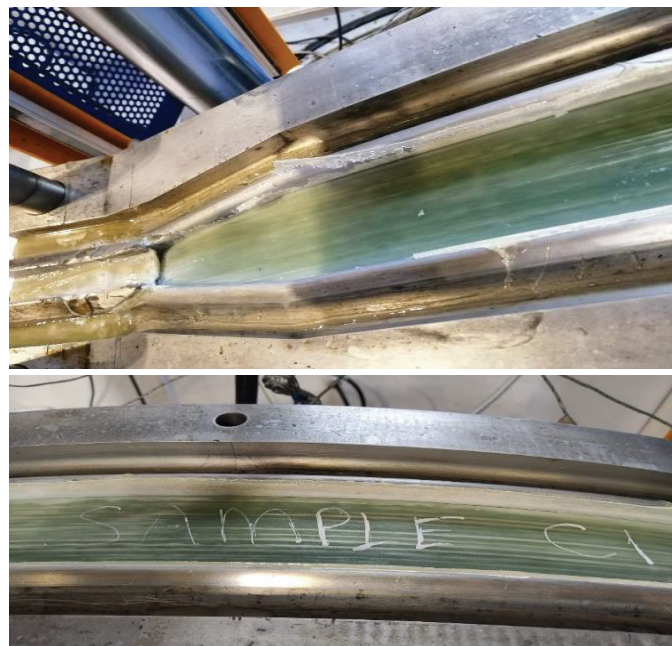
Figure 3.43. Sample #C in the pressure mold.
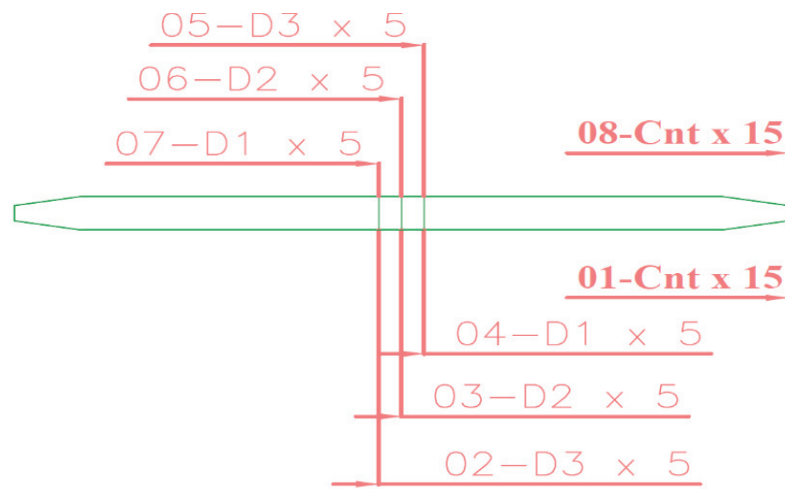
Figure 3.44. Layup Order for Sample #1.
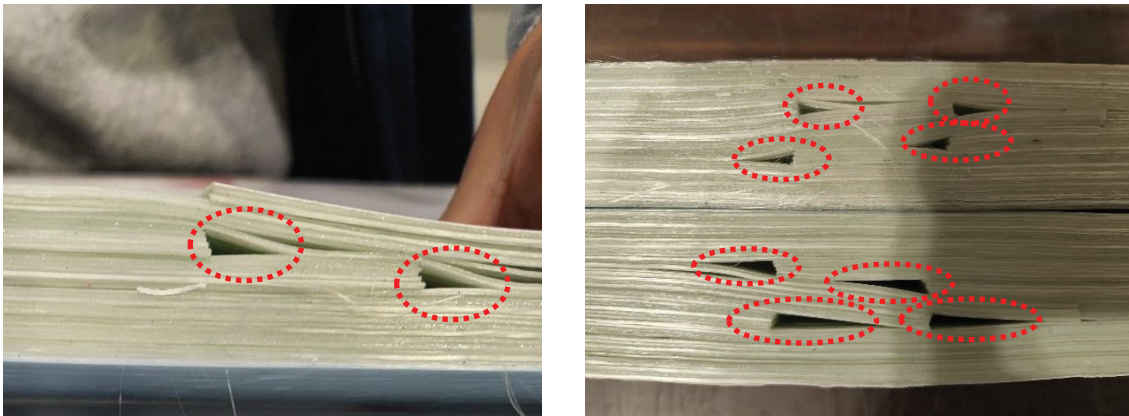
Figure 3.45. Sample #1 Gaps between layers.

Figure 3.46. Sample #1 Center Area on Preform Table.
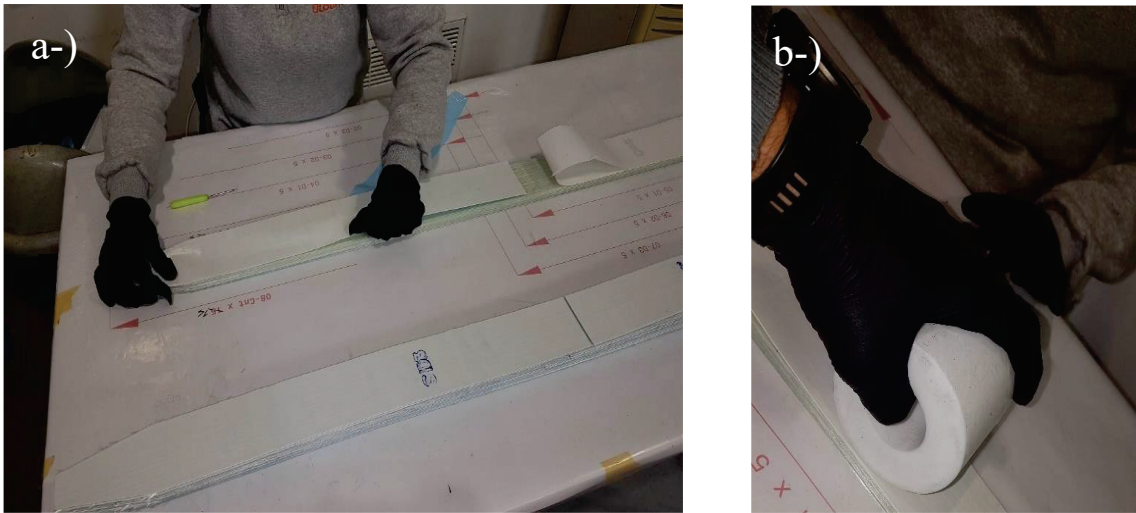
Figure 3.47. Sample #1 Prepereg Layup Process. a-) Prepereg Layup b-)PTFE roller consolidation process
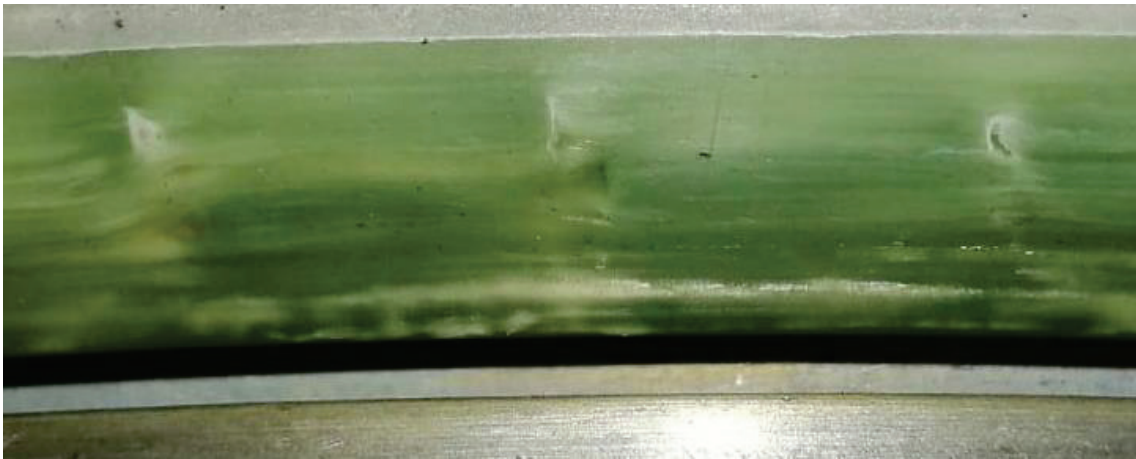
Figure 3.48. Sample #1 After Press Curing.

3.3.2.3. Production of Sample #2

Sample #2 needed a layup diagram since the layup order is changing on layers. The Figure 3.49 shows the layer order of this sample. The PTFE roller is used to consolidate the layers on each layer.

Sample #2 has fewer gaps between the layers than Sample #1. The discontinuities are edge-to-edge, allowing the pre-cure gaps to be minor, as can be seen on Figure 3.50. This method allows minimum gap voids.

Thus, the results are expected to be better on all three samples, namely #1, #2, and #3. Drop-off area gaps can be seen in the red circles. This drop-off area was a precursor of the resin pockets. Drop-off area gaps can be seen in the red circles.
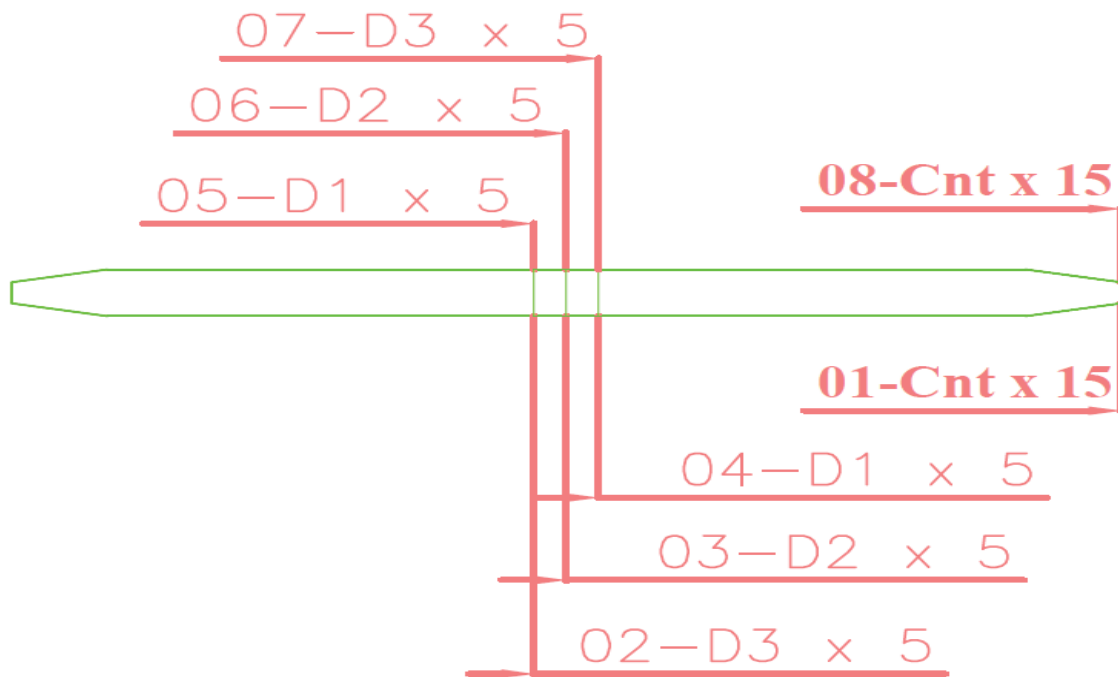
Figure 3.49. Layup Order for Sample #2.
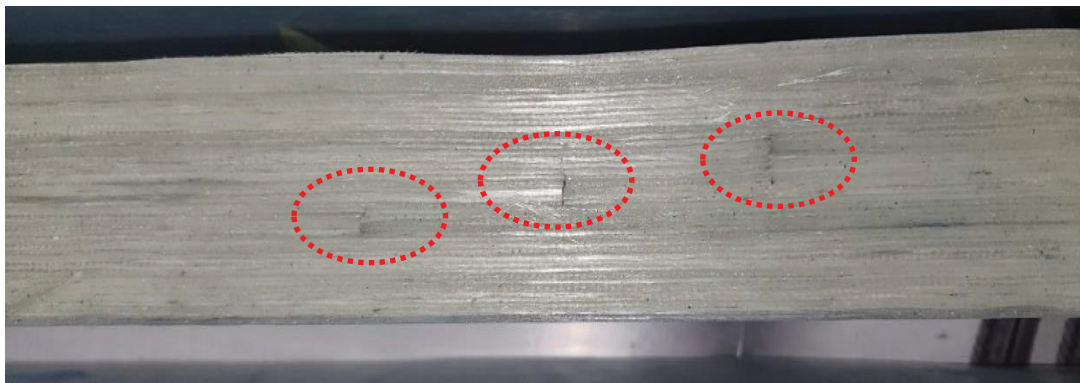
Figure 3.50. Precured Sample #2.

3.3.2.4. Production of Sample #3

This sample type is designed with the lowest static, dynamic, and fatigue life. The main reason is to determine the lowest result combination possible. The layup order can be seen on Figure 3.51. Also, this combination can be used to determine crash box design for vehicles that use the crash boxes for towing.

The resin pockets are on the surface where the highest strain is. The cured product also has air bubbles on the surface. The cured sample #3 can be seen on Figure 3.52. Voids and moisture within the layers might not be filled with resin, which induces gaps and bubbles between the matrix and fiber. The foam on the tension surface promoted fast crack propagation, and the resin-rich tension surface increased brittle behavior.
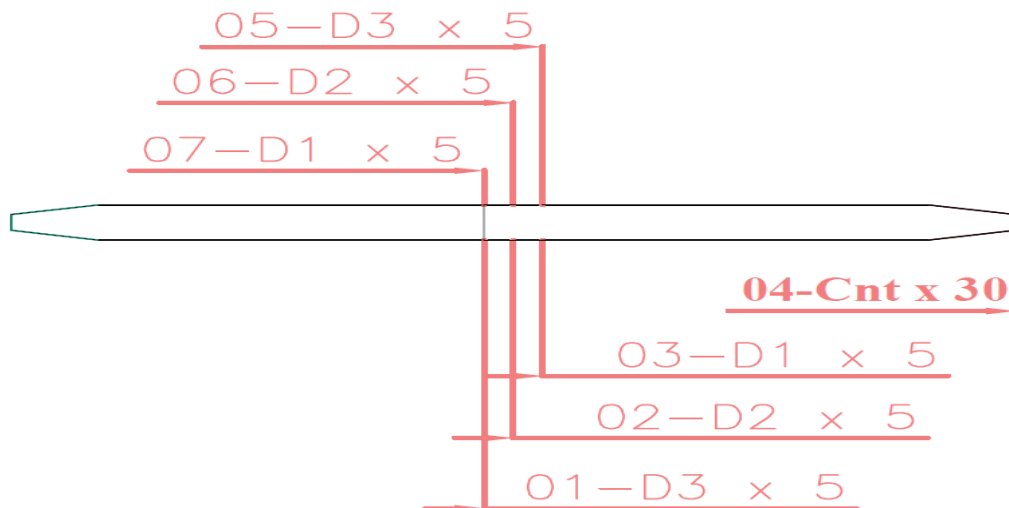
Figure 3.51. Layup Order for Sample #3.

Sample #3 is expected to be the least successful sample. During the curing, air gaps formed on the sides of the samples. These gaps can be seen on Figure 3.54. The effects of these gaps were determined during the tests.

3.3.2.5. Production of Sample #4

Sample #4 was one of the two Intraply discontinuity samples. Due to the same ply on every layer, there was no layup book. This sample has the cut-out at the outer sides of the center area. This made the resin pockets on the sides of the samples. The procured Sample #4 on the performing table can be seen on Figure 3.53.

3.3.2.6. Production of Sample #5

Sample #5 was the other Intraply discontinuity sample. Due to the same ply on every layer, there was no layup book. This sample has the cut-out at the inner side of the center area, as can be seen on Figure 3.55.This made the resin pockets in the middle of the samples. The procured Sample #5 on the performing table can be seen on Figure 3.56. The fibers at the central area spread to fill the central gap, yet there is a resin-rich area at the immediate center.

3.3.3. Post-curing Process of the Samples

In serial production, compression-molded composite materials usually get removed early enough to be handled in curing. This method is used to utilize the press and the mold more efficiently. After the products were pre-cured, they were post-cured in an oven batch by batch. The ovens have more space; thus, they can post-cure numerous products simultaneously more energy-efficiently. The heated molds were set to a higher temperature than ovens for faster pre-curing. This makes heated molds have a more significant temperature difference between their surroundings. As a result, it induced more heat and energy and caused mold loss.

If there is a mechanical operation on the final product, it should be done before the post-curing stage or reduce the overall strength of the final product. The comparison can be seen on Figure 3.57[99].

After the pre-curing and mechanical operations, such as drilling and milling, the materials were post-cured to achieve their ultimate strength and toughness. Infrared heating results were better than those of microwave heating.[99] The temperature and the duration can vary by the matrix.[100,101] The best results should be tested for better outcomes, as can be seen on Table 3.15[100]. In Table 3.15 Young's modulus (GPa), maximal stress (MPa), and strain (%) of the epoxy resin post-cured at 100, 120 and 150°C.

The samples built for this study are cured using the serially produced and proven method of 12 hours post-curing at 90°C. Since the test was conducted on bare leave springs, there was no mechanical operation on the springs; it was deburring. After the deburring, the samples are placed on a curing cart and put in the electric oven at 90°C for 12 hours, as the serial production method was the same. The cart can be seen on Figure 3.58

3.3.4. Comparison of Beam Samples

In this section, a brief comparison of the beam samples can be seen. Interply comparison can be seen on Figure 3.59. Discontinuous Sample Graphical Comparison.. This brief illustration shows the difference between them. The comparison shows that the spring samples were grouped into two prominent families. So, the test results would simulate the real lie conditions.
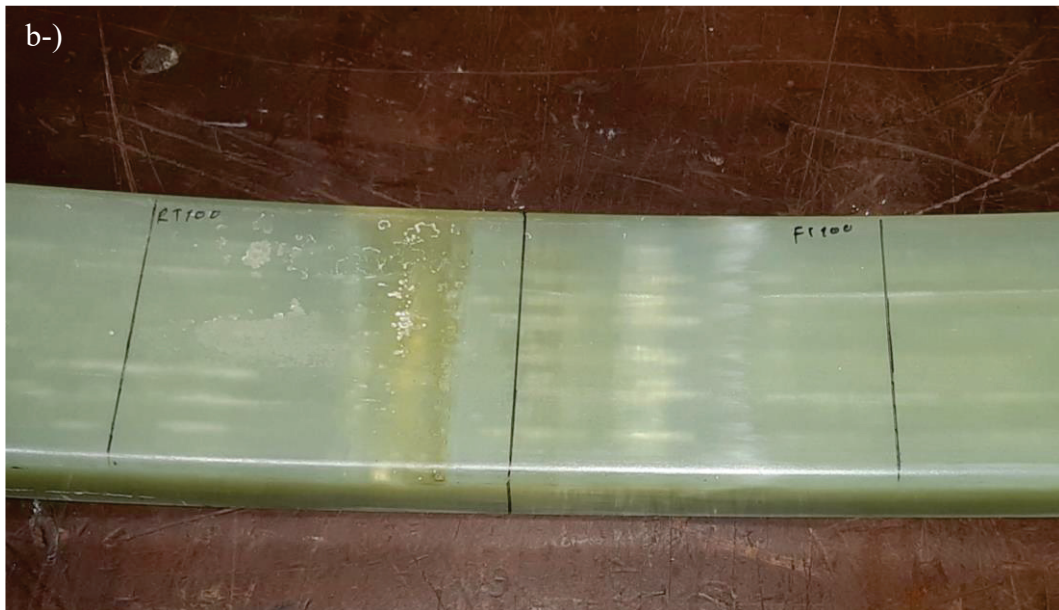
Figure 3.52. Sample #3 cured the sample's center in the mold. a-) Compression side (Top side of the spring), b-) Tension side after curing (Bottom Side).

Figure 3.53. Sample #4 on the perform table.

Figure 3.54. Airgaps on the sides of Sample #4.
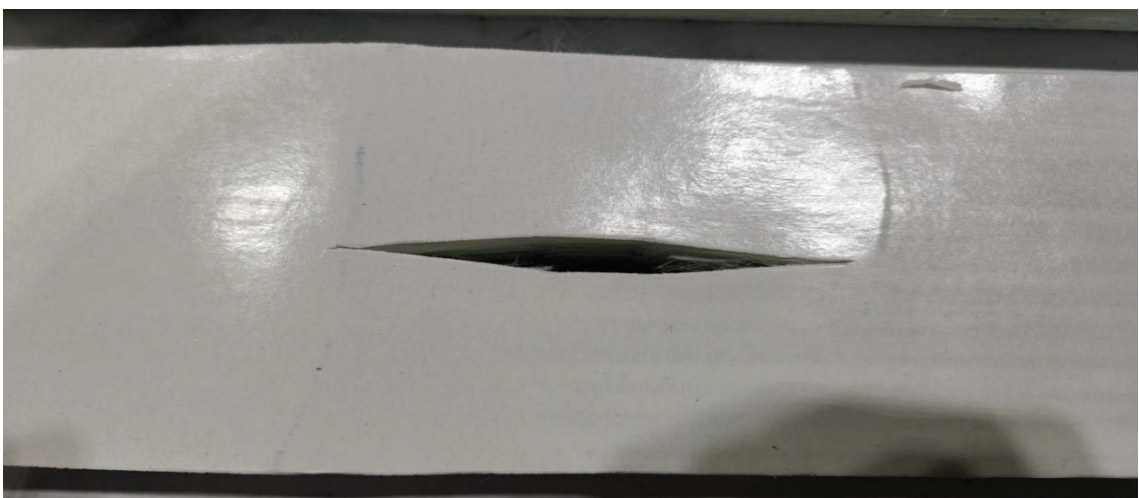
Figure 3.55. Sample #5 Precure Centre Area.
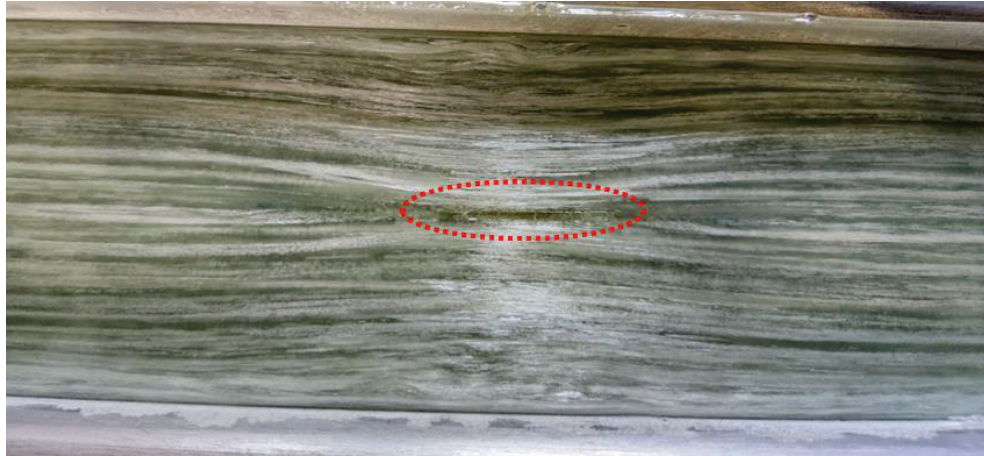
Figure 3.56. Sample #5 After Being Cured.
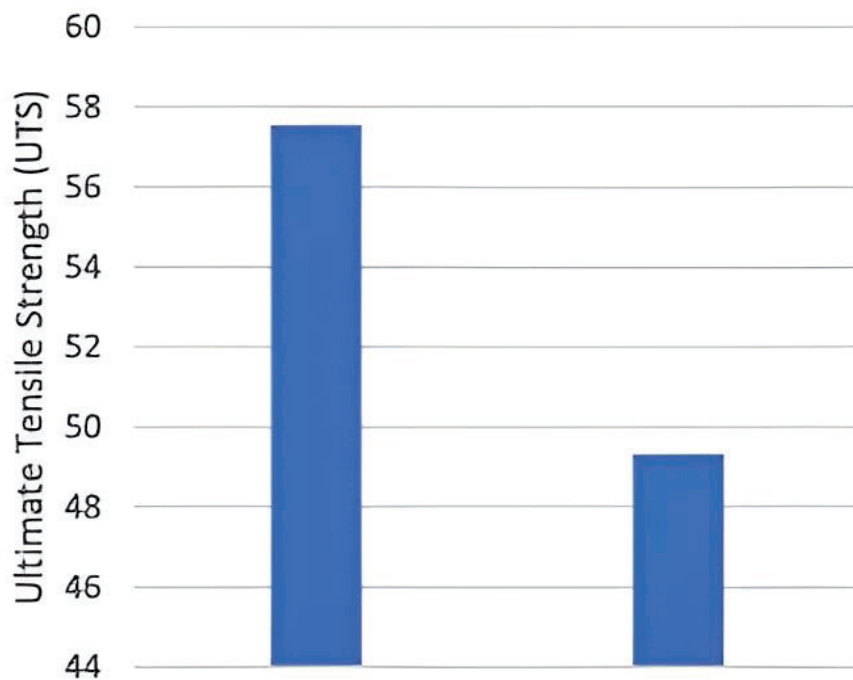
Figure 3.57. UTS Comparison of Mechanical Operations on Laminates.

(Source: Yathisha 2021[99])

Table 3.15. Mechanical Properties of the Samples (Source: Campana 2018[100])

Sample	R-NoPC	R-PC100	R-PC120	R-PC150
Modulus (GPa) according to ISO 527	3.4 ± 0.52	2.7 ± 0.27	2.9 ± 0.06	2.9 ± 0.37
Maximal tensile strength (MPa)	68 ± 8.1	69 ± 5.2	66 ± 3.2	54 ± 3.8
Elongation at break (%)	2.67 ± 0.54	3.56 ± 0.56	3.33 ± 0.04	3.12 ± 0.43

R-NoPC, Sample with no post-curing. R-PC100 Sample post-cured two hours at 100°C. R-PC120, Sample post-cured for two hours at 120°C. R-PC150, sample post-cured for two hours at 150°C.

Figure 3.58. Samples on the curing cart

3.3.5. Microscopic Imaging of Discontinuity Zones

Microscopic examination of the discontinuity zone revealed specific details. Sample#3 was excluded because its design produces a low-quality output. To fatigue test the leaf spring samples, first, the samples would be evaluated for maximum quasistatic loading. Since the fatigue testing cannot exceed this level. Studies conducted to compare the quasistatic and dynamic test results, such as those by Stephen B Clay[102–104] et al.

The quasistatic 3-point bending test, Fmax, was conducted with at least two samples, one with strain gauges. The strain gauges would be used to determine strain levels. Strain tests were conducted on the serially produced sprigs for vehicle conditions. The strain levels on all sample types are planned to match the serially produced versions. Yet the Fmax test would help us decide the strain levels.

The discontinuity zone of Sample#1 can be seen from Figure 3.60. In Figure 3.60 The blue arrow indicates that the fibers and the resin-rich zone can be seen. On Figure 3.60 b the blackish zones are polishing residues and should not be considered sample defects. Yet the brownish is caused by overheating or an excessive exothermic reaction. Resin pockets can induce excessive heat, reduce mechanical properties, and induce internal stresses.[105,106]

#1

#2

#3

#4
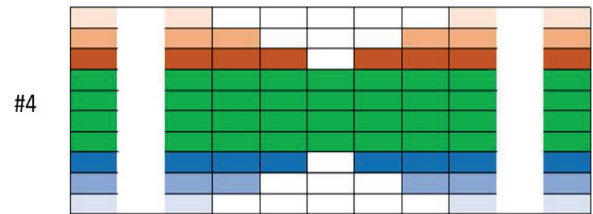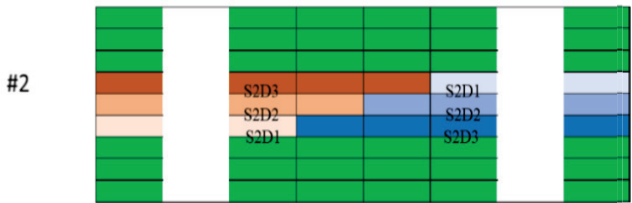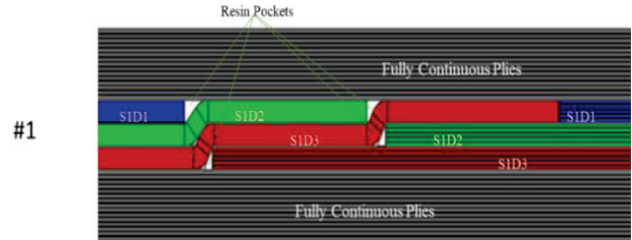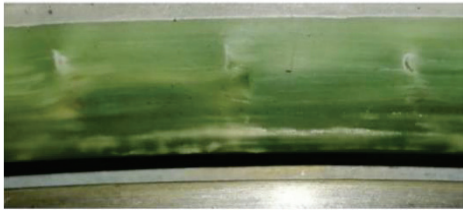
Side view of sample #4

#5
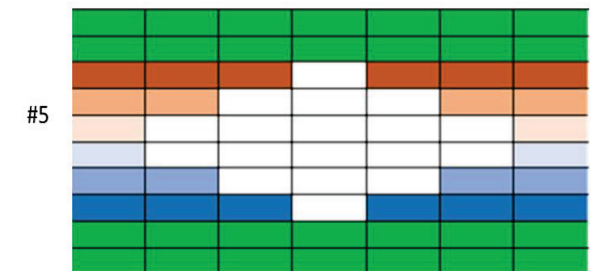
Top view of sample #5

Figure 3.59. Discontinuous Sample Graphical Comparison.
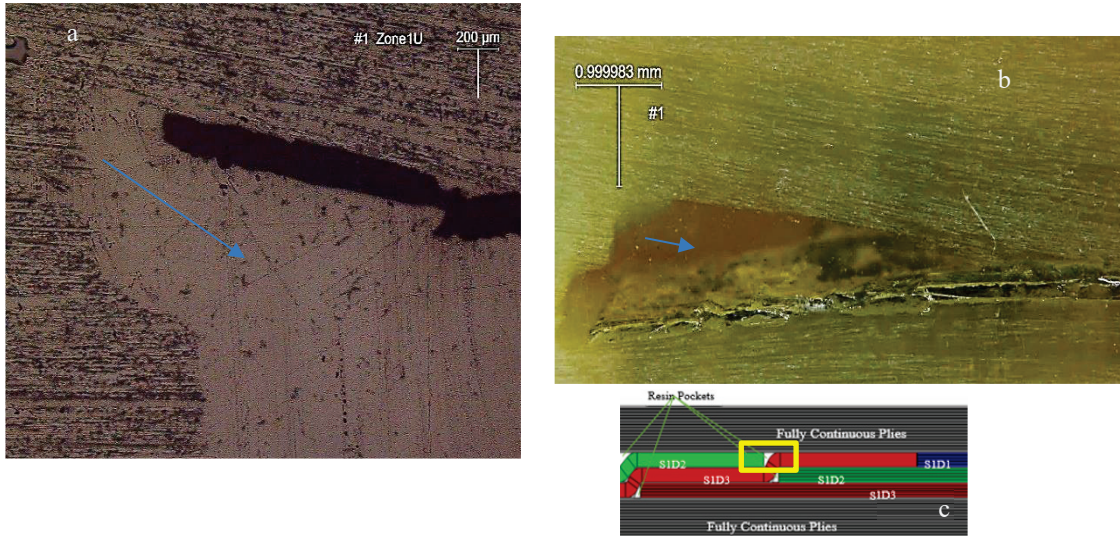
Figure 3.60. Sample#1 Discontinuous zone microscopic view. a-Sample#1 Discontinuous zone microscopic view blue arrow depicts resin-rich area. b- The half view of the discontinuous zone depicts the general view. c- Depicts the cut-off sample position.

In Figure 3.61 the resin pockets of Sample#2 are shown with blue arrows. As can be seen from the Figure 3.61 the cut layers have shifted and created resin pockets during the curing phase. During the pressing, the liquefied resin induces a slippery medium for the fibers to move quickly. During the pressing phase, the resin and fibers flow to the edges of the mold. Thus, the fiber moves away from its position. The place is filled with resin, and the resin pocket induces an exothermic reaction as in all other samples
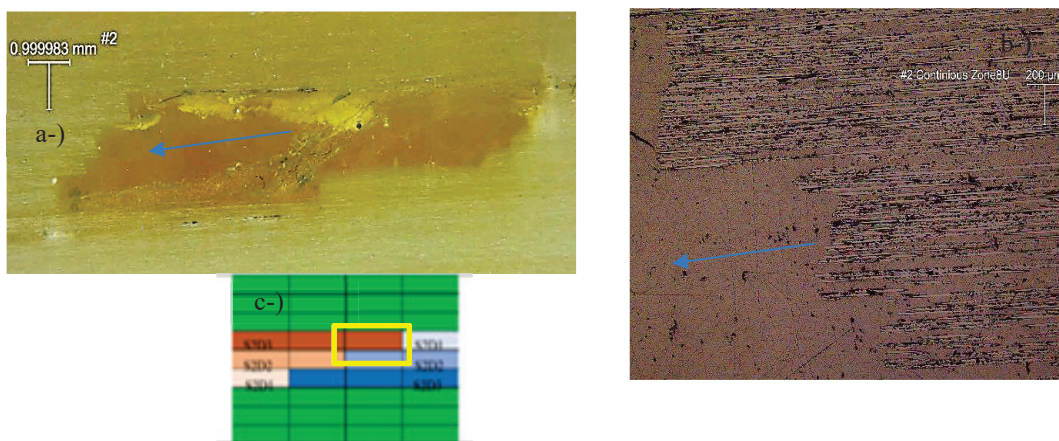
Figure 3.61. Sample#2 Discontinuous zone microscopic view. a-Sample#2 Discontinuous zone microscopic view. b- The half view of the discontinuous zone depicts the general view. c- Depicts the cut-off sample position.

The draping limitations and resin prevented the full spread and left some portions of the gap filled with pure resin, as can be seen from the images Figure 3.63 depicts a microscopic view of Sample#5's discontinuity zone. The pointing line is drawn to help detect the discontinuous zone. Below the line, the fiber bundles can be seen forming a triangle-like shape, as can be seen from the red line. Figure 3.63 a and b are mirror symmetrical. The point line in "a" is drawn to help detect the discontinuity zone. Above the zone, the fiber bundles can be seen. These fiber bundles have moved away from the center of the spring due to pressing forces and tried to fill the side gaps. The draping limitations and resin prevented full spread and left some portions of the gap filled with pure resin, as seen from the images. The main difference in Figure 3.64 is that it clearly shows exothermic resin deformation. Due to this resin pocket being located in the middle of the sample and unable to eject the excess resin and heat outside of this resin pocket, it seems to lead to this exothermic resin failure.

Figure 3.62 Sample#4 Discontinuous zone microscopic view. a-Sample#4 Discontinuous zone microscopic view. The pointing line is drawn to help detect the discontinuous zone. Below the line, the fibers can be seen forming a triangle-like shape, as can be seen from the red line. b- The half view of the discontinuous zone depicts the general view. The sample is below the red line, and the upper part is the clear resin used for the sample preparation. c- Depicts the cut-off sample position.
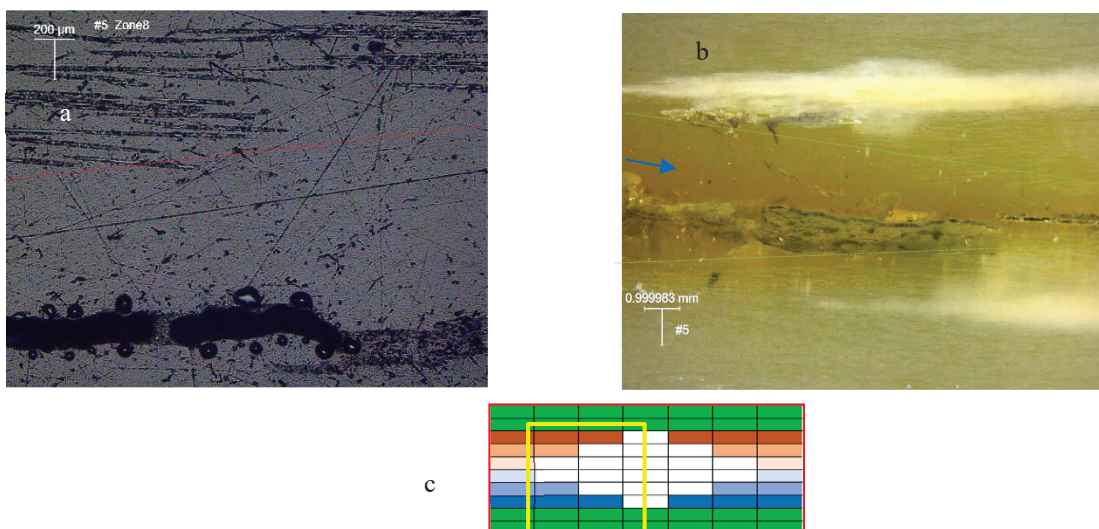
Figure 3.63. Sample#5 a- Discontinuous zone microscopic view. b- The half view of the discontinuous zone depicts the generally. The blue arrow depicts the exothermic reaction accrued withing the resin pocket. c- Depicts the cut-off sample position.

3.3.6. FVF of Discontinuous Zones

Sample#3 was left out because of its design results output in FVF tests. The parts' fiber volume fraction (FVF) is measured in numerous sections due to the varied continuity of the internal layup architecture according to ASTM D2584 [71].

Sample#C's FVF samples can be seen on Table 3.16 that shows FVF results. This sample is the base sample for the discontinuous samples. Sample#1's FVF samples can be seen on Figure 3.65 and Table 3.17 shows FVF results. The discontinuous points are especially included in the FVF test to better determine the distribution of the fiber-matrix content. Sample#2's FVF samples can be seen on Figure 3.66 and Table 3.18 shows FVF results. Sample#4's FVF samples can be seen on Figure 3.67 and Table 3.19 shows FVF results. Sample#5's FVF samples can be seen on Figure 3.68 and Table 3.20 shows FVF results. The discontinuous zones resemble lowered fiber concentration, as seen in the tables.
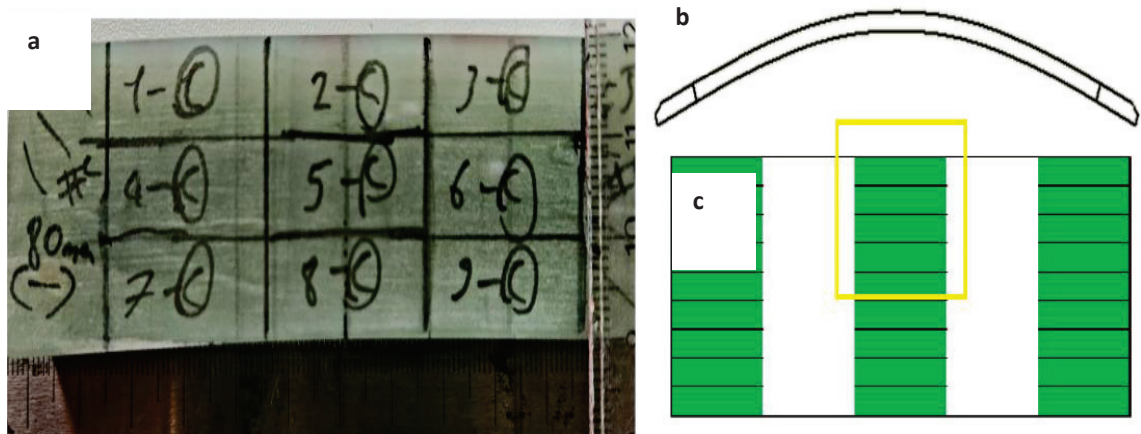
Figure 3.64. Sample#C FVF Sections. a-Sections of the sample b-General demonstration of beam c-Position of FVF section on the sample's layup marked with yellow rectangular.

Table 3.16. Fiber Volume Fraction of Sample#C.

1	59.8%	2	57.9%	3	58.4%
4	49.7%	5	49.6%	6	52.8%
7	48.9%	8	53.7%	9	52.9%

Table 3.17. FVF of Sample#1.

1	45.7%	2	43.6%	3	43.5%
4	52.2%	5	43.3%	6	44.0%
7	45.7%	8	43.4%	9	42.3%

Table 3.18. FVF of Sample#2.

1	41.9%	2	41.3%	3	41.7%
4	47.3%	5	49.2%	6	46.8%
7	46.3%	8	36.9%	9	44.6%
10	41.8%	11	42.2%	12	42.9%
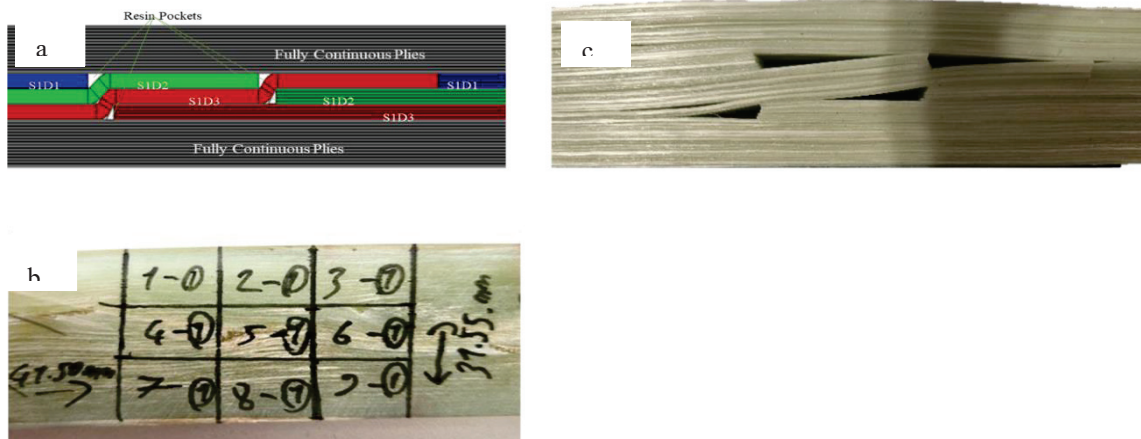
Figure 3.65. Sample#1 FVF Sections. a-Sections of the sample b-Precured sample c-Position of FVF section on the sample's layup.
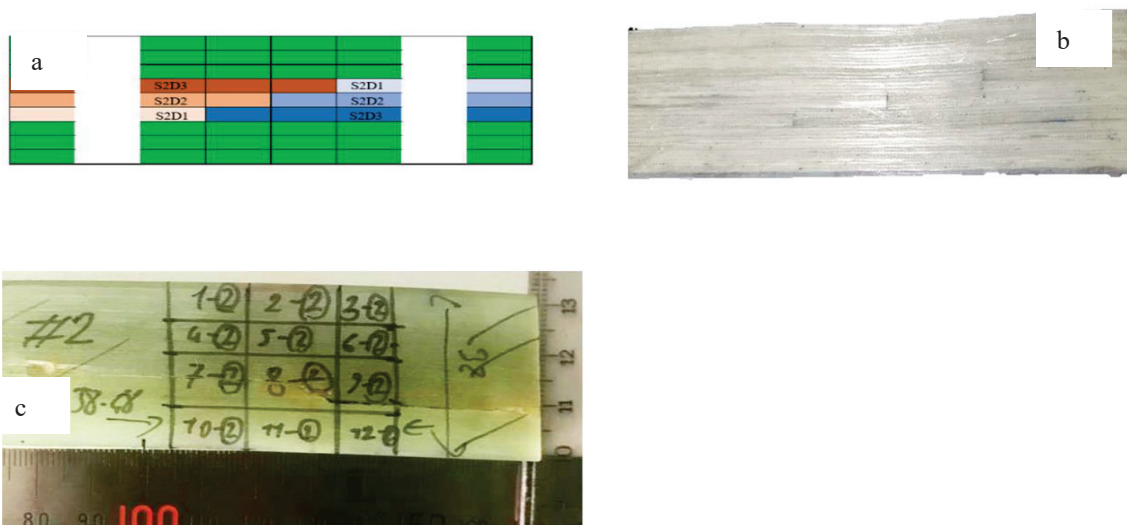
Figure 3.66. Sample#2 FVF Sections. a-Sections of the sample b-Precured sample c-Position of FVF section on the sample's layup.
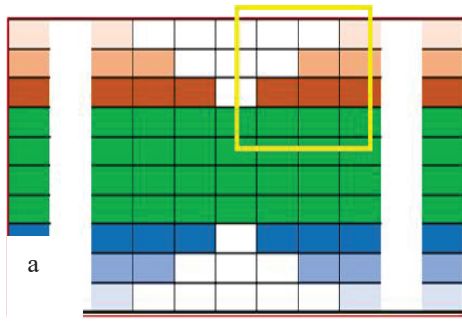
Figure 3.67. Sample#4 FVF Sections. a-Sections of the sample b-Precured sample c-Position of FVF section on the sample's layup.
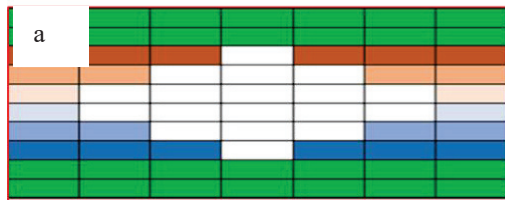
Figure 3.68. Sample#5 FVF Sections. a-Sections of the sample b-Cured sample c-Position of FVF section on the sample's layup

Table 3.19. FVF of Sample#4.

1	41.9%	2	41.3%	3	41.7%
4	47.3%	5	49.2%	6	46.8%
7	46.3%	8	36.9%	9	44.6%
10	41.8%	11	42.2%	12	42.9%

Table 3.20. FVF of Sample#5.

1	52.4%	2	52.6%	3	53.2%
4	47.8%	5	48.1%	6	47.9%
7	48.8%	8	46.2%	9	47.3%
10	29.4%	11	37.6%	12	41.9%
13	44.2%	14	45.9%	15	47.7%
16	48.8%	17	48.7%	18	53.2%
19	66.7%	20	66.5%	21	66.5%

3.4. Test Rig

The test rig consists of two fixed rollers and one servo-hydraulically controlled actuator. The spring is fixed at the center. The aim is to inflict the most strain at the center of the spring, where all the discontinuity is located.

To increase the effects of the strain, the central bracket consists of two steel plates with cylindrical contact points to the spring. The cylinders are made of polyoxymethylene (POM), which prevents the spring surface from being damaged due to scratches and penetration. The test rig can be seen on Figure 3.70.

A specialized rig test was conducted to determine the maximum flexural stress that composite beams could withstand. Stephen B. Clay and colleagues conducted a study to evaluate the maximum force capacity (Fmax) using 3-point bending. Strain gauges were used to measure strain levels and establish a comparison baseline using computer-aided engineering (CAE). A rig test was conducted to determine the maximum flexural stress that composite beams could withstand. Stephen B. Clay and colleagues conducted a study using the 3-point bending test to measure the maximal force capacity (Fmax). Strain gauges were used to measure strain levels and establish a comparison baseline using computer-aided engineering (CAE). The strain tests were carried out using springs obtained from mass-produced cars. The samples showed strain concentrations that met the specifications of the manufactured versions.

The strain tests were conducted using springs obtained from mass-produced automobiles. The samples showed strain concentrations that satisfied the specifications of the manufactured versions.

The Fmax test was utilized to verify the strain levels. The testing includes one actuator controlled by a servo-hydraulic system and two fixed rollers in the test setup. The central part of the beam is securely attached to focus the greatest stress on the spring's midpoint, where all imperfections are situated.

The central bracket is engineered to enhance the strain's impact by employing two steel plates that contact cylindrical locations on the spring. They utilized the Fmax test to validate the strain levels. Testing includes one actuator operated by a servo-hydraulic system and two fixed rollers. The central part of the beam is securely attached to focus the most stress on the spring's center, where any imperfections are situated.

The middle bracket increases the strain's effect by including two steel plates that contact cylindrical areas on the spring. Polyoxymethylene (POM) cylinders shield the steel plates to prevent damage from abrasion or penetration. Figure 3.70 displays the test setup.

To prevent pressure on the spring, the actuator is securely attached to limit its movement to the vertical plane. A distance of 1100 millimeters separates each fixed roller. The rollers in each sample remain in their original positions.
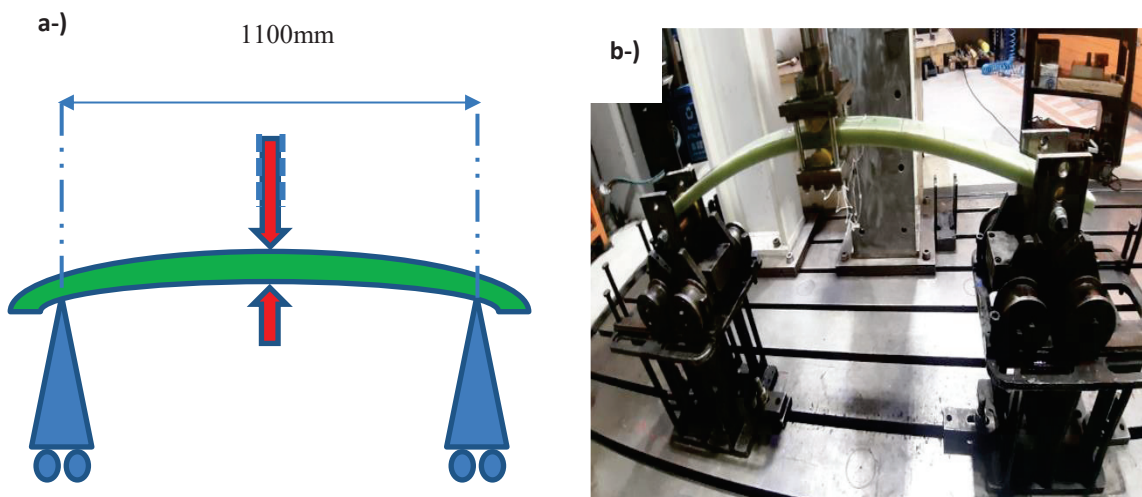
Figure 3.70. Test Rig with a Strain Gauged Spring. a-) Illustration with dimensions, b-) actual picture of the rig.

3.4.1. Maximum Load Strain Gauge Samples

There are 6 strain gauges placed on each sample. As can be seen from the previous chapters there are two discontinuities on each arm of the spring. Thus, four strain gauges were placed at the tension surface, two more were placed on the compression side of the spring in order to compare the balance of the tension compression sides. The gauges can be seen on Figure 3.71.
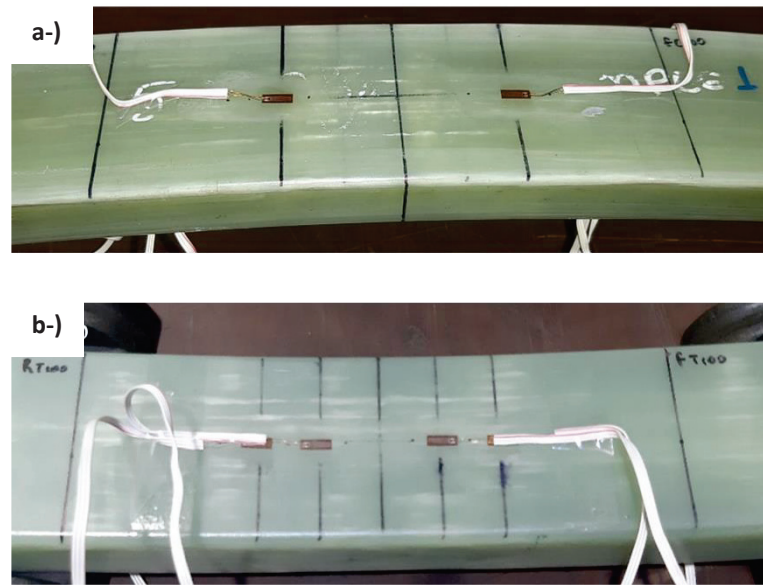
Figure 3.71. Strain Gauge Placement on the Samples a-Tension Side b-Compression Side.

3.4.2. F-Max Flexural Test Results and Discussion

Continuous test results were conducted to use as a baseline. Some of the samples can be seen in Figure 3.72. All the samples failed at the compression side fiber failure, followed by matrix failure.

Sample #1 test shows resin pocket failure followed by delamination. Failure started at the resin pockets. The samples can be seen on Figure 3.73. The resin pockets induced crack propagation. Sample #2 test shows delamination failure. Failure started at the resin pockets. The samples can be seen on Figure 3.74 The resin pockets induced crack propagation.

Sample #3 test shows delamination failure. Failure started at drop-off areas. The samples can be seen on Figure 3.75. The discontinuities are furthest from the natural axis;

this increases the effect more than the other samples due to the higher stress the resin pockets induced crack propagation. Sample #4 test shows delamination failure and behaves similarly to Sample #C. Failure started at the central cut-off area. The samples can be seen in Figure 3.76, where the resin pockets induced crack propagation.

Figure 3.72. Sample #C Fmax Test. a-Sample 1 after the test b-Sample 2 after the test c-Sample 1 after the break at the rig d- sample 3 after the test.
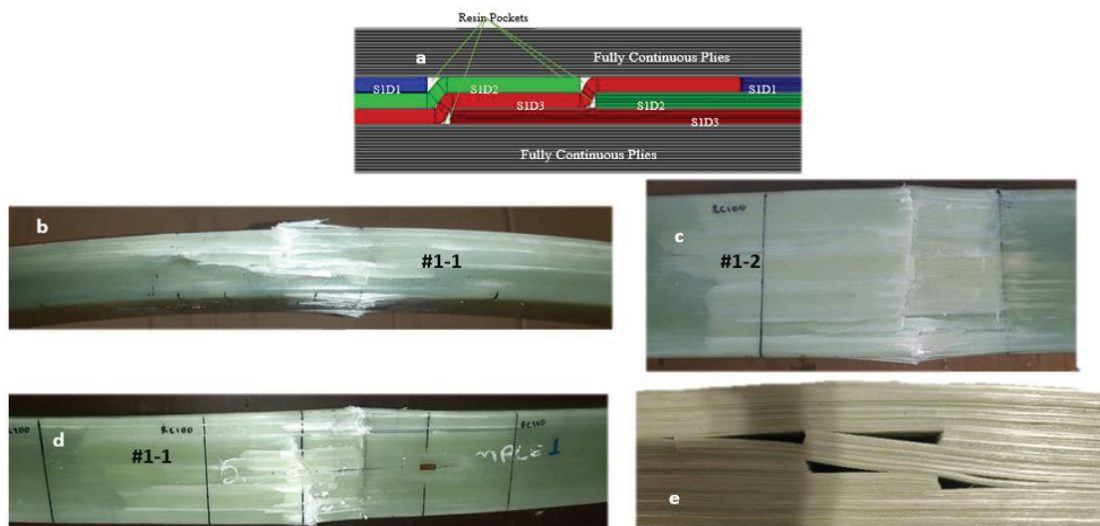
Figure 3.73. Sample #1 Fmax Test. a-General layout design of Sample #1 b-Sample#1-1 after the test side view c-Sample#1-2 after the test compression sided-Sample#1-1 after break compression side e- Sample#1 actual stack up before press forming.
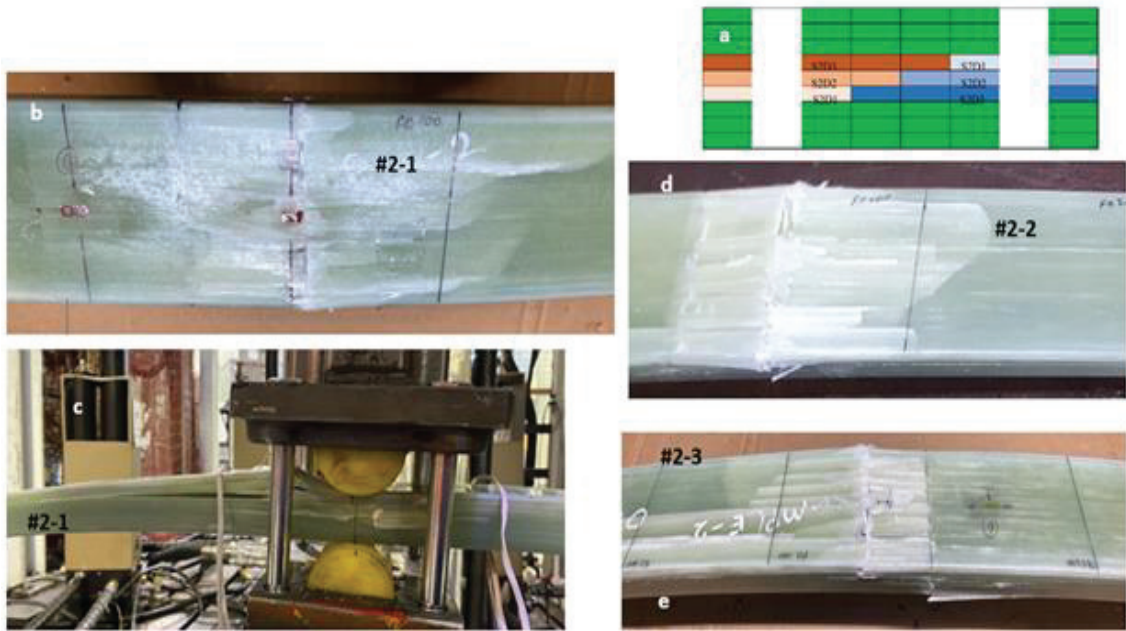
Figure 3.74. Sample #2 Fmax Test. a-General layout design of Sample #2 b-Sample#2-1 after breaking compression side c- Sample #2-1 breaking on fixture side view d- Sample#2-2 after breaking compression side e-Sample#2-3 after breaking compression side.
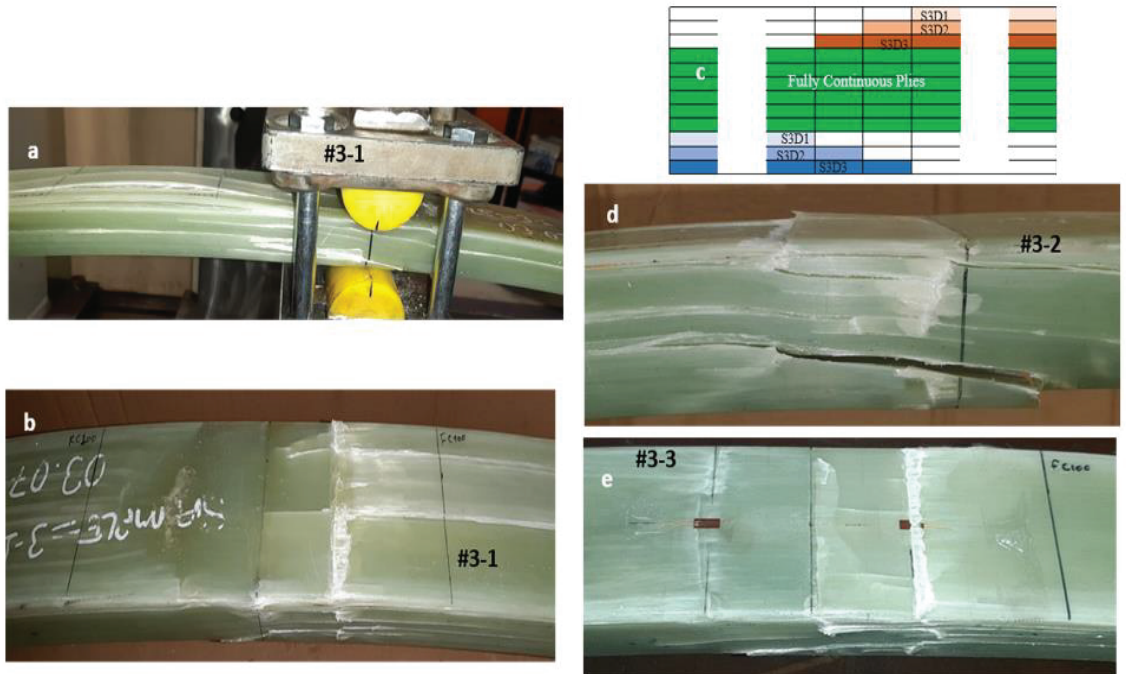
Figure 3.75. Sample #3 Fmax Test. a-Failed Sample#3-1 at the rig b-Sample#3-1 after breaking compression side c- General layout design of Sample #3 d-Sample#3-2 after breaking side view e-Sample 3 after breaking compression side.

Sample #5 test shows delamination failure and behaves similarly to Sample #C. Failure started at the central, where the Fiber Volume Ratio was lower than the rest of the sample. The samples can be seen on Figure 3.77. The resin pockets induced crack propagation.
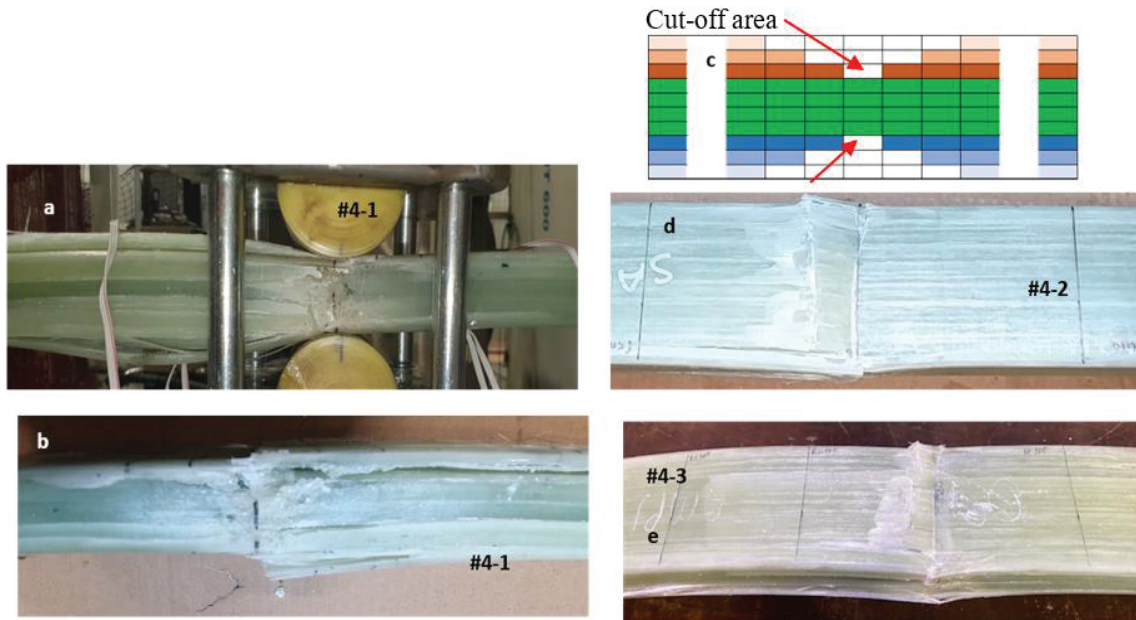
Figure 3.76. Sample #4 Fmax Test. a-Failed Sample#4-1 at the rig b-Sample#4-1 after breaking side view c- General layout design of Sample #4 top view d- Sample#4-2 after breaking side view e-Sample#4-3 after breaking compression side.

Fmax test results can be seen in Table 3.21. There are some strain gauges that failed the test due to the failure zone. Table 3.21 shows that Sample #1 behaves more brittle than Sample #C. This can be seen from less displacement at failure. Also, this brittle behavior leads to low-force load failure. The brittle characteristics do not lower the rate of sample #1. Nevertheless, the strain is lower than Sample #C. The brittle behavior is caused due to resin pockets.

Sample #2 shows strain and rate characteristics similar to those of Sample #1. Sample #2 has smaller resin pockets. This leads to higher Fmax and displacement at failure. It is clear that smaller resin gaps lead to higher strength and more challenging attributes. These results support our primary theory. The continuous fibers allow loads to be distributed evenly, yet the resin content of the discontinuity also helps with the toughness. Sample#1 has a higher gap than Sample #2. This allows the cured samples' resin pockets to have more gaps and air pockets within.

The fiber volume ratio is important in a composite material in general, as is the matrix volume ratio in the drop-off/cut-off areas. The air gaps allow the matrix to fail earlier than it usually would. This situation can be accepted as another composite within the matrix medium. The gaps have no strength, so the new resin-air composite matrix would induce lower matrix strength.
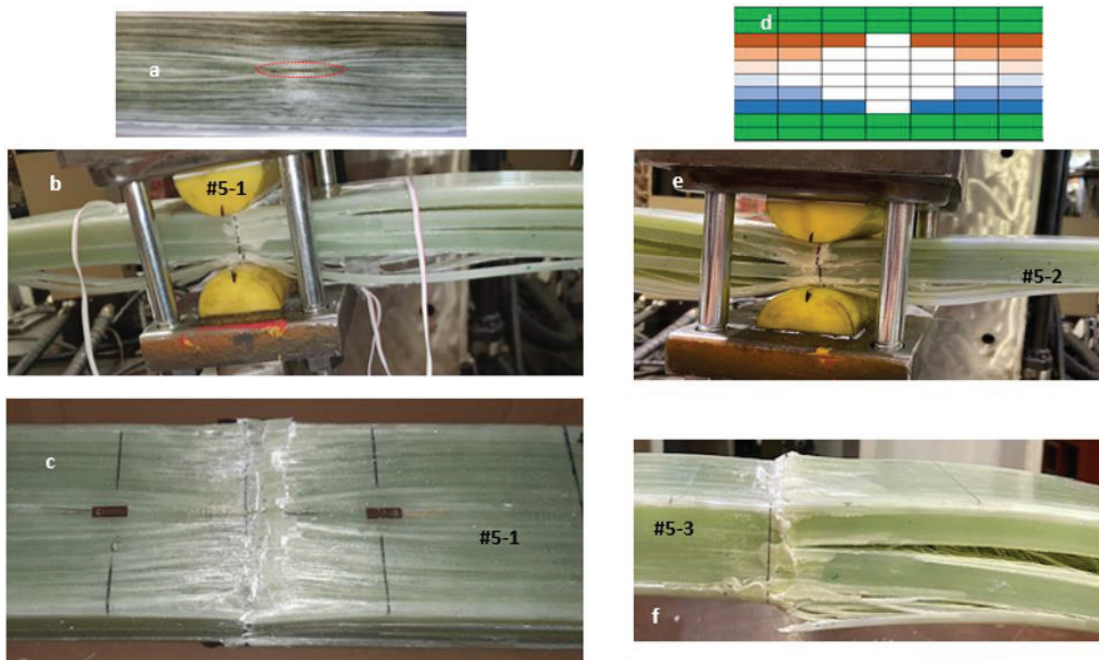
Figure 3.77. Sample #5 Fmax Test. a-Sample #5 center top view b-Sample 1 after breaking side view on the rig c- Sample 1 top view after failure d- General layout design of Sample #4 top view e-Sample 2 after failure side view on the rig f-Sample 3 after failure side view.

Sample #3 shows this phenomenon drastically. The resin gaps are on the outer side of the sample. This would lead to less resin to fill the gaps. Also, the gaps, fail initiators, are at the furthest distance to the natural axis. Thus, Sample #3 shows lowest Fmax, and displacement at failure. Also, the rate and strain characteristic of the sample is too low to compare this sample to the other 4 samples.

Sample#4 has discontinuities on the sides of the center of the spring. This intraply discontinuity lessens the continuous plies at the center. Sample #4 has less Fmax than Sample#2 due to the reduced fiber-to-volume ratio at the center. During the press curing process, the fibers stretch and fill the mold's width. Yet the lowered fiber ratio with homogenized intraply fiber distribution allows better toughness than Sample #2's interply discontinuity. The rate and strain are less than Sample #1 and Sample #2.

Table 3.21. F-Max Test Results.

#C	ΔDisplacement [mm]	Fmax [kN]	Rate [N/mm]	Max μ Strain at ±40	Max μ Strain at ±20
	158	37	231	19093	20499
	163	38	240	20499	N/A
Average	161	38	235	19796	20499
Coef. of Var.	3	1	4	703	0
#1	110	26	242	15047	14969
	104	23	246	16473	15509
Average	107	24	244	15760	15239
Coef. of Var.	3	1	2	713	270
#2	116	27	242	14509	16613
	120	28	246	16442	15922
Average	118	28	244	15475	16268
Coef. of Var.	2	0	2	967	346
#3	63	12	186	8006	6878
	64	12	194	5569	N/A
Average	63	12	190	6788	6878
Coef. of Var.	1	0	4	1219	0
#4	129	27	217	16740	18392
	130	27	206	17075	18267
Average	130	27	212	16907	18330
Coef. of Var.	0	0	6	167	62
#5	126	25	205		
	120	27	211	13311	21502
Average	123	26	208	13311	21502
Coef. of Var.	3	1	3	0	0

Sample#5 has similar intraply discontinuities like Sample#4, yet the discontinuities are at the midsection of the parts. The intraply discontinuities does not allow gaps to be filled as good as Sample #4. It can be said that in intraply discontinuities, outside gaps induce less weakening where in interply inward discontinuities provoke improved results.

The ratio between Sample#C and each of the samples in Table 3.22, this table is a simplified comparison of Table 3.22. This can be seen from the Table 3.22 that the highest Fmax is Sample#2 followed by Sample#4, Sample#5, and Sample #1. Yet Sample #4 and Sample#5 exceed Sample#2 in displacement before failure respectively; this is followed by Sample#1.

The rate of Sample #1 and Sample#2 is higher than even the continuous sample. This is caused by the resin-rich areas' brittle, harder nature. This hardness decreases the displacement and load capacity yet increases the spring rate.

Table 3.22. F-Max Test Results Ratio Comparison.

% Ratio #C vs	#1	#2	#3	#4	#5
Fmax	0.64	0.74	0.31	0.72	0.69
ΔDisplacement	0.67	0.74	0.39	0.81	0.77
Rate	1.04	1.04	0.81	0.90	0.88
% Strain	0.77	0.79	0.34	0.87	0.86

Even though Sample#3 has 0.31 load and 0.39 displacement ratio to Sample#C; due to brittle hardness introduced by the resin area Sample#3's spring rate is similar to Sample #4 and Sample#5 and equals to 0.81 of Sample#C's. This is an important finding, as even though the Strain is 0.34 of the continuous sample, the spring rate is not that drastically affected. This might indicate that the spring rate does not help identify the damage to the spring. Sample #4 has a similar spring rate and strain as Sample#5. This implies that discontinuities do not affect spring rate and strain much. Nevertheless, the discontinuities drastically affect maximum load and displacement before failure.

The affected maximum load and displacement before the failure, without drastically affecting the strain, led us to test out the load and displacement capacity at 1% strain. The Figure 3.78 is drawn to compare the samples at 1% strain. Sample#3 is not shown in the graph because it does not have that much strain capacity.
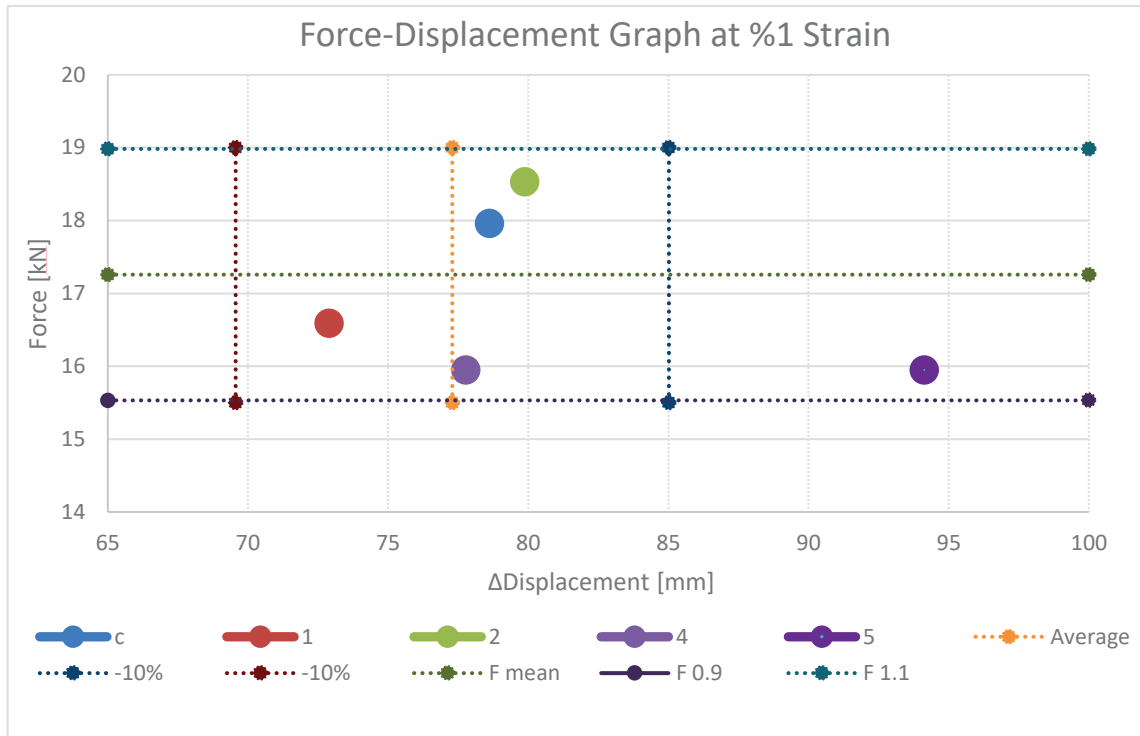
Figure 3.78. Force-Displacement Graph at %1 Strain.

It can be seen that at 1%, Sample #4 and Sample#5 have the lowest load at failure. Intraply discontinuity lessens the fiber volume ratio, thus inducing a lower load. Sample #4 is around Sample#C and average values in displacement comparison, yet Sample #5 is more than the 10% mark and at around 94.1mm, whereas Sample#C is at around 78.6mm displacement. This phenomenon reflects low resin volume ratio matrix. The highest force reaction is measured in Sample#2; the result is similar to Sample#C. Sample#C is 17.96kN yet Sample#2 is 18.53kN at 1% strain. The spectacle is due to a higher rate of Sample#2.

3.5. Fatigue Test

As a way for future works fatigue tests were conducted. The conclusive F Max tests clearly showed that Sample#3 was not suitable as a replacement for Sample#C. Therefore Sample#3 was not included in the fatigue strength tests. The other four samples underwent a comparison, with Sample#C. These samples were meticulously tested based on the designated fatigue limits set for Sample#C and the results were carefully matched with strain measurements to guarantee accurate and dependable data samples tested in the same test rig as F Max tests. The center bolts torqued to 30Nm per serially produced sample.

92

3.5.1. Determining Testing Strain Range

Some trials were conducted to determine an adequate testing limit for the samples. From the F-Max test results, Sample#2 was better than Sample#1. The first comparison tests between Sample#2 and Sample#C were done. Preliminary tests can be seen in Table 3.23, the preliminary test can be seen.

The primary comparison tests are conducted from the same minimum strain level of 5k microstrain. The maximum strain levels have been tested at 12k and 16k microstrain. Sample#2 did not fail the 5k-12k test and was removed without failure and yet had a premature failure at 5k-16k test. As the Maximum Force (Fmax), and Minimum Force (Fmin) test results show, sample #1 samples are not expected to withstand as much as Sample#2. This suggestion is supported by Sample#1 5k-15.5k test result below.

The strain rate determination tests show that the 16k maximum strain limit is too high for Sample#1, and the 12k level was too low for Sample#C and Sample#2. Thus, the limit was determined to be 14k as the average of both maximum strain limits.

3.5.2. Sample#C Fatigue Test Results

The Sample#C fatigue test results are shown in Table 3.24. The results demonstrate a definitive pattern. Their force and displacement values are nearly identical. Most of the samples were successfully removed without any failures despite the prolonged duration of the testing. However, it is worth noting that the samples endured more than 800,000 cycles. The delamination failure modes exhibit similarity across all samples.

3.5.3. Interply Samples' Fatigue Test

Provide examples for comparison Sample#1 and Sample#2 were first tested to set up a foundation for the study. Sample#3 was omitted due to its Fmax results being too low compared to that of Sample#C.

3.5.3.1. Sample#1 Fatigue Test Results

The test results for Sample#1 were inconclusive. During the rate measurement stage, two of the samples failed at the pre-test stage. The issue is also evident in situations involving minimal force levels. As can be seen Table 3.25. Even if the two samples were omitted, the rest were too separated, around 1/10. A typical Sample#1 failure can be seen on Figure 3.79, this sample belongs to failure at 100578 cycles.

Table 3.23. Strain Range Determination Tests.

Type	Microstrain	ΔDisp. (mm) (From F0 to Fmax)	ΔDisp. (mm) (From Fmin to Fmax)	Min/Max Force [kN]	Cycle	Deform. axis	Definition
#1	5k-15.5k	109.5	72.48	7.64-26.03	185	CC0	Failed at 185 Cycle from center along the front arm via middle section delamination.
#2	5k-12k	94.35	54.2	7.52-19.36	303081	-	Removed without failure
#2	5k-16k	125	84.84	8.15-29.08	7828	CCO	Midsection delamination occurred from center along the rear arm at 8K cycles.
#C	5k-16k	125	84.83	7.63-27.90	296000	CCO-CTO	Surface delamination occurred on Compression ve Tension throughout the test. Failed at 296K cycles at center.

Figure 3.79. Sample#1 Typical Failure.

3.5.3.2. Sample#2 Fatigue Test Results

Sample#2 has 2 samples that failed at rate measurement. The rest of the two samples depict deviated results. As can be seen from Table 3.26, one of the acceptable results was around twice that of the other. A typical Sample#2 failure can be seen on Figure 3.80, this sample belongs to failure at 31100 cycles.

Table 3.24. Sample#C Fatigue Test Results.

Type	Microstrain	ΔDisp. (mm) (From F0 to Fmax)	ΔDisp. (mm) (From Fmin to Fmax)	Min/Max Force [kN]	Cycle	Definition
#C	5k-14k	109.5	69.34	7.51-23.36	1029148	RC0-RC200 Radius Delamination. FT0-FT100 and RT0-RT100 Delamination. Removed without failure.
#C	5k-14k	109.5	69.33	7.43-23.18	998381	FC0-FC100 on radius area fiber delamination. Removed without a failure.
#C	5k-14k	109.5	69.33	7.52-23.52	801611	Compression radius delamination at 114K cycle. Fiber separation at 170K cycle on Comp. and Tension Radius Removed without failure.
#C	5k-14k	109.5	69.39	7.67-23.57	852697	Delamination at 62K Cycle on RC0-RC100 axis. Delamination at 320K Cycle 0-FT200 axis. Delamination on the middle section at 852K Cycle is needed for both front and rear arms.

3.5.4. Approaches for Rectifying Inconclusive Test Results

Central bolt torque was reduced to correct the inconclusive test results, and the tests were repeated for interply samples. As can be seen from Table 3.25 and Table 3.28 the results are similar to the 30Nm tests. Sample#1 resulted in 204k cycles without a failure and 21k cycles at failure. Sample#2 showed 47k cycles and 23k cycles at failure. The intraply samples were fatigue tested with 20Nm central bolt torque.

Table 3.25. Sample#1 Fatigue Test Results.

Type	Macrostrain	ΔDisp. (mm) (From F0 to Fmax)	ΔDisp. (mm) (From Fmin to Fmax)	Min/Max Force [kN]	Cycle	Deformation axis	Definition
#1	5k-14k	101.76	64.79	7.72-20.62	1196	FC0-FC50	Total failure at 1K cycles at FC0-FC300 Comp Radius and FC0-FC50.
#1	5k-14k	101.76	64.76	7.55-23.75	100578	FC0-FC50	Delamination at 16K cycle on Comp. Radius. Total delamination at 100K cycles
#1	5k-14k	101.76	64.77	6.91-22.09	84	RC0-RC50	Deformation at rate measurement. Total Failure at fatigue test.
#1	5k-14k	101.76	64.76	6.86-21.92	386	RC0-RC50	Deformation at rate measurement. Total Failure at fatigue test.
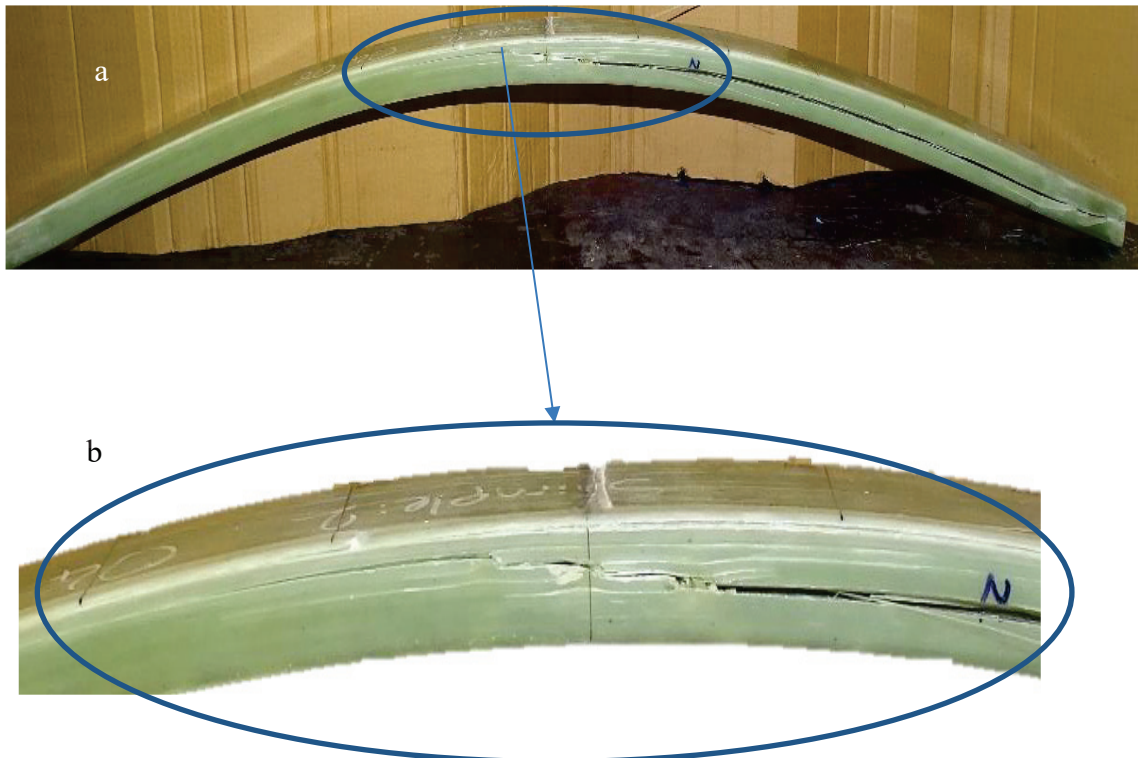
Figure 3.80. Sample#2 Typical Failure. a-Failed sample, b-Fail detail.

Table 3.26. Sample#2 Fatigue Test Results.

Type	Macrostrain	Δ Disp. (mm) (From F0 to Fmax)	ΔDisp. (mm) (From Fmin to Fmax)	Min/Max Force [kN]	Cycle	Deformation axis	Definition
#2	5k-14k	109.5	69.33	7.89-25.01	52393	CC0	Midsection delamination occurred from the center along the rear arm at 52K cycles.
#2	5k-14k	112.85	74.22	7.95-26.25	31100	CCO	Midsection delamination occurred from center along the front arm at 31k cycles.
#2	5k-14k	112.85	74.23	7.70-25.89	415	CCO	Partial deformation at rate measurement. Delamination from center along the front arm at 415 Cycles.
#2	5k-14k	112.85	74.24	7.68-25.77	35	CCO	Partial deformation at rate measurement. Delamination from center along the front arm at 35 Cycles.

Table 3.27. Sample#1 Fatigue Test with 20Nm Centre Bolt Torque.

Sample#	Sample No	Microstrain	Cycle	Definition 20Nm center Torque
1	9	5-14k	204049	removed without failure
1	12	5-14k	21900	delaminated from mid-section

Table 3.28. Sample#2 Fatigue Test with 20Nm Centre Bolt Torque.

Sample#	Sample No	Macrostrain	Cycle	Definition 20Nm center Torque
2	3	5-14k	47334	rear mid-section delamination
2	8	5-14k	23370	delamination mid-section

3.5.5. Fatigue Tests with 20Nm Central Bolt Torques

The remaining sample families, Sample#4 and Sample#5 were tested with 20Nm central bolt torque. The results, as seen in Table 3.29, are similarly inconclusive for these samples, too.

Table 3.29. Fatigue Test Results with 20Nm Centre Bolt Torque.

Centre Bolt Torque 20Nm				
Type	Sample	Microstrain	Cycle	Definition
1	9	5-14k	204049	removed without failure
1	12	5-14k	21900	delaminated from mid-section
2	3	5-14k	47334	read mid-section delamination
2	8	5-14k	23370	delamination mid-section
4	11	5-14k	150000	removed without failure
4	10	5-14k	52213	delamination at center
5	8	5-14k	1318	delamination at center
5	12	5-14k	1741	delamination at center

3.5.6. Fatigue Test Results

Sample#C results show conclusive results. All of the samples are stable and balanced. Sample#1 and Sample#2 results are not stable. Both tests have two failures at rate measurement. The other two test trials resulted in elevated deviation, especially in Sample#1; the acceptable results are more than ten times apart. The F-Max test results indicated that the Force and displacement values, thus rate, do not indicate the health of the samples at all. The samples have similar Force and displacement values, yet the cycles diverge. The deviation can be seen on Table 3.30.

The inconclusive results require more tests. The results do not direct us in any particular direction. The possible reasons for these inconclusive results are due to production and wider void introduced via 5-layer drop-off. The following test samples were produced via the machine layup process to eliminate any production-influenced deviation, leaving us only with the real nature of the discontinuities. It was possible that discontinuities could yield deviation in the fatigue life even with end-to-end comparison.

3.6. Discussion of Test Results

The F Max tests showed that Sample#3 was unsuitable to replace Sample#C. As a result, Sample#3 was not included in the fatigue strength testing. The remaining four samples underwent comparison, with Sample#C. These samples were meticulously tested

based on the specified fatigue limits for Sample#C, and the results were intricately linked to strain measurements to ensure accurate and reliable data.

Table 3.30. Comparison of The Fatigue

Type	Micro strain	Displacement (mm) (From Fmin to Fmax)	Min Force [kN]	Max Force [kN]	Average Cycle	St. Dev.
#1	5k-14k	64.78	7.64	22.19	50887	70274
#2	5k-12k	54.20	7.52	19.36	303081	-
#2	5k-14k	68.63	7.68	23.70	41747	15056
#2	5k-16k	84.84	8.15	29.08	7828	-
#C	5k-16k	5k-16k	125	84.83	7.33	-
#C	5k-14k	69.35	7.53	23.41	920459	-

3.6.1. Effects of Resin Pockets and Exothermic Reactions

The mechanical performance of the samples was significantly affected by resin pockets and the exothermic reactions occurring within them. These areas rich in resin displayed discolorations indicating thermal effects that altered the resin's molecular structure[2]. This thermal degradation notably decreased the materials' strength. CAE models supported these findings by showing resin-rich regions' properties aligning with experimental observations.

Microscopic examination depicted in Figure 3.60, Figure 3.61, Figure 3.62, Figure 3.63 provided insights into discontinuities within Samples. These images illustrated how forces during molding influenced fiber and resin distribution, resulting in strengths and failure patterns. Highlighted areas of exothermic resin deformation associated with resin pocket locations leading to localized breakdowns in the matrix structure.

3.6.2. Mechanical Performance and Composite Integrity

In the sample test areas, high resin content consistently exhibited performance. This trend was also accurately depicted in computer-aided engineering (CAE) models, which forecasted diminished properties in these regions. The findings were mainly inconclusive when compared to the strain levels of samples, underscoring the negative impact of resin pockets on the strength and durability of the overall material.

Upon inspection of fiber and matrix volume fractions, it became evident how crucial these elements are in determining the material's mechanical integrity. Variations within samples influenced fiber ratios, resilience, and gap-filling abilities, ultimately compromising the performance of the composite.

3.6.3. Evaluation of Performance Metrics and Load Capacity

A comprehensive analysis of performance metrics such as Fmax (load) spring rate and displacement capacities across samples is outlined in Table 3.21 and a simplified version can be seen on Table 3.22. The tests indicated that Sample #4 and Sample #5 bore 28% and 31% load, respectively, compared to Sample#C. This decrease can be attributed to the inclusion of regions reinforced with uninterrupted fibers.

Furthermore, these irregularities led to failures under minimal force conditions, resulting in displacement. The maximum displacement for Sample #4 decreased by 29%, while for Sample #5, it decreased by 33%. The results emphasize how resin pockets and their heat-releasing reactions play a role in determining the strength and deformation limits of the specimens. By examining the properties alongside detailed microscopic and volumetric studies, we gain a deep insight into the factors that impact the effectiveness of continuous fiber composites with polymer matrices. This research underscores the significance of addressing material inconsistencies to improve the integrity and dependability of components.

CHAPTER 4

COMPUTER-AIDED ENGINEERING MODELLING

This chapter will compare test values with computer-aided analysis (CAA) results. To increase the quality of the model resin, areas are modeled using a different method.

4.1. Model Correlation with Coupon Tests

The results from the coupon test were used to establish the parameters of the Computer Aided Engineering (CAE) model's simulation. The Altair® program group facilitated the execution of the simulation[86]. To get an initial characterization that replicated the linear tensile behavior of the material, Radioss® was executed.

The CAE model integrates all experimental data obtained using Young's Modulus and Sigma Yield. The Mat25 material model with the PCOMPP property is currently being selected. The 24QEHP Composite Shell formulation obtains maximum computation efficiency while maintaining desired outcomes.

This portion of the assessment focused exclusively on continuous fiber composites. Extra examinations were conducted on samples that originated from intermittent connections. The test data was reduced by implementing the resampling strategy to aid in comparing the findings [107].

4.2. CAE Analysis of Composite Leaf Spring

A single average value was selected as the benchmark sample for comparing the other two categories of items. This action compared the test results with the Computer-Aided Engineering (CAE) simulations. The standard version of Abaqus CAE 6.13 is used to create the Finite Element Method (FEM) models. The leaf spring model can be distinguished from Figure 4.1. The SC8R components, classified as continuum shell elements, are used for simulating composite materials. The SC8R elements are four millimeters in size. Clamping force is incorporated into Finite Element Method (FEM) models by utilizing Abaqus CAE connection force options. An axial wire element can be

used to apply connection force. An axial wire element connecting to the center cylinders in Figure 4.1.
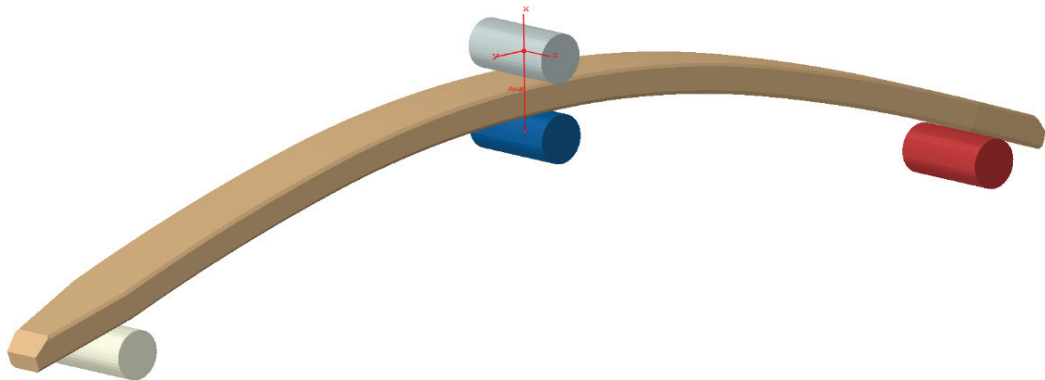
Figure 4.1. The CAE model of the Leaf Spring for Abaqus.

Sample#C is modeled using a single average material value obtained from coupon testing that has been modified with the FVF test results. The material data was a reference for Sample#1, Sample#2, Sample 4, and Sample 5. The Fiber volume fraction ratio in Sample#1 is summarized by segment compared to Sample#C. Measuring the fiber volume fraction revealed different material characteristics. Material data is presented based on the results of fiber volume fraction testing. The methodology for determining material properties in Sample 4's fiber volume fraction measurements define differing material properties. Material data was then assigned based on the corresponding fiber volume fraction test results.

In this study, the Shell Continuum 8-Node Reduced Integration Point (SC8R) element type, known as a kind of shell element, was selected for simulating composite materials. In Abaqus CAE, users have three options for simulating materials: shell, continuum shell, and solid. Traditional shell modeling is not recommended due to resin areas in the leaf spring. The software automatically determines the thickness of the shell elements.

Solid composite modeling can also be used for leaf spring simulation. C3D8R element has some advantages, too. The reason for selecting the C3D8R element type can be its effectiveness in managing deformations and nonlinear responses when subjected to thermal and mechanical loads, ensuring precise outcomes with minimal computational expenses.[34]

Nevertheless, it should be noted that the Continuum 3-dimensional 8-node

Reduced integration element (C3D8R) does not accommodate the Hashin damage criteria.[37,107] This study used the Hashin damage criterion, so the SC8R element was needed.

During the CAE analysis, we made assumptions to ensure that the multilayered structures were accurately modeled. We used nonlinear theory to capture the behavior of the materials under different loading conditions. The resin areas were represented as pure resin to reflect their properties accurately. We assumed that the fiber volume fraction remained consistent outside the discontinuity area to maintain material behavior across the model. The Hashin damage model was employed to estimate failure in the materials, offering a framework for evaluating damage.

Moreover, the thickness of the composite layers was kept constant, for the real models have constant thickness, so the analysis was done without compromising precision. The discontinuity areas' FVF was calculated using the rule of mixtures and matrix burnout test results.[72,73] The material model is selected from pure epoxy resin because of its mechanical plasticity. The subsequent passage delineates the Johnson-Cook plasticity theory is used, as seen in Equation (4.1)[108,109].

$$\sigma_{yield} = A + B\varepsilon_p^n 1 + Cln\frac{\dot{\varepsilon_p}}{\dot{\varepsilon_0}}\left(1 - \hat{\theta}^m\right) \qquad (4.1)$$

Equation (4.1) specifies that parameter A corresponds to the initial yield stress, whereas parameters B, n, C, and m reflect the material constants. In contrast to the reference strain rate, represented by ε_0, the comparable plastic strain is represented by ε_p. A study of Luo et al.[109] demonstrated extensive tests for pure resin, so the results were used as a base for estimating Johnson-Cook plasticity parameters depicted in Table 4.1 [109].

Table 4.1. Pure Epoxy Material Johnson-Cook Parameters.

(Source: Luo 2021)

Elastic Modulus	Poisson's Ratio	A	B	N
2000 MPa	0.35	20	2000	1.12

4.2.1.Sample#1 CAE Modelling

Abaqus CAE can accurately duplicate Sample#1 to resemble the original closely. Abaqus CAE is a robust software package for finite element analysis and computer-aided engineering activities. The software offers a variety of tools and capabilities that allow users to simulate and analyze real-world scenarios accurately and reliably. Using Abaqus CAE provides for capturing the complex characteristics of Sample#1 and generating a replica that nearly mirrors the original. This can benefit various sectors, such as manufacturing, engineering, and product design.

The sections are the same size and position as FVF, mentioned in the previous sections. The FVF ratio compared with Sample#C, along with position, can be seen on Table 4.2and Figure 4.2 respectively. To compare the model with the beam samples, please refer to Figure 3.48 and Figure 3.60.

Table 4.2: Sectional Fiber Volume Fraction Ratio of Sample#1 to Sample#C.

Section #	FVF Ratio	Section #	FVF Ratio
S1-1	0.86	S1-6	0.83
S1-2	0.82	S1-7	0.86
S1-3	0.82	S1-8	0.82
S1-4	0.98	S1-9	0.8

4.2.2. Sample#2 CAE Modelling

Abaqus CAE enables the representation of Sample#2's features, producing a duplicate that closely resembles the original. This feature is particularly advantageous for manufacturing, engineering, and product development industries. The components retain dimensions and locations as indicated by the fiber volume fraction (FVF) discussed in the preceding sections.

The comparison of FVF ratios with Sample#C, as their respective positions, is illustrated in Table 4.3, and Figure 4.3. To compare the model with the beam samples, please refer to Figure 3.50 and Figure 3.61.

Figure 4.2. Divided Sections of Sample #1.

Table 4.3. Sectional Fiber Volume Fraction Ratio of Sample#2 to Sample#C.

Section #	FVF Ratio	Section #	FVF Ratio	Section #	FVF Ratio	Section #	FVF Ratio
S2-1	0.79	S2-5	0.93	S2-9	0.84	S2-13	1
S2-2	0.78	S2-6	0.88	S2-10	0.79	-	-
S2-3	0.79	S2-7	0.87	S2-11	0.8	-	-
S2-4	0.89	S2-8	0.7	S2-12	0.81	-	-

4.2.3. Sample#4 CAE Modelling

By using Abaqus CAE, it is possible to accurately depict the characteristics of Sample#4 and generate a replica that closely resembles the original. This feature demonstrates its worth in various sectors, such as manufacturing, engineering, and product development. The segments maintain the dimensions and positioning indicated by the sections' fiber volume fraction (FVF). The FVF ratios of Sample#C are compared with their respective positions in

Table 4.4 and Figure 4.4. Figure 4.5 demonstrates the rest of the model, which depicts pure epoxy zones. To compare the model with the beam samples, please refer to Figure 3.54 and Figure 3.62.
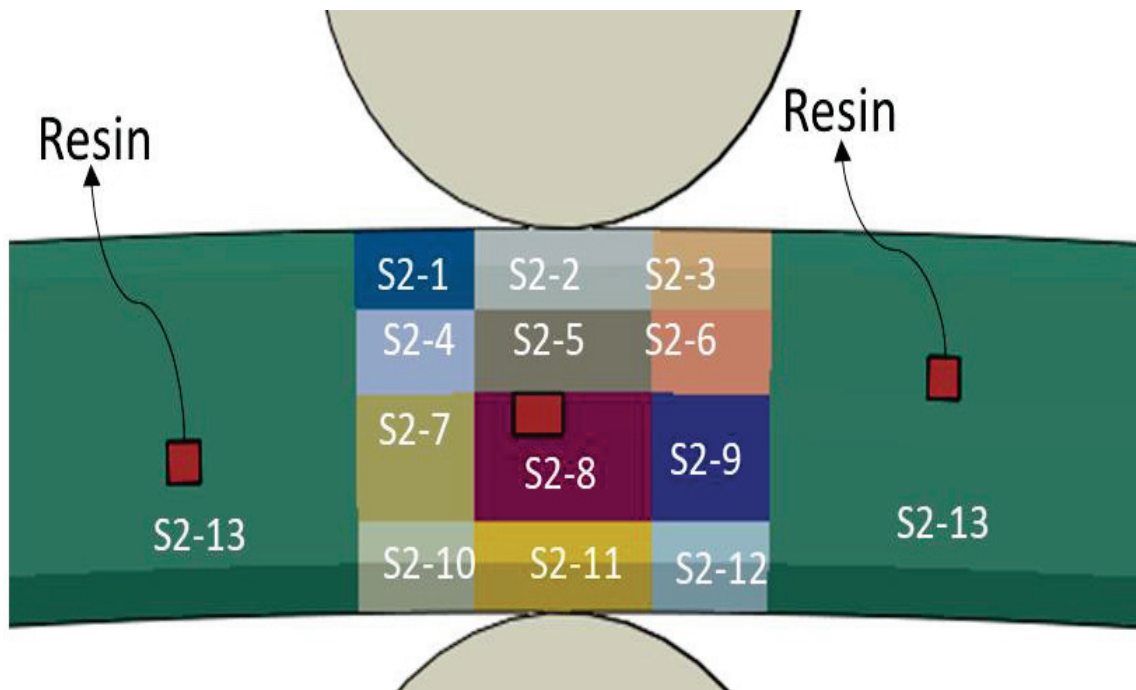
Figure 4.3. Divided Sections of Sample #2.
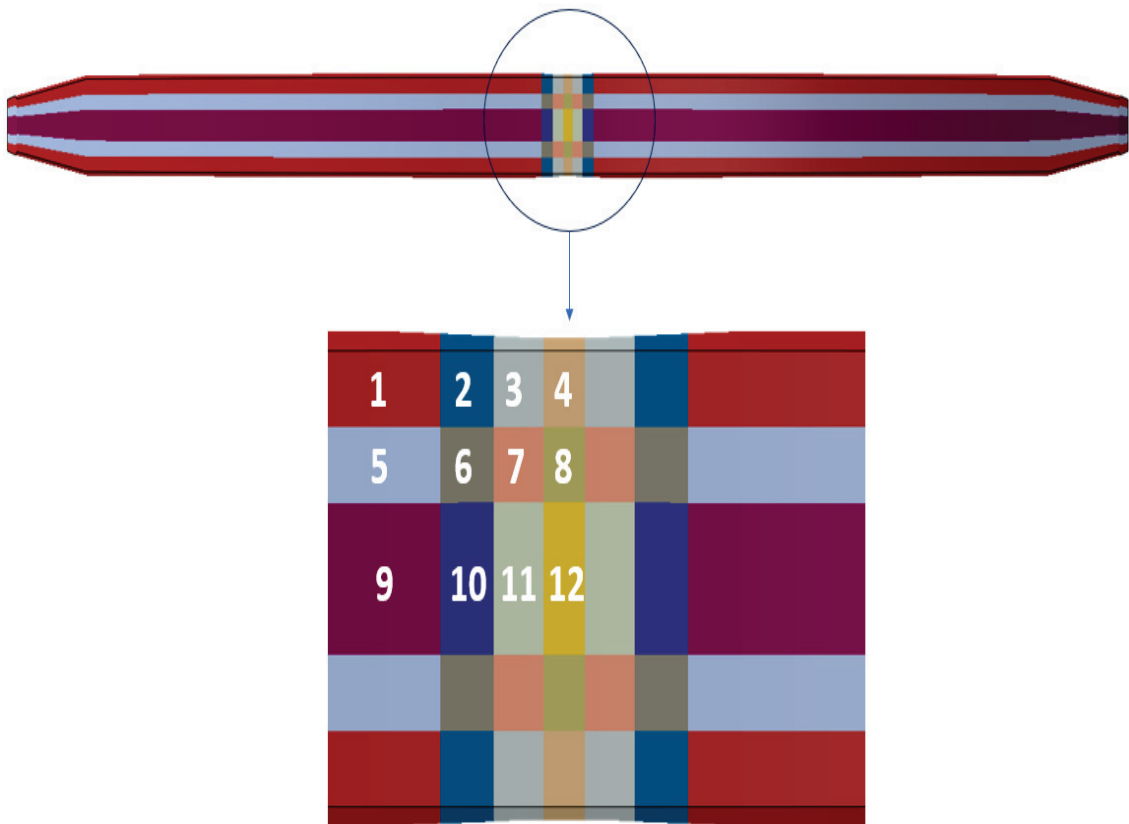
Figure 4.4. Divided Sections of Sample #4.

Table 4.4. Sectional Fiber Volume Fraction Ratio of Sample #4 to Sample #C.

Section #	FVF Ratio	Section #	FVF Ratio
S4-1	0.93	S4-7	0.93
S4-2	1.03	S4-8	0.93
S4-3	1.07	S4-9	0.92
S4-4	1.06	S4-10	0.93
S4-5	0.92	S4-11	0.93
S4-6	0.93	S4-12	0.93
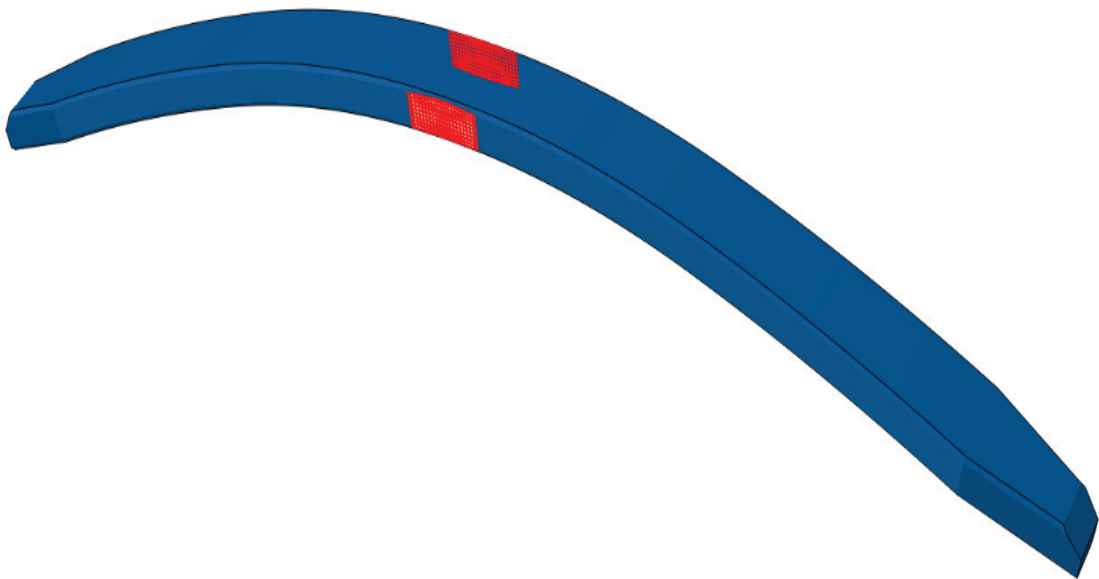
Figure 4.5. The pure epoxy area of Sample #4 is represented by the color red in the model.

4.2.4. Sample#5 CAE Modelling

By using Abaqus CAE, it is possible to accurately depict the characteristics of Sample#5 and generate a replica that closely resembles the original. This feature demonstrates its worth in various sectors, such as manufacturing, engineering, and product development. The segments maintain the dimensions and positioning indicated by the sections' fiber volume fraction (FVF). The FVF ratios of Sample#C are compared with their respective positions in Table 4.5 and . To compare the model with the beam samples, please refer to Figure 3.63 and Figure 3.68.

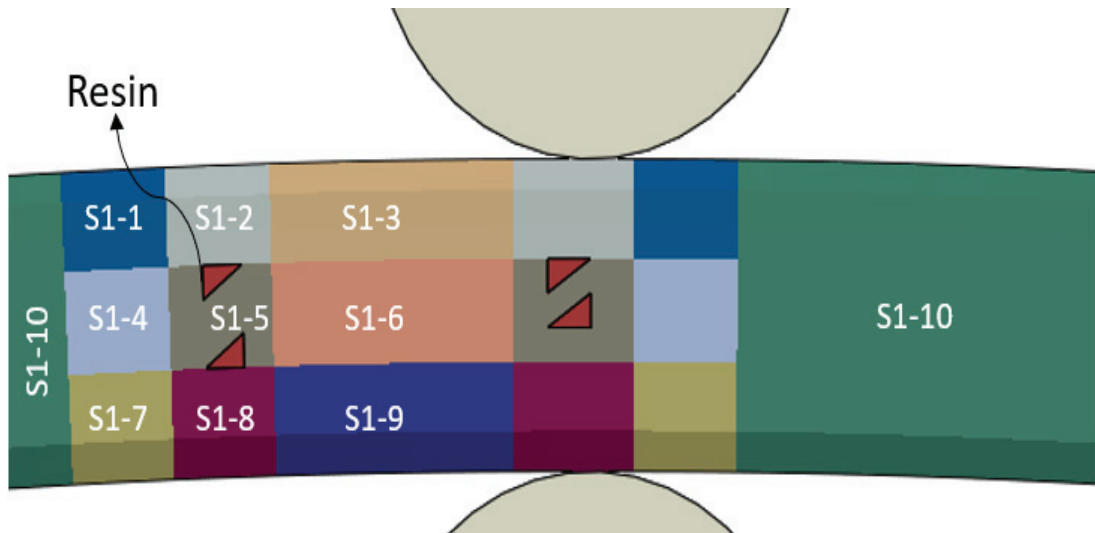Table 4.5 Sectional Fiber Volume Fraction Ratio of Sample #5 to Sample #C.

Section #	FVF Ratio	Section #	FVF Ratio	Section #	FVF Ratio
S5-1	0.99	S5-8	0.87	S5-15	0.9
S5-2	0.99	S5-9	0.89	S5-16	0.92
S5-3	1	S5-10	0.56	S5-17	0.92
S5-4	0.9	S5-11	0.71	S5-18	1
S5-5	0.91	S5-12	0.79	S5-19	1.26
S5-6	0.9	S5-13	0.83	S5-20	1.25
S5-7	0.92	S5-14	0.87	S5-21	1.25
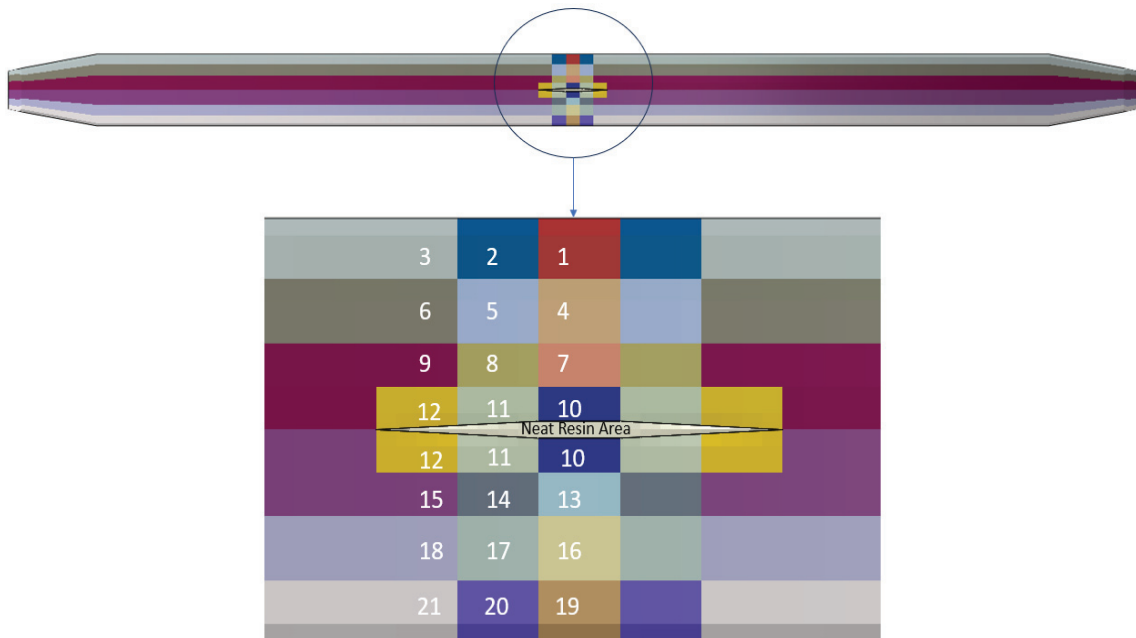
Figure 4.6 Divided Sections of Sample #5.

4.3. CAE Fmax Analysis Results of Composite Beams

The test results were compared with the analysis results to determine the integrity of the CAE model and the method's robustness. Force displacement models are compared based on strain gauge measurement results.

4.3.1.Sample#C CAE Results

The continuous sample CAE analysis result can be seen from Figure 4.7 a). The failure position closely resembles the tests, as shown in Figure 3.72. Due to a lack of discontinuities, the sample tests and the CAE analysis showed the failure at the center of the spring. The test results shown comparable results, as can be seen from Figure 4.7.

Figure 4.7. Sample C CAE Analysis. a) CAE analysis results of continuous composite beams, b) Force-displacement curve comparison between CAE analysis and test results.

4.3.2. Sample#1 CAE Results

CAE analysis findings for Sample#1 are shown in Figure 4.8, Figure 4.9 and Figure 4.10 shows resin failure leading to breaking, with test results shown in Figure 4.8. The matrix failure initiates at the central clamping area where the fiber discontinuity is most pronounced in conjunction with the applied force. Figure 4.8 the comparison between the CAE analysis and Fmax test results is shown in Figure 3.73 indicates that the failure occurred in the compression matrix region. Insufficient fiber reinforcement causes the center of the sample to expand more than other sections in a tripoint bending test, resulting in sample failure. Figure 4.10 shows the failure of the pure epoxy area on the tension side.
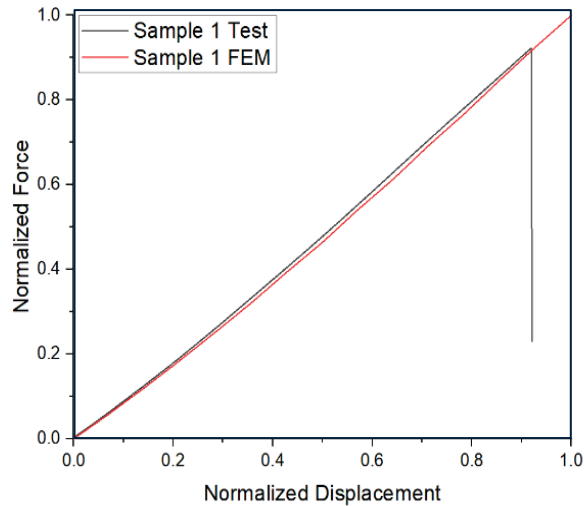
Figure 4.8. Sample#1 CAE Analysis Force Displacement Comparison with Test.
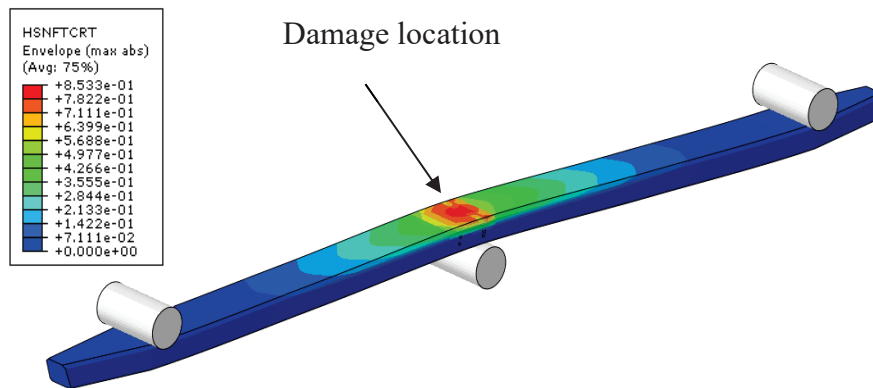
Figure 4.9. Sample#1 CAE Analysis Hashin Fiber Tension Damage.

4.3.3. Sample#2 CAE Results

Sample#2 CAE analysis results are shown in Figure 4.12, Figure 4.13 and Figure 4.11; breakage accrued from tension matrix failure, as the analyzed results are shown in Figure 4.13. The matrix failure is initiated in the center clamping area, where the fiber discontinuity and the applied force are at their maximum. The comparison between the CAE analysis and the Fmax test results is depicted in Figure 3.74 the analysis demonstrated the failure in the compression matrix and compression fiber area.

The outside of the sample at the tripoint bending test stretches more than the mid-section; with enough fiber to help the matrix overcome this tension stress, the sample fails from the compression side. Figure 4.11 The ductile failure criterion shows that the pure epoxy area fails from the tension side.

110
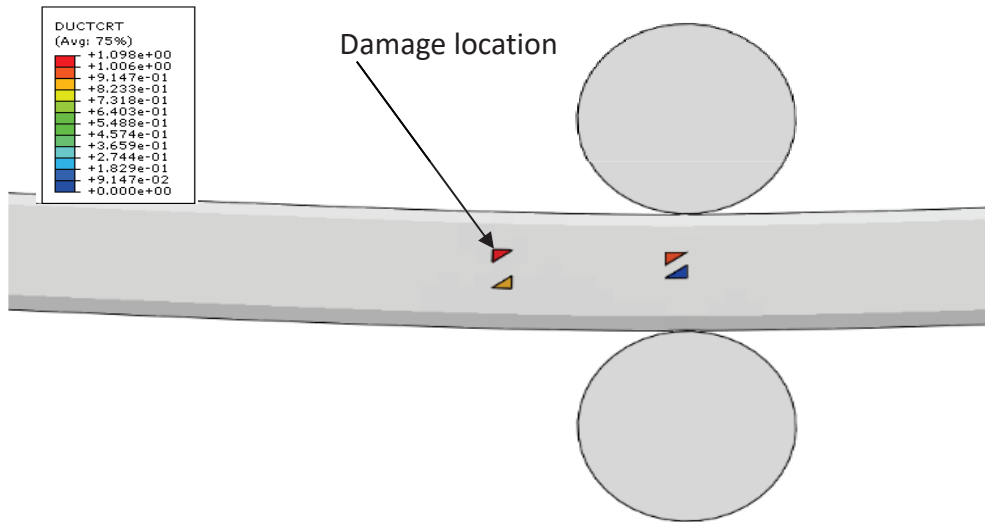
Figure 4.10. Sample #1 Resin Area Damage Criterion.
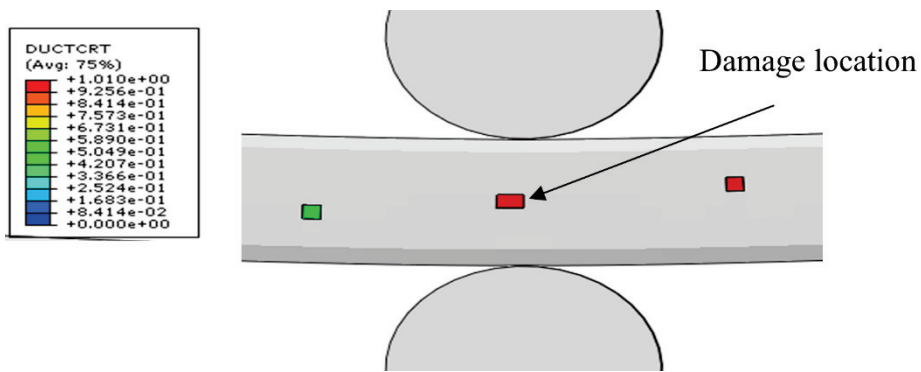
Figure 4.11. Sample #2 Resin Area Ductile Damage Criterion.
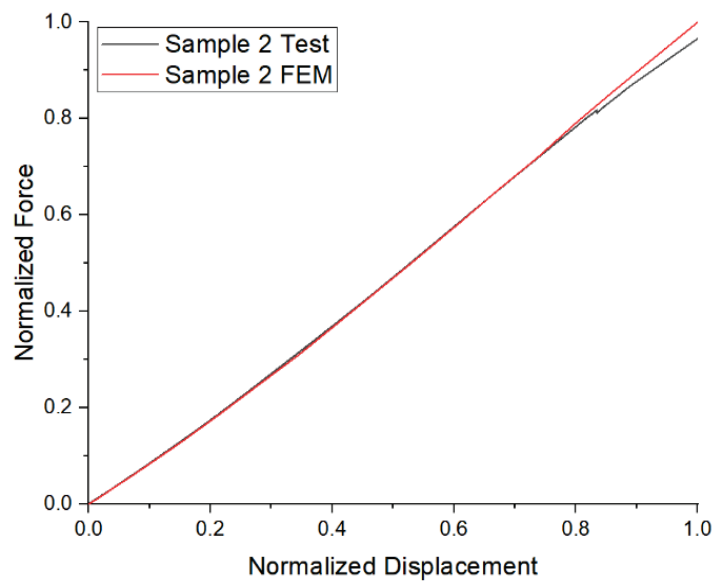
Figure 4.12. Sample#2 CAE analysis Force Displacement Comparison with Test Sample.
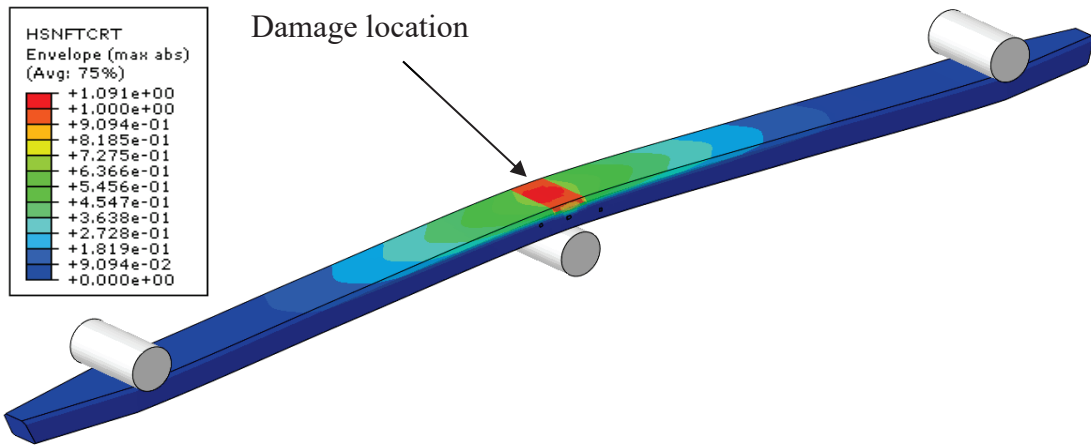
Figure 4.13. Sample#2 CAE analysis Hashin Fiber Tension Damage Location.

4.3.4. Sample#4 CAE Results

Sample #4 CAE analysis results are shown at Figure 4.14. a). Breakage accrued from matrix failure, as the test results are shown in Figure 3.76. The matrix failure is initiated on the center clamping area where the fiber discontinuity and the applied force are at their maximum. The comparison between the CAE analysis and the Fmax test results depicted on Figure 4.14 b). The analysis demonstrated the failure in the tensile matrix and compression fiber area.
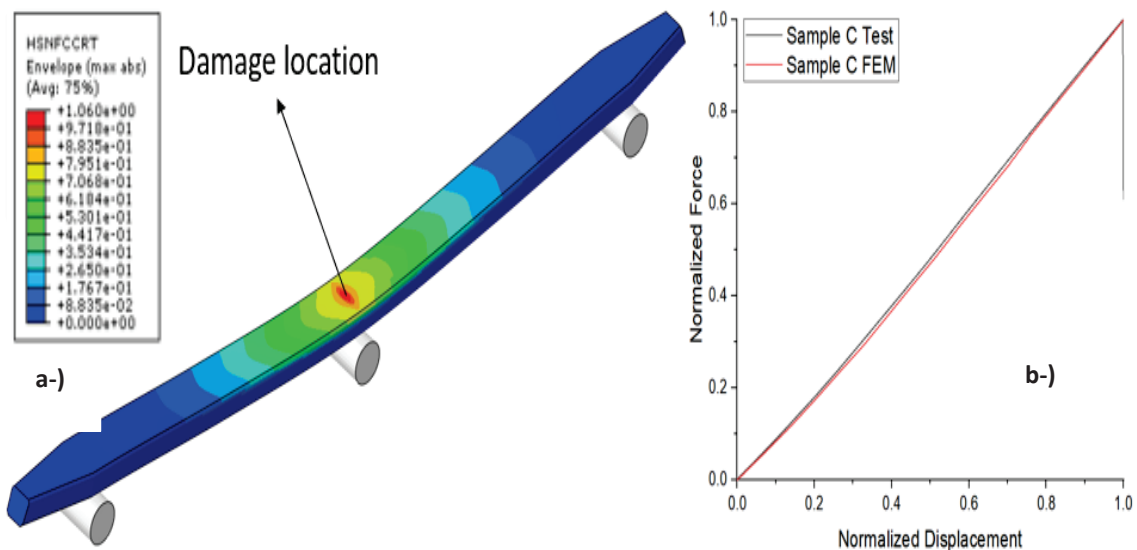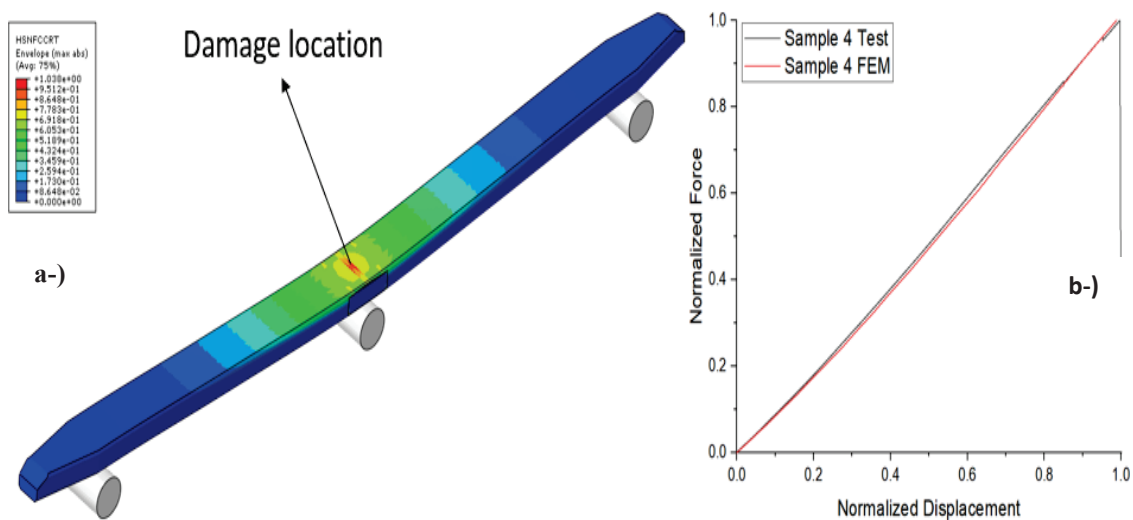

Figure 4.14. Sample #4 CAE analysis. a) CAE analysis results of Sample#4 composite beams, b) Force-Displacement curve comparison between CAE analysis and test results

The outside of the sample at the tripoint bending test stretches more than the mid-section; without enough fiber to help the matrix overcome this tension, the sample fails. Also Figure 4.15 shows the pure epoxy area fails from the tension side.
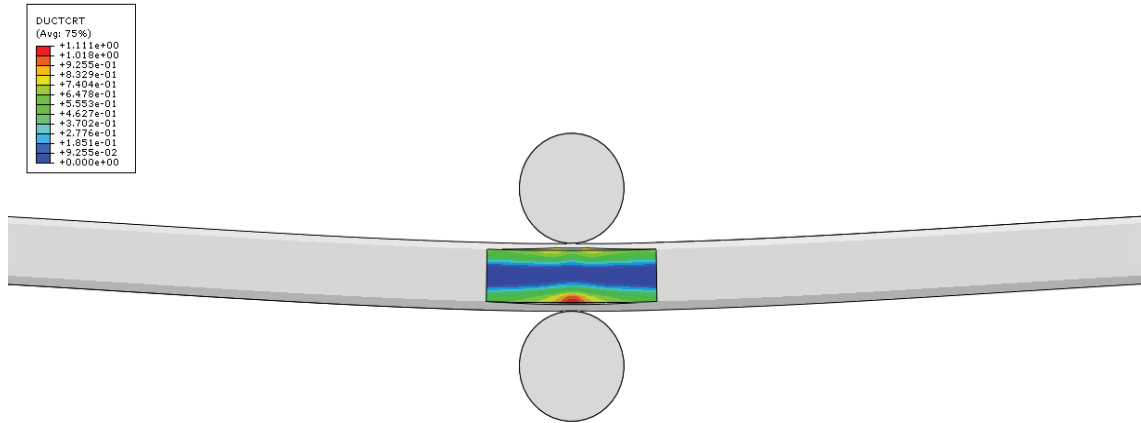
Figure 4.15. Sample #4 Resin Area Damage Criterion.

4.3.5. Sample#5 CAE Results

Sample #5 CAE analysis results are shown at Figure 4.16 a). Breakage accrued from matrix failure, as the test results are shown in Figure 3.77. The matrix failure is initiated on the center clamping area where the fiber discontinuity and the applied force are at their maximum. The comparison between the CAE analysis and the Fmax test results depicted on Figure 4.16 b). The analysis demonstrated the failure in the compression matrix and fiber area. The outside of the sample at the tripoint bending test stretches more than the mid-section; with enough fiber to help the matrix overcome this tension stress, the sample fails from the compression side. Also, Figure 4.17 shows the pure epoxy area fails from the tension side.

4.4. Evaluation of the F-Max Tests

The tested samples indicate that discontinuities drastically affect structures' force and displacement capacities. Nevertheless, the Force/Displacement rates cannot identify these conditions. Even if the yield stress is drastically reduced to one-third, as in Sample #3, the rate only changed around twenty percent. Some samples even demonstrated an increase in the spring rates (Sample #1, #2). So, the rate deviation is insufficient to

conclude the discontinuity's severity. Results demonstrated that interply discontinuities could increase spring rates. This can be used to produce higher spring rates if needed.
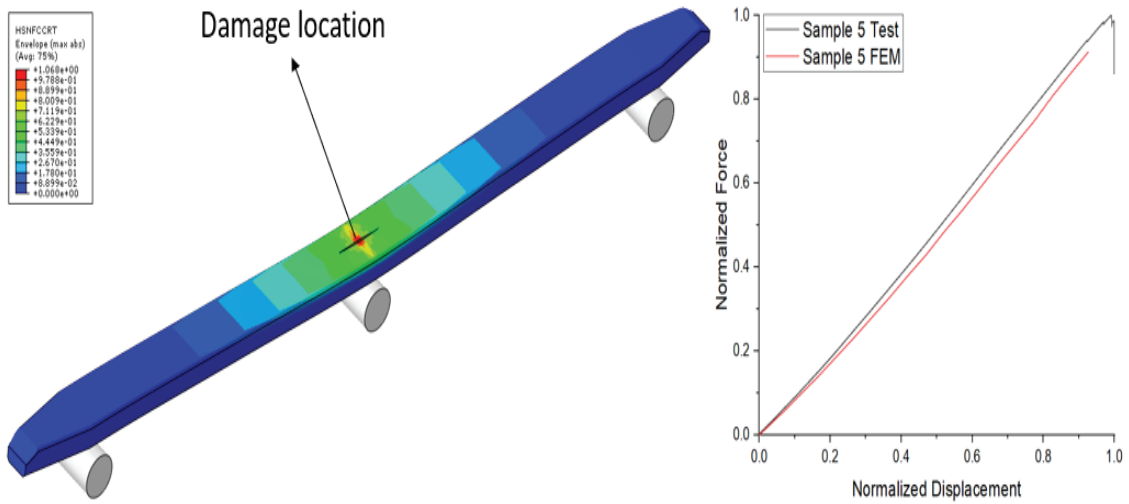
Figure 4.16. Sample #5 CAE analysis. a) CAE analysis results of Sample#5 composite beams, b) Force-Displacement curve comparison between CAE analysis and test results
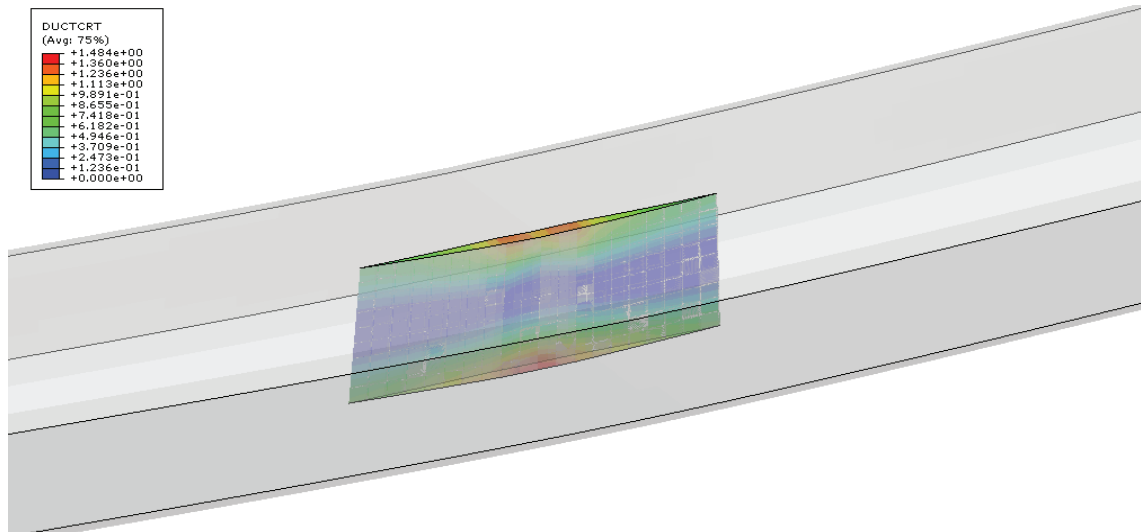
Figure 4.17 Sample #5 Resin Area Damage. Criterion

Samples with low resin rich areas, such as E.G Sample #2, can withstand higher forces in lower than maximum strains even than Sample #C. In the tests, this condition happens at lower strain states than the maximum conditions. Since all of the samples failed before the maximum strain of Sample#C, this condition is compared at 1% strain. Sample #3 has a lower yield point, yet this can be used to produce crush beam-like

114

structures that can support vehicle pulling hooks.

It is widely noted upon examining sources that comparing computer-aided engineering (CAE) analyses with real flexural test results of polymer matrix continuous fiber composites frequently produces highly accurate results. These accurate results are essential for ensuring the reliability of simulations. Typically, an accuracy rate exceeding 85% is deemed satisfactory.

A study conducted by Zhang[110] et al. (2020) demonstrated the effectiveness of finite element method (FEM) simulations in accurately predicting the flexural properties of carbon fiber-reinforced polymer composites. Their research showed correlation rates that occasionally reached 99.5%, depending on the modeling techniques.

A research article published in Polymers[111] examined layer carbon fiber reinforced polymer composites and found a discrepancy between simulated and experimental results of flexural tests. The difference ranged from as low as 0.5% to approximately 14.25%. The discrepancy was influenced by the materials and software used in modeling techniques, such as machine learning, which enhanced accuracy. Hence, while correlation rates may vary, reaching accuracy levels above 85% is generally considered satisfactory, and rates approaching or surpassing 90% are often achievable and highly reliable for conducting CAE analyses on properties in polymer matrix fiber composites.

So, the results of this study's CAE analysis show meaningful results. Sample#1 also demonstrates similar outcomes with a correlation of around 92%. Sample#2 demonstrates significant variability in its results, showing a correlation of approximately 96%. Similarly, Sample#4 demonstrates highly consistent outcomes, with a correlation approaching 99%, and Sample#5, where the correlation is approximately 96%.

CHAPTER 5

CONCLUSIONS

The comprehensive testing conducted on various samples has yielded valuable insights into the mechanical behavior of polymer matrix continuous fiber composites. The results of the F Max tests unequivocally demonstrated that Sample#3 is unsuitable as a replacement for Sample#C, thereby eliminating it as a candidate for fatigue strength testing. The remaining samples were analyzed against Sample#C, aligning the testing with its specified fatigue limit, and correlating it with strain measurements to ensure accuracy.

Gaps in the resin are formed within the continuous samples during the consolidation process due to resin flow inside the mold. The resin pockets, distinguishable by their coloration, are caused by elevated curing temperatures and significantly compromise the mechanical strength of the materials. The CAE models effectively depicted this behavior by uncovering characteristics in regions with a high resin concentration, thus corroborating the experimental findings.

Sample#C demonstrated a strong correlation of above 90% between the predictions made by CAE (Computer-Aided Engineering) and the actual experimental results. Sample#4 showed a correlation of 99%, while Sample#5 correlated approximately 96%. These findings underscore the importance of CAE in predicting the mechanical behavior of the samples and the need to minimize resin gaps to prevent discoloration caused by heat accumulation and the formation of fatigue patterns.

The intermittent samples demonstrated the ability to withstand strain of up to 1% while maintaining their strength compared to the completely continuous samples. However, the influence of resin pockets and their thermal effects on mechanical performance cannot be overstated. A central resin gap in Sample#5 resulted in yellow discoloration, although it did not directly cause delamination, further emphasizing the impact of resin pockets on the strength of the materials.

The study has found that intraply samples generally demonstrate greater strength than interply samples due to the uniformity of the matrix and fibers. Examining fiber and matrix volume fractions highlights their significance in determining mechanical strength. Material discontinuities significantly impact fiber ratios, resilience, and gap-filling

ability, affecting performance.

The study findings underscore the importance of examining the influence of resin yellowing on strength, especially in relation to specific samples such as Sample#5, and the need to consider this factor in the testing process.

Conducting investigations on resin additives to prevent color changes and developing mold designs to enhance the transfer of heat and mass are essential upcoming steps. This study emphasizes the significance of material quality and strength in enhancing the performance of polymer matrix continuous fiber composites, leading to the development of more robust and reliable composite structures for future applications. Possible methods to prevent resin browning this issue are as listed:

- Modify the layup to reduce the occurrence of pre-cure gaps, thereby preventing the accumulation of surplus resin in the affected areas, as observed in Sample#1.

- To avoid the displacement of layers caused by the flow of resin, it is necessary to prevent the growth of gaps between the fibers. The voids will be filled with resin, similar to what is observed in Sample#2.

- Avoid the presence of air gaps within the matrix. This will also trigger failure modes. Avoid introducing discontinuities in the tension/compression, as illustrated by Sample#3.

- Optimize the mold design to enhance heat and mass transfer efficiency to mitigate heat clamping. demonstrated by Sample#4 and Sample#5.

The study results underscore avenues for exploration to enhance the effectiveness and dependability of polymer matrix continuous fiber composites across all samples. It is crucial to optimize layup techniques for Sample#1 and Sample#2 to minimize cure gaps and manage layer shifting effectively to prevent resin pockets from forming. For Sample#3, which was excluded from fatigue strength testing, conducting fatigue tests is essential to understand its long-term performance and identify potential enhancements in processing methods. In cases where resin gaps resulted in mechanical performance challenges for Sample#4 and Sample#5, the development of mold designs to improve heat and mass transfer is vital. Moreover, exploring resin additives that can prevent yellowing and delving into the impact of resin yellowing on strength are tasks.

The ongoing use of imaging to monitor the effects of resin pockets and fiber discontinuities will offer insights into the composite integrity. Addressing these areas will result in dependable polymer matrix continuous fiber composites suitable for a broad spectrum of high-performance applications.

REFERENCES

1.   OlgunCelik | Home. http://olguncelik.com.tr/EN/index.php.

2.   Krauklis, A. E. & Echtermeyer, A. T. Mechanism of yellowing: Carbonyl formation during hygrothermal aging in a common amine epoxy. *Polymers (Basel).* **10**, 1017 (2018).

3.   Campbell, F. C. C. (Flake C. . F. Structural Composite Materials. *Struct. Compos. Mater.* 612 (2010) doi:10.31399/asm.tb.scm.9781627083140.

4.   Composites 2020: AMultitude of Markets | CompositesWorld. https://www.compositesworld.com/articles/composites-2020-a-multitude-of-markets.

5.   Komus, A. & Beley, N. 3.15 Composite Applications for Ground Transportation. *Compr. Compos. Mater. II* 420–438 (2018) doi:10.1016/B978-0-12-803581-8.09950-1.

6.   Fromm, J. Composite Fan Blades and Enclosures for Modern Commercial Turbo Fan Engines. (2009).

7.   Manohar, D. M. D Murali Manohar - Polymer Engineering PEB3213 - Polymer Composites Engineering 1. *Appl. Compos.* 1–22 (2019).

8.   The science and technology of composite materials - Curious. https://www.science.org.au/curious/technology-future/composite-materials.

9.   What Are Some Uses of Composite Materials? | Livestrong.com. https://www.livestrong.com/article/131647-what-are-some-uses-composite-materials/.

10.   Boyle, R. J., Parikh, A. H. & Nagpal, V. K. Design Considerations for Ceramic Matrix Composite High Pressure Turbine Blades. *Proc. ASME Turbo Expo* **6**, (2019).

11.   Composites in commercial aircraft engines, 2014-2023 | CompositesWorld. https://www.compositesworld.com/articles/composites-in-commercial-aircraft-engines-2014-2023.

12.   GE Successfully Tests World's First Rotating Ceramic Matrix Composite Material for Next-Gen Combat Engine | GE Aviation. https://www.geaviation.com/press-release/military-engines/ge-successfully-tests-worlds-first-rotating-ceramic-matrix-composite.

13.   Kittleson, J. J. & De Diego, P. Ceramic matrix composite (CMC) turbine blades and methods of forming CMC turbine blades. (2020).

14.   Meetham, G. W. The future of composites in gas turbine engines. *Mater. Des.* **10**, 231–234 (1989).

15.   Al-Khudairi, O. *et al.* Full-scale fatigue testing of a wind turbine blade in flapwise direction and examining the effect of crack propagation on the blade performance. *Materials (Basel).* **10**, (2017).

16.   Mishnaevsky, L. *et al.* Materials for wind turbine blades: An overview. *Materials (Basel).* **10**, (2017).

17.   Wind turbine blades: Glass vs. carbon fiber | CompositesWorld. https://www.compositesworld.com/articles/wind-turbine-blades-glass-vs-carbon-fiber.

18.   Huang, W., Xu, R., Yang, J., Huang, Q. & Hu, H. Data-driven multiscale simulation of FRP based on material twins. *Compos. Struct.* **256**, 113013 (2021).

19.   Li, H. *et al.* Multiscale design of carbon-based, high-efficiency and wide-frequency microwave-absorption composites. *Ceram. Int.* **47**, 20467–20475 (2021).

20.   Peng, Z., Wang, X. & Wu, Z. Multiscale strength prediction of fiber-reinforced polymer cables based on random strength distribution | Elsevier Enhanced Reader. *Composites Science and Technology* vol. 196 108228 https://reader.elsevier.com/reader/sd/pii/S0266353819335699?token=E10F93C3 06519A657F482D72926C99F8C5A0CFE4B4ECCF6AED8030AD4532FBA2A D0B940AD2CA42E31844F8FA23F38948&originRegion=eu-west1&originCreation=20210831172709 (2020).

21.   Wang, X. *et al.* Prediction of the inter-fiber mechanical properties of composites: Part II Failure criterion based on micromechanics and cross-scale stress calculation. *Compos. Struct.* **271**, 114126 (2021).

22.   Sahota, J. K., Gupta, N. & Dhawan, D. Fiber Bragg grating sensors for monitoring of physical parameters: a comprehensive review. *Opt. Eng.* **59**, 1 (2020).

23.   Bai, X. *et al.* Sensing applications of fiber Bragg gratings in single mode fibers with as-drawn 25 μm diameter cladding. *Opt. Laser Technol.* **144**, 107451 (2021).

24.   Zweben, C. Composite Materials. *Mech. Eng. Handb.* 1–37 (2015) doi:10.1002 /9781118985960.MEH110.

25.   Han, M. G. & Chang, S. H. Draping simulations of carbon/epoxy fabric prepregs using a non-orthogonal constitutive model considering bending behavior. *Compos. Part A Appl. Sci. Manuf.* **148**, 106483 (2021).

26.   Mei, M., He, Y., Yang, X. & Wei, K. Analysis and experiment of deformation and draping characteristics in hemisphere preforming for plain woven fabrics. *Int. J. Solids Struct.* **222**–**223**, 111039 (2021).

27.   Butler, S. *et al.* Effect of embedded sensors on interlaminar damage in composite structures. *J. Intell. Mater. Syst. Struct.* **22**, 1857–1868 (2011).

28.   Series production of composite leaf springs. https://www.henkel.com/press-andmedia/press-releases-and-kits/2013-03-08-press-release-series-production-of-composite-leaf-springs-144034.

29.   Schirmaier, F. J., Weidenmann, K. A., Kärger, L. & Henning, F. Characterisation of the draping behaviour of unidirectional non-crimp fabrics (UD-NCF). *Compos. Part A Appl. Sci. Manuf.* **80**, 28–38 (2016).

30.   How soccer ball is made - material, making, history, used, industry, machine. https://www.madehow.com/Volume-5/Soccer-Ball.html.

31.   Fikry, M. J. M., Vinogradov, V. & Ogihara, S. Experimental observation and modeling of resin pocket cracking in unidirectional laminates with ply discontinuity. *Compos. Sci. Technol.* **218**, 109175 (2022).

32.   Ke, J., Wu, Z. yu, Chen, X. ying & Ying, Z. ping. A review on material selection, design method and performance investigation of composite leaf springs. *Compos. Struct.* **226**, 111277 (2019).

33.   Dewangan, H. C., Thakur, M., Deepak, S. S. K. & Panda, S. K. Nonlinear frequency prediction of cutout borne multi-layered shallow doubly curved shell structures. *Compos. Struct.* **279**, 114756 (1995).

34.   Dewangan, H. C. *et al.* Thermo-mechanical large deformation characteristics of cutout borne multilayered curved structure: Numerical prediction and experimental validation. *Int. J. Non. Linear. Mech.* **150**, 104345 (2023).

35.   Dewangan, H. C., Panda, S. K. & Sharma, N. A review of linear and nonlinear structural responses of laminated flat/curved panels with and without cutout under thermo-mechanical loading. *Compos. Struct.* **303**, 116340 (2023).

36. Dewangan, H. C. *et al.* Geometrical large deformation-dependent numerical dynamic deflection prediction of cutout borne composite structure under thermomechanical loadings and experimental verification. *Acta Mech.* **233**, 5465–5489 (2022).

37. Dewangan, H. C., Sharma, N. & Panda, S. K. Numerical Nonlinear Static Analysis of Cutout-Borne Multilayered Structures and Experimental Validation. *https://doi.org/10.2514/1.J060643* **60**, 985–997 (2021).

38. Hirwani, C. K., Tiwari, S., Mishra, P. K., Dewangan, H. C. & Panda, S. K. Numerical hygrothermal frequency of pre-damage shallow shell panel: A nonlinear FE approach. *Waves in Random and Complex Media* (2022) doi:10.1080/17455030.2022.2091181.

39. Mouritz, A. P., Leong, K. H. & Herszberg, I. A review of the effect of stitching on the in-plane mechanical properties of fibre-reinforced polymer composites. *Compos. Part A Appl. Sci. Manuf.* **28**, 979–991 (1997).

40. Ivanov, D., Ivanov, S., Lomov, S. & Verpoest, I. Strain mapping analysis of textile composites. *Opt. Lasers Eng.* **47**, 360–370 (2009).

41. Potter, K., Khan, B., Wisnom, M., Bell, T. & Stevens, J. Variability, fibre waviness and misalignment in the determination of the properties of composite materials and structures. *Compos. Part A Appl. Sci. Manuf.* **39**, 1343–1354 (2008).

42. Vallons, K. A. M. Fatigue of non-crimp fabric composites. *Fatigue Text. Compos.* 275–293 (2015) doi:10.1016/B978-1-78242-281-5.00012-2.

43. Rajak, D. K., Pagar, D. D., Kumar, R. & Pruncu, C. I. Recent progress of reinforcement materials: a comprehensive overview of composite materials. *J. Mater. Res. Technol.* **8**, 6354–6374 (2019).

44. Rajak, D. K., Wagh, P. H. & Linul, E. Manufacturing technologies of carbon/glass fiber-reinforced polymer composites and their properties: A review. *Polymers (Basel).* **13**, (2021).

45. Ravishankar, B., Nayak, S. K. & Kader, M. A. Hybrid composites for automotive applications – A review. *J. Reinf. Plast. Compos.* **38**, 835–845 (2019).

46. Hull, D. & Clyne, T. W. An Introduction to Composite Materials. *An Introd. to Compos. Mater.* (1996) doi:10.1017/CBO9781139170130.

47. Callister Jr, W. D. & Rethwisch, D. G. *Characteristics, Application, and Processing of Polymers. Materials Science and Engineering - An Introduction* (2018).

48. Miracle, D. B. Metal matrix composites - From science to technological significance. *Compos. Sci. Technol.* **65**, 2526–2540 (2005).

49. Chawla, K. K. Composite materials: Science and engineering, third edition. *Compos. Mater. Sci. Eng. Third Ed.* 1–542 (2012) doi:10.1007/978-0-387-74365-3/COVER.

50. Chawla, N. & Chawla, K. K. *Metal Matrix Composites 2nd Edition*. (2013).

51. Masuelli, M. A. & Masuelli, M. A. Introduction of Fibre-Reinforced Polymers − Polymers and Composites: Concepts, Properties and Processes. *Fiber Reinf. Polym. - Technol. Appl. Concr. Repair* (2013) doi:10.5772/54629.

52. Sanivada, U. K., Mármol, G., Brito, F. P. & Fangueiro, R. Pla composites reinforced with flax and jute fibers—a review of recent trends, processing parameters and mechanical properties. *Polymers (Basel).* **12**, 1–29 (2020).

53. Chaitanya, S., Singh, A. P. & Singh, I. Processing of lignocellulosic fiber-reinforced biodegradable composites. *Nat. Fiber-Reinforced Biodegrad. Bioresorbable Polym. Compos.* 163–181 (2017) doi:10.1016/B978-0-08-100656-6.00009-1.

54. Lubin, G. *Handbook of Composites*. *Handbook of Composites* (Springer US, 1982). doi:10.1007/978-1-4615-7139-1.

55. Handbook of Print Media. *Print Pap. Eur.* **13**, 35 (2001).

56. HOT MELT PREPREG MAKING SYSTEM | Mikrosam. https://archive.mikrosam.com/new/article/en/hot-melt-prepreg-making-system/index.html.

57. Biscaia, H. C., Chastre, C. & Viegas, A. A new discrete method to model unidirectional FRP-to-parent material bonded joints subjected to mechanical loads. *Compos. Struct.* **121**, 280–295 (2015).

58. Prepreg Systems. https://www.calitzler.com/prepreg-systems/.

59. Shafaq *et al.* Influence of deposition rates on the mode I fracture toughness of in-situ consolidated thermoplastic composites. *Compos. Part B Eng.* **251**, 110474 (2023).

60. Campbell, F. Structural Composite Materials. ASM International. *ASM Int.* 612 (2010).

61. Schueler, D., Toso-Pentecôte, N. & Voggenreiter, H. Effects of static preloads on the high velocity impact response of composite plates. *Compos. Struct.* **153**, 549–556 (2016).

62. Zhao, C., Donough, M. J., Prusty, B. G. & Xiao, J. Influences of ply waviness and discontinuity on automated fibre placement manufactured grid stiffeners. *Compos. Struct.* **256**, 113106 (2021).

63. Liu, Y., Wang, H., Ding, H., Wang, H. & Bi, Y. Effect of hygrothermal aging on compression behavior of CFRP material with different layups. *Compos. Part B Eng.* **270**, 111134 (2024).

64. Hallett, S. R. & Wisnom, M. R. Numerical investigation of progressive damage and the effect of layup in notched tensile tests. *J. Compos. Mater.* **40**, 1229–1245 (2006).

65. Karthik, K., Rajamani, D., Manimaran, A. & Udayaprakash, J. Evaluation of tensile properties on Glass/Carbon/Kevlar fiber reinforced hybrid composites. *Mater. Today Proc.* **39**, 1655–1660 (2020).

66. Hall, W. & Javanbakht, Z. Design and Manufacture of Fibre-Reinforced Composites. **158**, (2021).

67. Thor, M., Sause, M. G. R. & Hinterhölzl, R. M. Mechanisms of origin and classification of out-of-plane fiber waviness in composite materials — A review. *J. Compos. Sci.* **4**, (2020).

68. Potter, K. & Ward, C. Draping processes for composites manufacture. *Adv. Compos. Manuf. Process Des.* 93–109 (2015) doi:10.1016/B978-1-78242-307-2.00005-1.

69. Arnold, S. E., Sutcliffe, M. P. F. & Oram, W. L. A. Experimental measurement of wrinkle formation during draping of non-crimp fabric. *Compos. Part A Appl. Sci. Manuf.* **82**, 159–169 (2016).

70. Abdalla, F., Megat, M., Sapuan, M. & Bb, S. Determination of Volume Fraction Values Of Filament Wound Glass and Carbon Fiber Reinforced Composites. *ARPN J Eng Appl Sci* **3**, 7–11 (2008).

71. D2584 Standard Test Method for Ignition Loss of Cured Reinforced Resins. https://www.astm.org/d2584-11.html.

72. Taherzadeh-Fard, A., Cornejo, A., Jiménez, S. & Barbu, L. G. A rule of mixtures approach for delamination damage analysis in composite materials. *Compos. Sci. Technol.* **242**, 110160 (2023).

73. Kou, G., Zhang, W., Chen, J., Chen, J. & Yang, Z. An improved rule of mixture model based on deformation coordination in predicting engineering constants of unidirectional fiber reinforced composites. *Mater. Today Commun.* **34**, 105072 (2023).

74. Gutoff, E. B., Cohen, E. D. & Kheboian, G. I. Coating and drying defects : troubleshooting operating problems. 337 (2006).

75. Das, P. P. & Chaudhary, V. Mechanical Characterization Techniques for Composite Materials. *Compos. Mater.* 155–161 (2020) doi:10.1201/97810030806 33-8.

76. ASTM D3039 / D3039M - 17 Standard Test Method for Tensile Properties of Polymer Matrix Composite Materials. https://www.astm.org/Standards/D3039.

77. ASTM D790 - 17 Standard Test Methods for Flexural Properties of Unreinforced and Reinforced Plastics and Electrical Insulating Materials. https://www.astm.org/Standards/D790.

78. Timoshenko, S.P. and Goodier, J.N. (1970) Theory of elasticity. McGraw-Hill, New York. https://www.scirp.org/(S(i43dyn45teexjx455qlt3d2q))/reference/ReferencesPape rs.aspx?ReferenceID=96774.

79. Dr. Henry Tan. MACE 61058: Plasticity – Lab. https://homepages.abdn.ac.uk/ h.tan/pages/teaching/plasticity/lab.htm.

80. ASTM D638 - 14 Standard Test Method for Tensile Properties of Plastics. https://www.astm.org/Standards/D638.

81. Precision, W. S. ASTM D6641/D6641M: Standard Test Method for Compressive Properties of Polymer Matrix Composite Materials Using a Combined Loading Compression (CLC) Test Fixture. American Society for Testing and Materials (2009). 1–13 (2009) doi:10.1520/D6641.

82. ASTM D2344 - Short-Beam Strength Testing of Polymer Matrix Composite Materials (Interlaminar Shear) - TRL. https://www.trl.com/astm_d2344_short_beam_strength_testing_of_polymer_matrix_composite_materials_interlaminar_shear/.

83. Three-Point Bend Test Fixtures - Instron. https://www.instron.com/en/products/testing-accessories/flexure-fixtures/three-point-bend-test-fixtures?region=Global Site&lang=en.

84. 3MTM Scotch-WeldTM Epoxy Adhesive DP420 | 3M United States. https://www.3m.com/3M/en_US/p/d/b40066431/.

85. Course: Learn Composite Analysis with OptiStruct. https://certification.altair university.com/course/view.php?id=175.

86. Material Characterization of Continuous Fiber Composites. https://www.altair .com/resource/material-characterization-of-continuous-fiber-composites.

87. Altair. Composite Optimization with OptiStruct11.0 on the example of a Formula - Student - Monocoque.

88. Altair acquires Multiscale Design Systems. *Reinf. Plast.* **59**, 162 (2015).

89. Müller, M. Tutorial : Composite Tensile Test and Cantilever Beam using Altair HyperMesh TM and Altair OptiStruct TM 2021. (2021).

90. Altair HyperWorks. Altair Multiscale Designer. (2020).

91.   Sadd, M. H. *Elasticity: Theory, Applications, and Numerics*. *Elasticity: Theory, Applications, and Numerics* (Elsevier Inc., 2009). doi:10.1016/B978-0-12-374446-3.X0001-6.

92.   Elastic Bending Theory - Roy Mech. https://roymech.org/Useful_Tables/Beams/Beam_theory.html.

93.   Sideris, S. A. & Tsakmakis, C. Consistent Euler – Bernoulli beam theories in statics for classical and explicit gradient elasticities. *Compos. Struct.* **282**, 115026 (2022).

94.   Grunenfelder, L. K. & Nutt, S. R. Void formation in composite prepregs – Effect of dissolved moisture. *Compos. Sci. Technol.* **70**, 2304–2309 (2010).

95.   Muric-Nesic, J., Compston, P., Noble, N. & Stachurski, Z. H. Effect of low frequency vibrations on void content in composite materials. *Compos. Part A Appl. Sci. Manuf.* **40**, 548–551 (2009).

96.   Mehdikhani, M., Gorbatikh, L., Verpoest, I. & Lomov, S. V. Voids in fiber-reinforced polymer composites: A review on their formation, characteristics, and effects on mechanical performance. *J. Compos. Mater.* **53**, 1579–1669 (2019).

97.   Fu, Y. & Yao, X. A review on manufacturing defects and their detection of fiber reinforced resin matrix composites. *Compos. Part C Open Access* **8**, 100276 (2022).

98.   Hamidi, Y. K., Aktas, L. & Altan, M. C. Formation of Microscopic Voids in Resin Transfer Molded Composites. *J. Eng. Mater. Technol.* **126**, 420–426 (2004).

99.   Yathisha, N. & Suresha, S. Influence of post curing methodology on strength of polymer matrix composites with a circular hole and square inbuilt patches. *Mater. Today Proc.* **44**, 1296–1299 (2021).

100. Campana, C., Leger, R., Sonnier, R., Ferry, L. & Ienny, P. Effect of post curing temperature on mechanical properties of a flax fiber reinforced epoxy composite. *Compos. Part A Appl. Sci. Manuf.* **107**, 171–179 (2018).

101. Chavan, V. R., DInesh, K. R., Veeresh, K., Algur, V. & Shettar, M. Influence of post curing on GFRP hybrid composite. *MATEC Web Conf.* **144**, 1–7 (2018).

102. Zhang, J., Qin, Q., Xiang, C. & Wang, T. J. Dynamic response of slender multilayer sandwich beams with metal foam cores subjected to low-velocity impact. *Compos. Struct.* **153**, 614–623 (2016).

103. Clay, S. B. & Knoth, P. M. Experimental results of quasi-static testing for calibration and validation of composite progressive damage analysis methods: *http://dx.doi.org/10.1177/0021998316658539* **51**, 1333–1353 (2016).

104. Beyene, A. T., Belingardi, G. & Koricho, E. G. Effect of notch on quasi-static and fatigue flexural performance of Twill E-Glass/Epoxy composite. *Compos. Struct.* **153**, 825–842 (2016).

105. Han, N. *et al.* Experimental and computational analysis of the polymerization overheating in thick glass/Elium® acrylic thermoplastic resin composites. *Compos. Part B Eng.* **202**, 108430 (2020).

106. Controlling Exotherm - Epoxyworks. https://www.epoxyworks.com/index.php/controlling-exotherm/.

107. Hashin damage. https://abaqus-docs.mit.edu/2017/English/SIMACAECAERef Map/simacae-t-prpmechanicaldamagehashin.htm.

108. Chen, G., Ren, C., Yang, X., Jin, X. & Guo, T. Finite element simulation of high-speed machining of titanium alloy (Ti-6Al-4V) based on ductile failure model. *Int. J. Adv. Manuf. Technol.* **56**, 1027–1038 (2011).

109. Luo, G., Wu, C., Xu, K., Liu, L. & Chen, W. Development of dynamic constitutive model of epoxy resin considering temperature and strain rate effects using experimental methods. *Mech. Mater.* **159**, 103887 (2021).

110. Zhang, Z. *et al.* Predicting Flexural Strength of Additively Manufactured Continuous Carbon Fiber-Reinforced Polymer Composites Using Machine Learning. *J. Comput. Inf. Sci. Eng.* **20**, (2020).

111. Bastovansky, R., Smetanka, L., Kohar, R., Mishra, R. K. & Petru, M. Comparison of Mechanical Property Simulations with Results of Limited Flexural Tests of Different Multi-Layer Carbon Fiber-Reinforced Polymer Composites. *Polym. 2024, Vol. 16, Page 1588* **16**, 1588 (2024).

VITA

Ahmet Süha KILIÇOĞLU

Education

Master of Science (MS), Machine Theory and Dynamics

Dokuz Eylül University, 2014 - 2018

Bachelor's Degree, Mechanical Engineering

Dokuz Eylül University, 2006 - 2010

Professional Experience

OlgunCelik A.Ş., Manisa, *February 2021 – Present*

Machine Technologies and Maintenance Leader (MTB Leader)

OlgunCelik A.Ş., Manisa, *January 2016 - January 2021*

Research and Development Specialist Engineer

Tepaş Elektrik, August 2012 - August 2015

Design and Applications Engineer,

HPA Teknoloji, March 2012 - August 2012

Design and Applications Engineer

Organizations

Member, Turkish Chamber of Mechanical Engineers (TMMOM MMO), 2012- Present